2007

The catalytic partial oxidation of n-tetradecane on Rh and Sr substituted pyrochlores

Daniel Haynes
Louisiana State University and Agricultural and Mechanical College, dhayne5@lsu.edu

THE CATALYTIC PARTIAL OXIDATION OF N-TETRADECANE ON RH AND SR SUBSTITUTED PYROCHLORES

A Thesis
Submitted to the Graduate Faculty of the
Louisiana State University and
Engineering College
in partial fulfillment of the
requirements for the degree of
Master of Science in Chemical Engineering

in

The Department of Chemical Engineering

by
Daniel Haynes
B.S., University of Toledo, 2004
May 2007

Acknowledgements

First and foremost I would like to thank my advisor, Dr. Jerry Spivey, for his constant guidance, support and patience throughout this project. The skills and abilities I have learned from him will surely allow me to be successful not only as a chemical engineer, but in life in general. I would also like to thank David Berry from NETL/DOE for the opportunity to work with the separations and fuel processing division. His expertise in fuel processing and general guidance throughout my time at NETL has been beneficial to the completion of this project. A special thanks to Dushyant Shekhawat for his time, patience, and guidance regarding the numerous questions I had about catalysis. Todd Gardner deserves thanks for his assistance and expertise in catalysis. Thanks also to Donald Floyd for his hard work and troubleshooting advice in performing experiments. To Dr. Harrison and Dr. Griffin I am very appreciative of their time and willingness to serve on my committee. Jo Ann Yuill, Bob Stevens, Jason Trembly, Dustin McIntrye, Christopher Johnson, Grant Bromhal and Simone Honeygan deserve appreciation for their encouragement, time and helpful advice throughout the project.

I would like to thank my girlfriend, Linda Pickering, for her constant support throughout the project. To my father, Michael Haynes, I am very grateful for his encouragement and assistance, for without which I could not have successful completed this work. Finally, I would like to give special thanks to my mother Donna Mihalec, brother Jon-Michael and grandmother, Angela Fonzi whose encouragement throughout this undertaking has also been instrumental to its completion.

Table of Contents

Abstract

Catalyst deactivation by high levels of sulfur and aromatics limits the catalytic partial oxidation (CPOX) of diesel fuel into a H_2-rich stream for fuel cells. These species poison traditional supported metal catalysts because they adsorb strongly to electron dense metal clusters and promote the formation of carbon on the surface. Therefore, it is logical to spatially distribute an active metal into the lattice of a chemically and thermally stable material to create an active catalyst surface that is less likely to accumulate carbon or be deactivated by sulfur. In this work, Rh metal only and Rh + Sr are substituted into lanthanum zirconate (LZ) pyrochlore ($La_2Zr_2O_7$) to give $La_2Rh_yZr_{(2-y)}O_{(7-\xi,)}$ (LRZ) and $La_{(2-x)}Sr_xRh_yZr_{(2-y)}O_{(7-\xi)}$ (LSRZ) catalysts. Their resistance to deactivation and carbon formation were examined by the CPOX of a mixture of model compounds chosen to represent diesel fuel. The results were compared to a commercial Rh/γ-Al_2O_3 catalyst.

Characterization results appear to confirm the Rh metal is distributed throughout the pyrochlore structure and is reducible. Activity screening with the CPOX of n-tetradecane (TD) with no other reactants shows that the Rh substituted in LRZ and LSRZ has activity comparable to the supported Rh/γ-Al_2O_3, and each of these catalysts produces H_2 and CO yields close to equilibrium levels. Effects of polynuclear aromatics (5 wt % 1-methylnaphthalene (MN) in TD), sulfur (1000 ppmw dibenzothiophene (DBT) in TD) and 5 wt % MN + 1000 ppmw DBT in TD on catalytic activity were then tested. Rh/γ-Al_2O_3 was deactivated in all three experiments, likely due to significant carbon accumulation on/near the Rh metal. The activity of the pyrochlores in the presence of the contaminants was LSRZ>LRZ>LZ, which was directly related to carbon formation on the surface. Both LZ and LRZ were irreversibly poisoned by MN and DBT while the

activity of the LSRZ is only kinetically inhibited by these contaminants. The resistance to deactivation by LSRZ is thought to be attributable to the oxygen-ion conductivity that results from Sr substitution into the pyrochlore structure. The presence of Rh, in both LRZ or LSRZ, resulted in a greater resistance to deactivation by sulfur and carbon accumulation on active sites than the supported $Rh/\gamma\text{-}Al_2O_3$.

Chapter 1. Introduction/Literature Review

1.1 Fuel Cells

Fuel cells are being explored as energy conversion devices in stationary and mobile applications because of their efficient operation compared to conventional heat engine technology. A fuel cell is basically a battery, which produces electricity through the electrochemical reaction of fuel (usually H_2) and O_2 as long as both are continuously supplied [1]. Extracting the energy electrochemically avoids heat and frictional losses that occur in thermal cycles and allows more chemical energy to do work [1, 2]. In current energy production technology, conversion losses in thermal cycles account for a large portion of the energy produced. For instance, the Energy Information Administration (EIA) has reported that stationary power generation accounted for 39% of the total energy consumption in the United States in 2005 and that 65% of the energy value of the fuel used to produce this energy was lost due to heat transfer and other conversion losses [3, 4]. In addition, although not quantified, the transportation sector, which consumes 27% of total energy in the U.S. [3, 4], is subject to similar losses because the combustion engines are limited by the Carnot efficiency as well. Although, fuel cells do undergo some efficiency losses due to slow reaction rate or resistance to electron flow [2], these losses are less than for conventional systems as shown by **Figure 1.1**.

In addition to higher efficiency, fuel cells are more environmentally benign energy production sources. The electrochemical oxidation of the fuel is a much cleaner conversion method because energy is produced at a lower temperature than combustion.

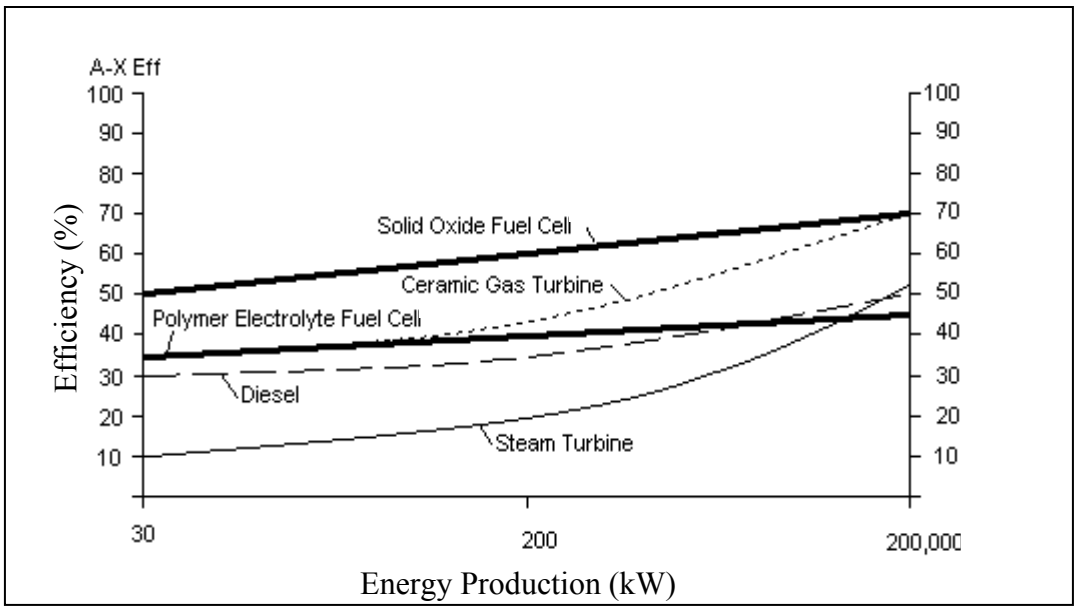

Figure 1.1 Efficiency of fuel cells versus current energy production methods for large-scale stationary power applications. Adapted from The Future of Fuel Cells website [5].

As a result, much of the thermal NO_x and particulate matter emissions that result from burning the fuel are reduced [6, 7]. It is because of the reduction of these emissions that the fuel cell shows a lower global warming potential (**Figure 1.2)**, compared to competing energy production technologies.

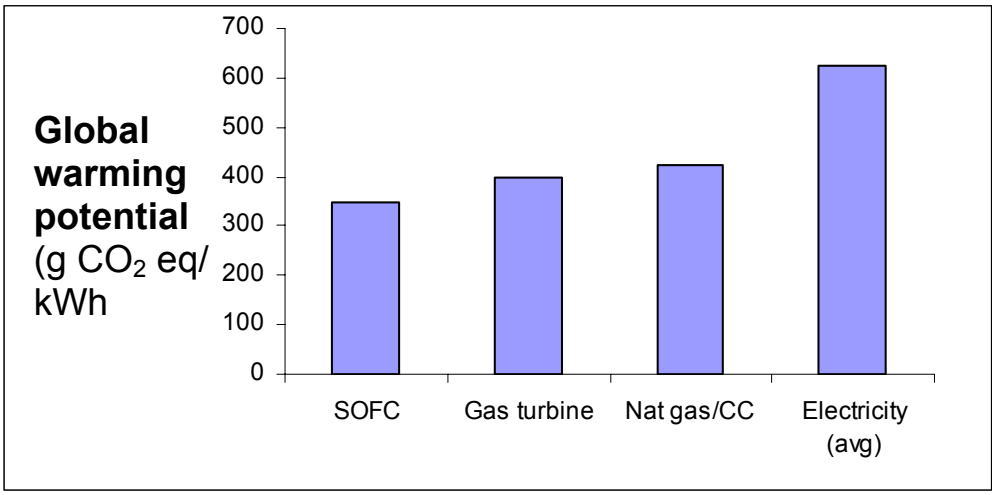

Figure 1.2 Greenhouse gas emissions of SOFC compared to conventional energy sources. Figure adapted from [8].

There are several types of fuel cells that have been developed for power generation: alkaline fuel cell (AFC), proton exchange membrane fuel cell (PEMFC), phosphoric acid fuel cell (PAFC), molten carbonate fuel cell (MCFC), and solid oxide fuel cell (SOFC). Two of these systems, PEMFC and SOFC, have shown the potential to be effective in widespread power applications while having the ability to meet cost targets for commercialization.

PEM fuel cells are defined by their thin polymer based electrolyte that conducts hydrogen protons from the anode to the cathode [1, 2]. Their low operating temperature and compact size have made them suitable for transportation and portable power applications [1, 2]. Specifically, they are being heavily investigated as a replacement for the combustion engine in automobiles [1, 2, 9, 10]. However, their implementation is complicated because a pure H_2 fuel stream is needed. The platinum anode catalyst is highly susceptible to poisoning by CO and sulfur that can be present in certain fuel streams derived from hydrocarbons. To solve this problem, a preferential oxidation reactor is typically used in hydrocarbon fuel processors to convert CO to CO_2 to reduce CO to safe levels, <50 ppm [11].

SOFC's are solid-state energy conversion devices that conduct O_2 anions over a yttria stabilized zirconium (YSZ) ceramic electrolyte to produce electricity [1, 2]. They are a high temperature cell that operates between 600-1000°C. This high operating temperature makes them more tolerant to contamination than PEM cells. They have shown resistance to low levels of sulfur [12], and CO can actually be used as fuel because no noble metal catalysts are needed [1, 2]. CO is converted to CO_2 and electricity. These capabilities makes operation more fuel-flexible gives them a much broader range of

applications. Also, since the fuel requirements are more relaxed, simplified hydrocarbon fuel processing systems can be used. Certain complications regarding electrode durability do arise over long periods of time due to the high operating temperatures [1]. However, these issues are currently being addressed [12, 13], and when resolved, SOFC's are likely to be one of the first commercially available cells. Applications for SOFC's include auxiliary power units (APU's) to supply supplemental power to heavy-duty diesel vehicles [1, 2, 4, 14, 15] as well as large-scale (> 2kW) combined heat and power systems for stationary power [1, 2].

1.2 Logistic Fuels as Fuel for Fuel Cells

Parallel to the development of these fuel cell systems is the development of a sufficient hydrogen fuel supply to generate electricity. For commercial use, hydrogen fuel must be readily available and must also have proper storage capabilities to ensure an adequate supply. However, at this point, a pure hydrogen distribution network and storage technologies are not advanced enough to meet the demands of commercialization [9, 11, 16]. An alternative to supplying pure hydrogen is to reform hydrocarbon fuels into a hydrogen-rich gas for fuel [17, 18]. The catalytic reforming of logistic fuels such as gasoline, diesel, and JP-8 is an attractive solution that can provide hydrogen fuel until a hydrogen infrastructure becomes more developed. Diesel and gasoline are appealing as hydrogen energy sources because of their high hydrogen energy density- which is shown in **Figure 1.3** to be higher than other potential hydrocarbon fuels. They also have an existing, wide-spread distribution network which makes them convenient energy sources.

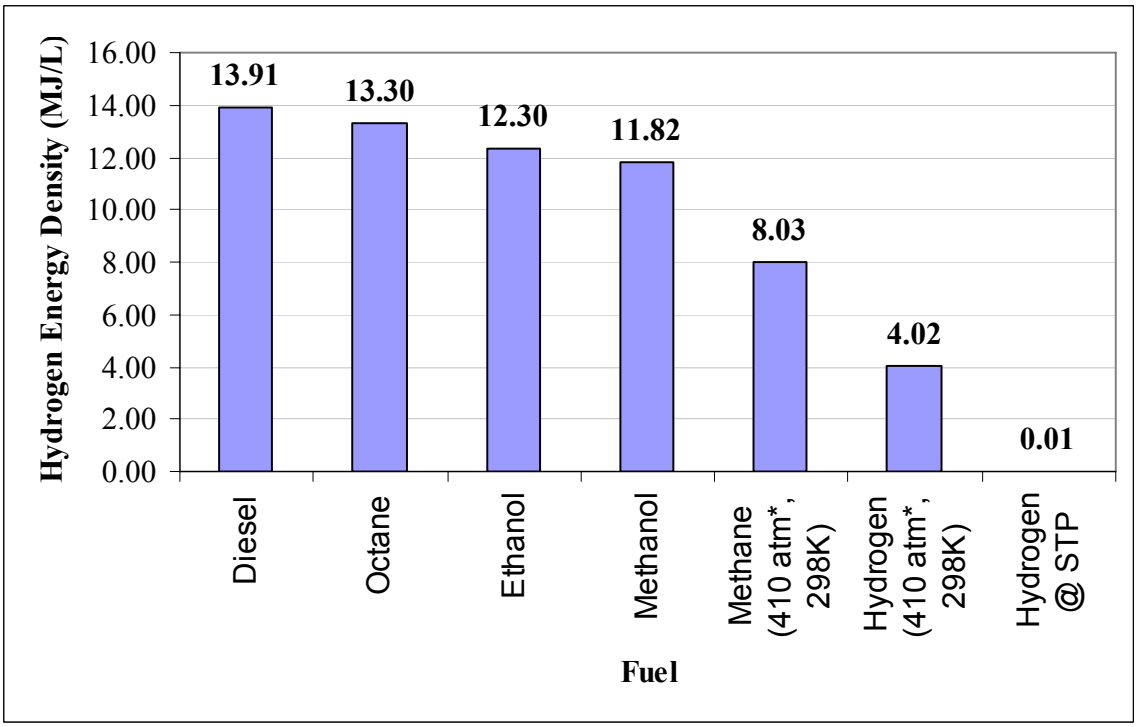

Figure 1.3 Comparison of hydrogen energy densities for different hydrocarbon fuels[a].

[a]- Calculations only consider the hydrogen energy that can be extracted from the compounds. They do not take into consideration added hydrogen formation from water gas shift, or energy from CO oxidation.

*- Pressure value of 410 atm used for hydrogen and methane was adapted from a discussion in reference [19] involving current storage capabilities.

1.3 Reforming Reactions

Three primary reforming reactions can be used to convert the liquid fuel into synthesis gas (H_2 + CO) for fuel cells: steam reforming (SR), autothermal reforming (ATR), and partial oxidation (POX) [17]. Each reaction has specific characteristics which make it efficient for certain applications, but unattractive for others. However, in any fuel processing system, regardless of the reaction scheme chosen, the operating conditions are designed to maximize hydrogen yields and limit the formation of carbon. Carbon formation is a known problem in reforming hydrocarbons because it can accumulate on reactor walls or on the surface of the reforming catalyst and foul the reactor.

SR $\quad C_nH_m + nH_2O \rightarrow (n+m)H_2 + nCO \quad \Delta H > 0 \quad (1)$

ATR $\quad C_nH_m + x(O_2 + 3.76N_2) + (2n - 2x)H_2O \quad \Delta H \sim 0 \quad (2)$

$$\rightarrow (2n - 2x + \frac{m}{2})H_2 + nCO_2 + 3.75xN_2$$

where $\quad x = n + \frac{1}{2}\left(\frac{\Delta H_f Diesel - n\Delta H_f CO_2}{\Delta H_f H_2O}\right)$

POX $\quad C_nH_m + \frac{n}{2}(O_2 + 3.76N_2) \rightarrow \frac{m}{2}H_2 + nCO + 3.76\frac{n}{2}N_2 \quad \Delta H < 0 \quad (3)$

To prevent this problem, the reformers are typically operated at elevated temperatures (>600°C) and in excess of an oxidant (either steam, air or both) to decrease the thermodynamic driving force for carbon formation. Practical reaction conditions and applications for each reaction are discussed below.

1.3.1 Steam Reforming (SR)

SR uses steam to convert the hydrocarbon fuel into a H_2 rich synthesis gas. Of the three reforming reactions, SR has the highest H_2 yield because of the hydrogen contributed from the steam. The reaction can be run at high steam to carbon ratios (S/C) to further increase H_2 yields by converting the CO to CO_2 through the water gas shift reaction shown below.

$$CO + H_2O \rightarrow H_2 + CO_2 \quad (4)$$

High S/C ratios also allow for the oxidation of more carbon and thus reduce carbon formation. However, the steam reforming reaction is highly endothermic, and running at high S/C ratios is not practical. A thermodynamic analysis by Shekhawat et al. shows that it is favorable to run at S/C between 2-3 [17]. **Figure 1.4** shows the amount of

carbon formation that is thermodynamically favorable for the reforming of n-tetradecane ($C_{14}H_{30}$) using SR, ATR and POX over a wide temperature range. SR has the least amount of carbon formed because the high S/C ratio provides more oxygen to react with carbon than is possible in the other two reactions. The temperatures for this reaction are usually in the range of 600-1000°C, which can be seen from Figure 1.4 are in the carbon free operating range.

While SR may have the lowest amount of carbon formation, the reaction rate is limited by heat transfer [9, 11, 17, 20, 21]. For this reason, reformers tend to be heavy and bulky and take up a large amount of space to obtain maximum heat transfer, and are generally limited to stationary applications rather than transportation. Also, the logistics of carrying water onboard are not favorable because extra storage space is needed, and the water supply must be insulated to keep from freezing.

1.3.2 Autothermal Reforming (ATR)

In ATR, fuel, air and water are fed together so that the heat of reaction from POX thermally balances the energy requirements for the endothermic SR reaction. The expression shown below is used to calculate the correct oxygen stoichiometry in equation 2 shown above, to obtain thermoneutrality [17].

$$x = n + \frac{1}{2}\left(\frac{\Delta H_f Diesel - n\Delta H_f CO_2}{\Delta H_f H_2O}\right) \qquad (5)$$

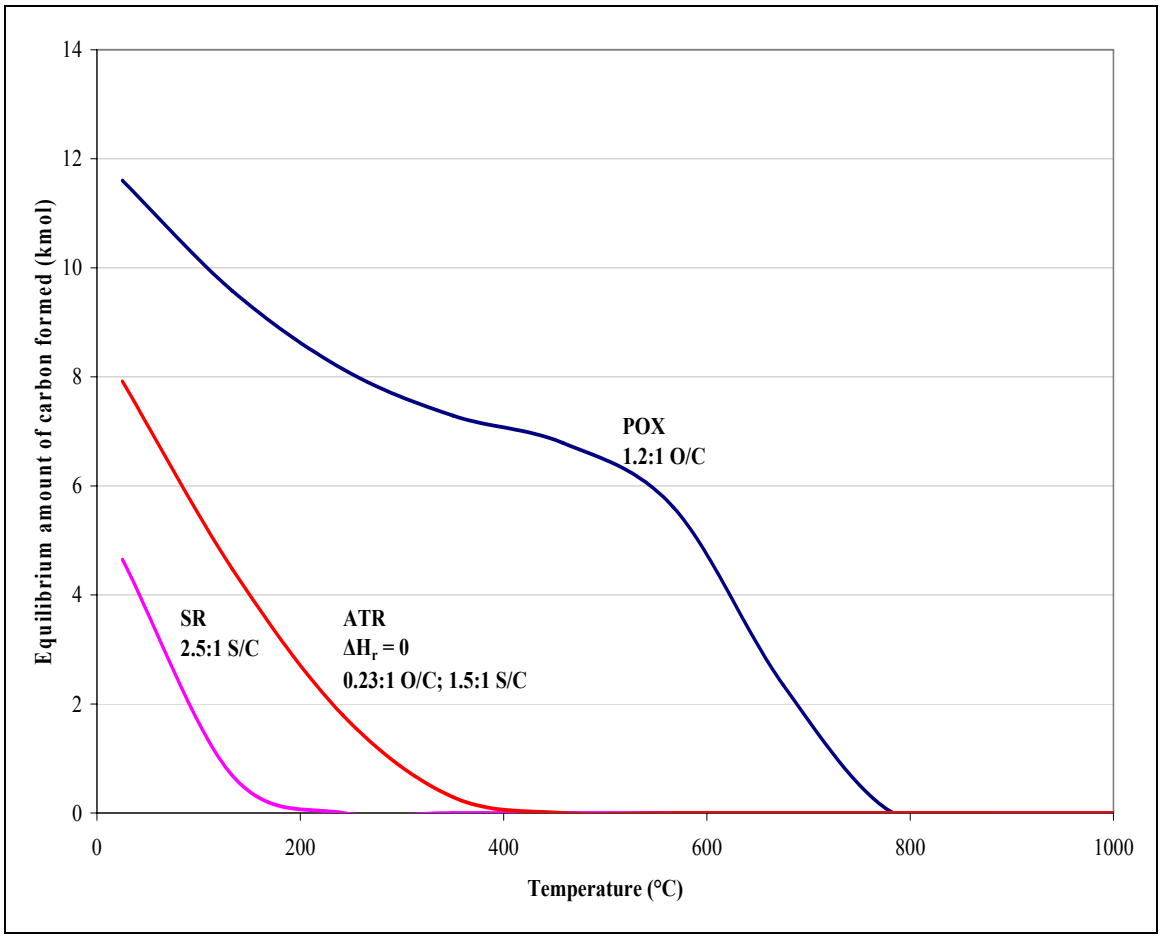

Figure 1.4 The thermodynamic tendency of carbon formation for steam reforming (SR), autothermal reforming (ATR) and partial oxidation (POX) reforming reactions at practical operating conditions. Operating conditions adapted from Shekhawat et al. [17].

Autothermal operation is only one possible operating condition for a feed containing fuel, O_2, and steam. Increasing or decreasing x from thermoneutrality changes the energy requirements for the reaction. As x→0 (SR), the reaction becomes richer in steam and requires more energy to be added. On the other hand, as x→n/2, the reaction approaches POX and becomes more exothermic. Changing x values also affects carbon formation. Figure 1.4 shows that ATR (thermoneutrality) corresponds to an intermediate amount of carbon formed between SR and POX. However a decrease in x will give lower carbon

formation as the reaction approaches SR and an increase in x will result in an increase in carbon as the reaction approaches POX conditions.

An ATR reactor can be thought of as two plug flow reactors in series [17]. The O_2 is consumed first by the exothermic POX reaction, which then provides the energy for the SR to occur. The POX reaction has much faster kinetics than SR, so the system is much more responsive to transients. However, the ATR is not without disadvantages. The reformer requires specific operation and configuration to avoid hot spots that result from the different reaction rates between POX and SR which can deactivate the catalyst [21-23]. In addition, as the reaction consists of POX and SR, an ATR catalyst must be active for both reactions [9, 11, 17]. Noble metals like Rh, Ru, Pd are typically used in ATR reactions [17]. However, because all or most of the energy for the reaction is provided internally by the POX, there are no extreme energy requirements (either addition or removal). This makes ATR the most thermally efficient reaction [9], and as a result it is used more widely in practical applications, like transportation, than SR because ATR reactors are more energy efficient and smaller [9, 11, 22].

1.3.3 Partial Oxidation (POX)

POX reacts fuel and a sub-stoichiometric amount of O_2 to produce H_2 and CO. Although the POX reaction can be carried out thermally, typically the reaction is carried out as catalytic POX, or CPOX. Compared to the other two reactions, CPOX has lower H_2 yields because it can only produce the amount of H_2 contained in the hydrocarbon fuel. However, the process has fast light-off capabilities as well as fast kinetics, which gives it a greater dynamic response to interruptions in the feed (transients) as well as fast throughput [24]. It also has the advantage of being more tolerant to contaminants, like

sulfur, because the presence of O_2 at high reaction temperatures can produce SO_2 [25]. Unfortunately, the process has a greater tendency to form carbon than the other reactions at lower temperatures, as seen in Figure 1.4. Increasing the O/C ratio does not benefit CPOX as it does SR and ATR. Carbon formation does decrease as O/C increases >1, but as the O/C $\rightarrow$ 2 H_2O and CO_2 become thermodynamically favorable products. To compensate for this limitation, CPOX is run at elevated temperatures. An example of operating conditions for CPOX are O/C of 1.2 and between 800-900°C, which is shown in Figure 1.4 to be in the carbon free region.

A CPOX system is not the most efficient option in an energy conversion sense because the high reaction temperatures do not permit much thermal integration. However, the advantages of CPOX allow the reformer to be light-weight and compact in design. In addition, unlike SR or ATR, no water storage or delivery system is required, which makes the system less complex and reduces its cost [24, 26]. These capabilities make CPOX a practical solution for fuel processing systems in mobile/transportation or remote applications where water is scarce. For instance, the DOE has deemed CPOX to be an efficient reforming option to supply fuel to SOFC for a 5 kW net system which may be used as an auxiliary power unit for diesel trucks [27]. Also, CPOX has been investigated for non-power producing applications. A CPOX system may a viable option as a pre-treatment method in combustion engines to provide a solution to NO_x abatement [28-30]. Research has shown that a hydrocarbon/H_2/CO mixture can decrease the operating temperature of spark engines, while maintaining high efficiency, and decrease NO_x emissions [31, 32]. Also, the CPOX system can be modified to produce a

hydrocarbon/O_2/H_2+CO gas mixture that can be used in exhaust systems (either diesel or gasoline) reduce NO_x emissions as well [33, 34].

1.4 Catalytic Partial Oxidation (CPOX) of Logistic Fuels

1.4.1 Fuel Characteristics

Logistic fuels (i.e. diesel and jet fuels), also known as middle distillates, are a complex blend of large molecular weight paraffins (C_{10}-C_{20}), cycloparaffins, naphthenes, aromatics, and organosulfur species. The proportion of these constituents is highly dependent on the feedstock and fuel preparation scheme, and therefore the composition can vary greatly from one refinery to another. A compositional analysis has determined diesel can contain between 20-45 wt% aromatics [35], with the balance mainly n-paraffins and naphthenes. The distribution of the components in these fuels is shown below in **Table 1.1**.

Table 1.1 General distribution of components found middle distillate feedstocks [35].

Component	Weight Percent (%)
Saturated Hydrocarbons (n-paraffins and naphthenes)	55-80
Monoaromatics	15-25
Diaromatics	5-15
Polyaromatics	0-5

Sulfur content is currently regulated to be between 0.01-0.05 wt% [35] (100-500 ppmw), however it can be as high as 0.3 wt% (3000 ppmw) for military diesel [10, 17].

1.4.2 Issues with the CPOX of Logistic Fuels

In the CPOX process, the fuel is first vaporized to facilitate mixing requirements to obtain a uniform gas mixture with adequate contact of O_2 and hydrocarbon before they reach the catalyst [36]. However, the wide variety of constituents in these fuels gives them a broad boiling range between 160 to 380°C [35]. In order to fully vaporize these fuels, the pre-heat/vaporizer temperature must be operated above the boiling point of the least volatile components (>380°C). In doing so, this can cause the more volatile components to undergo thermal decomposition (pyrolysis) [35, 37, 38] into unsaturated hydrocarbons and aromatics, which are known carbon precursors [39]. These products coupled with the aromatics and sulfur compounds already present, pose a challenge for fuel processing systems because they deactivate CPOX catalysts [10, 17, 40-42].

Also, POX of diesel is a complicated process because the different blends lead to fuel mixtures with different reactivities. This presents a challenge to determine the exact O/C stoichiometry needed for POX. It then becomes further complicated because the fuels compete for oxygen at the active sites of the catalyst and the most reactive compound will consume the O_2 rapidly and leave the less reactive components to undergo pyrolysis and potentially form carbon [43, 44].

1.4.3 Surrogate Fuels

The problems associated with the composition and reactivity between different feedstocks can be reduced using surrogate fuel mixtures. A surrogate fuel is a fuel with a well defined composition and with a similar behavior to that of the parent fuel. They can be composed of between 1-15 hydrocarbons chosen to represent various classes of

compounds found in diesel. The use of surrogate fuels decreases the complexity of reforming diesel and provides an understanding of reaction pathways. The fuel compositions are well-defined and reproducible, which allows for systematic testing and a precise O/C stoichiometry to be calculated for each experiment. Also, selected components can be isolated in mixtures (like sulfur and paraffins) to delineate the effects of individual components on catalytic activity.

1.4.4 Thermodynamics of POX

A thermodynamic analysis of POX is necessary to establish the conditions that will maximize synthesis gas (H_2 and CO) yields while minimizing carbon. Such an analysis was performed by Shekhawat et al. for the POX of n-C_{16} to examine the effect of O/C ratio and temperature on reformate product distribution [17]. The calculations were made using a Gibb's free energy minimization technique by HSC Chemistry Thermodynamic Software [45], and the results (equilibrium amount) were normalized to 1 mole of n-C_{16} fed to the reactor. In addition to these parameters, the effect of pressure was examined using the same HSC software [45]. Conversion of hydrocarbon was complete for each case.

1.4.4.1 Effect of O/C Ratio

Figure 1.5 shows the effect of O/C ratio on synthesis gas selectivity and carbon formation. Conversion of hydrocarbon was complete for each case. At low O/C ratios, carbon formation is thermodynamically favorable. However as the O/C approaches 1.1, sufficient O_2 is available to decrease the driving force for carbon formation while still maintaining high H_2 and CO yields. Then, as stated earlier, the selectivity towards

synthesis gas decreases as the O/C approaches an O_2 rich environment (as O/C→1.5) because H_2O and CO_2 become thermodynamically favorable products. Thus, an optimal O/C ratio for carbon free operation and high synthesis gas yields is roughly 1.2.

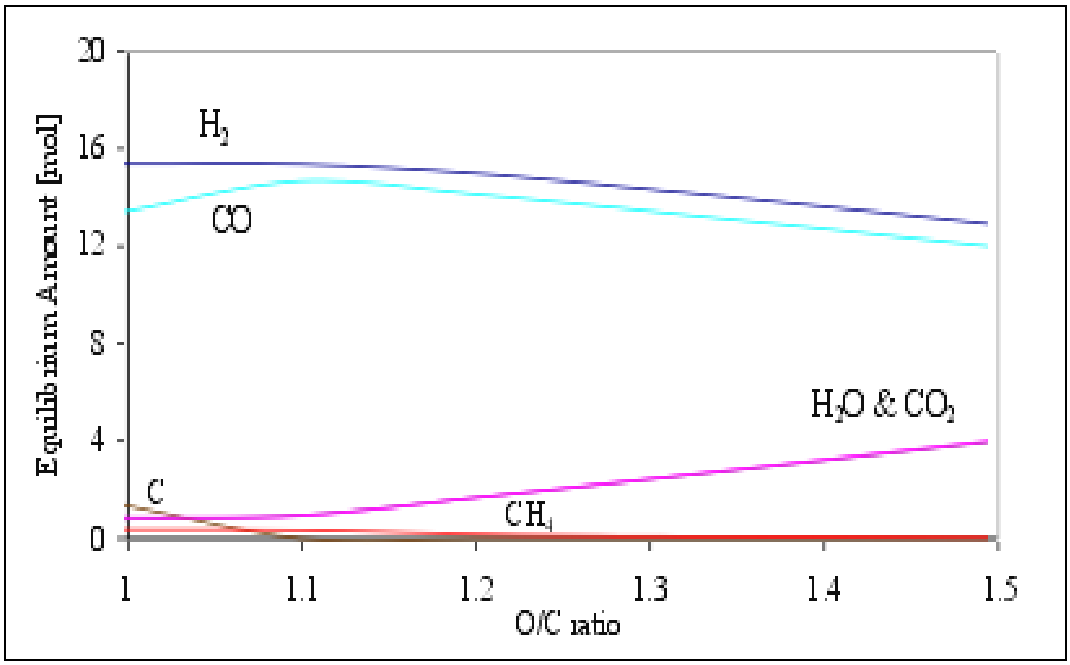

Figure 1.5 Effect of O/C ration on the product distribution for the POX of n-C_{16} at 800°C and 1 atm. Figure taken from Shekhawat et al [17].

1.4.4.2 Effect of Temperature

The effect of temperature on reformate product composition and carbon formation is shown in **Figure 1.6** at O/C of 1.2 and P=1 atm. At low temperatures (~500°C) conditions are favorable for carbon formation and synthesis gas yields are low. However, as temperature is increased, carbon formation becomes unfavorable (at T ≥ 750°C) and H_2 and CO yields are maximized. Thus, at an O/C of 1.2 and P= 1 atm, it is desirable to run CPOX at elevated T ≥ ~800°C to obtain thermodynamically high yields of synthesis gas with no carbon.

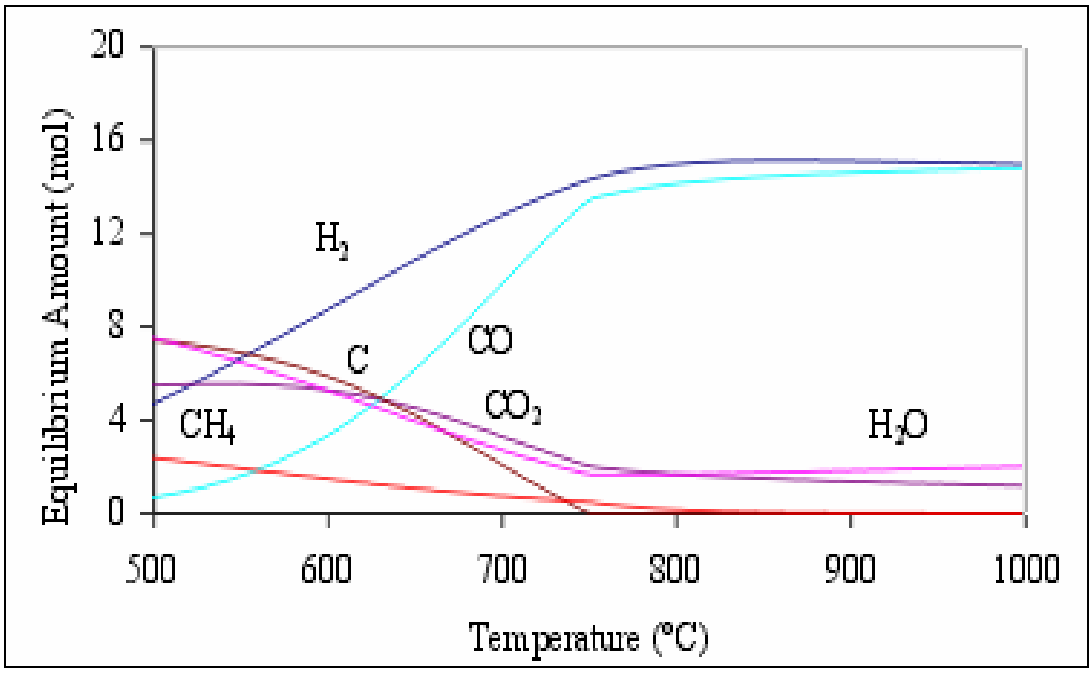

Figure 1.6 Effect of temperature on product distribution of POX n-C_{16} at an O/C of 1.2 and P= 1 atm. Figure taken from Shekhawat et al. [17].

1.4.4.3 Effect of Pressure

Figure 1.7 illustrates the effect of pressure on the reformate gas products after the POX of n-C16 at 800°C and an O/C of 1.2. As can be seen, the production of H_2 and CO decreases with increasing pressure. This is likely due to the increase in moles that form as the hydrocarbon is reacted. An optimal pressure range for the reaction at the elevated temperatures is somewhere between 1-2 atm to obtain the highest synthesis gas yields.

1.5 Catalytic Partial Oxidation (CPOX) Literature Studies

From a practical perspective, the CPOX of logistic fuels should be used in smaller scale applications, i.e. fuel processing for transportation or remote power, because the reformer has less spatial requirements and lower construction costs [9].

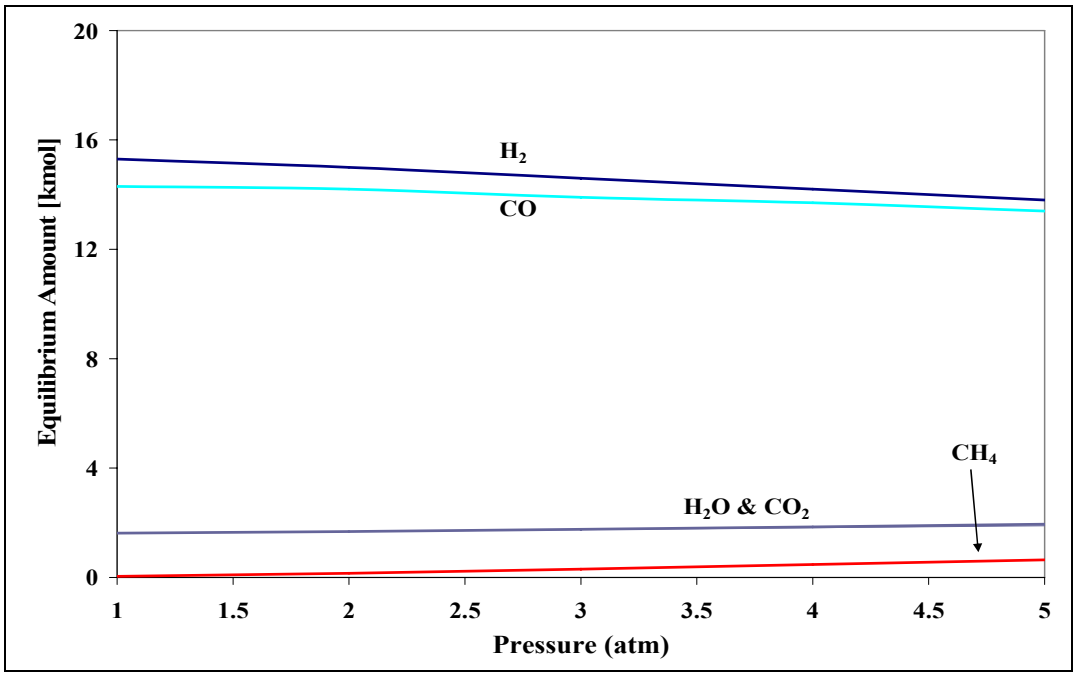

Figure 1.7 Effect of pressure on product distribution of POX of n-C_{16} at an O/C of 1.2 and T=800°C.

As the reaction is exothermic, optimal thermal integration would require a partial oxidation reformer to be used in conjunction with high temperature cells like an SOFC, rather than a low temperature PEM. As stated before, there are several areas that have emerged as niche markets for SOFC implementation: auxiliary power units (APU's) for long haul diesel trucks and remote power generation [14, 15, 26, 27, 46]. The life-time requirement for such applications is roughly 5000 hours of operation [27]. In either of these applications, the CPOX of logistic fuels offers an attractive solution as an H_2 energy supply [26, 27, 46]. Therefore, as advances in SOFC design bring the technology closer to commercialization, a long-life CPOX reformer is needed.

Studies of the CPOX of diesel and diesel surrogate fuels have been reported in the literature. Much of the work in the CPOX of liquid fuels has been performed by the

Schmidt group the at University of Minnesota. Some of their work is summarized in **Table 1.8** below.

Table 1.8 Examples of CPOX of diesel or diesel surrogate fuels in the literature.

Author	Fuel	O/C	Catalyst	H_2 Selectivity	CO Selectivity	Conversion
Schmidt et al. [28].	C_6H_6, n-C_6, i-C_8, n-C_{10}	1	Rh on wash-coated alumina	60-95% depending on fuel	55-95% depending on fuel	~ 100% for each fuel
O'Connor et al. [30].	n-C_6, i-C_8	1	Rh on wash-coated alumina	>90% for each fuel	>85% for each fuel	>95% for each fuel
Krummenacher and Schmidt [47].	n-C_{10}	1.25	Rh or Pt on wash-coated alumina	>85% for Rh[a] n.d. for Pt[a]	>85% for Rh[a] >15% for Pt[a]	>99% for Rh > 80% for Pt
Krummenacher et al. [44].	n-C_{10} n-C_{16} diesel	1.25, 2.25 for diesel	Rh on wash-coated alumina	>85%[a] for n-C_{10}, >75%[a] for n-C_{16}, >70%[b] a for Diesel	>85%[a] for n-C_{10}, >70%[a] for n-C_{16}, >80%[b] for Diesel	>94% for each fuel
Shekhawat et al. [42]	n-C14	1.2	Rh/ZDC[c] Pt/Al_2O_3 Pt/ZDC[c]	>80% for Rh/ZDC, >80% for Pt/Al_2O_3, >65% Pt/ZDC	>80% for Rh/ZDC, >81% for Pt/Al_2O_3, >65% for Pt/ZDC	>95% for all catalysts

a- at 4 SLPM feed rate

b- at 2 SLPM feed rate

c- ZDC- zirconium doped ceria

From Table 1.8 it can be observed that the CPOX of fuels is capable of high synthesis gas yields, with greater than 95% conversion of fuel with an appropriate catalyst. However many of these studies are only parametric analyses of the operating

conditions for CPOX. This is mainly due to the fact that the longer term studies are hindered by catalyst deactivation by the aromatics and sulfur compounds commonly found in diesel.

1.6 Catalysts for POX

1.6.1 Traditional CPOX Catalysts

CPOX catalysts are typically Ni [24] or Group-VIII noble metals [28, 30, 40, 44, 48] incorporated onto various high surface area oxide substrates such as γ-Al_2O_3, SiO_2, and more recently, mixed metal oxides [42, 49]. The metal is dispersed onto the support surface in small crystallites to maximize the amount of active metal exposed. As seen in Table 1.8, rhodium has been identified as the superior metal for CPOX due to its high H_2 and CO selectivities [44, 50-52]. This behavior is believed to be directly related to the high bond strength of Rh metal with surface oxygen, which prevents the reaction between surface oxygen and dissociated hydrogen atoms on the surface into hydroxyl radicals, and eventually into water [47]. Also Rh metal has shown a higher resistance to carbon formation compared to other metals [30, 42, 53].

However this design of the catalyst may be predisposed to carbon formation and deactivation by sulfur. The adsorption of sulfur and carbon has been shown to be structure sensitive [54]. Specifically, both carbon and sulfur adsorption have been linked to the metal cluster size, with larger cluster sizes more prone to deactivation [39, 54, 55].

1.6.2 Mixed Oxides as Alternative Catalysts

The development of a catalyst with spatially distributed active metal components in the structure may provide a more durable catalyst compared to the traditional alternative. Dispersing the metal throughout the structure would avoid the metal clusters at the surface that are favorable sites for sulfur and carbon adsorption, and thus may make the catalyst less susceptible to deactivation. Mixed metal oxides have become increasingly popular because of the ability to substitute different metals into their structure and maintain catalytic activity [56-58]. For example, the work of Gardner et al. [56] demonstrated the ability to effectively incorporate Ni into a hexaluminate structure $ANi_{0.4}Al_{11.6}O_{19-\delta}$ (A = La, Sr and Ba) and successfully partially oxidize n-tetradecane with reduced carbon formation. Further, Liu and Krumpelt [57] have shown that the incorporation of Ru into a perovskite type structure ($LaCr_{0.95}Ru_{0.05}O_3$) is catalytically active for the ATR of dodecane while exhibiting sulfur tolerance.

However, the substitution is not only limited to transition metals. Additional, lower valence elements (typically rare earth metals) can be substituted into the structure to create oxygen vacancies to increase oxygen ion mobility in the bulk material [57, 59]. Oxygen mobility has been identified as a mechanism that can reduce carbon accumulation on the surface in reforming reactions. Erri et al. [60] reported that the addition of cerium to nickel containing perovskite ($La_{0.6}Ce_{0.4}Fe_{(1-x)}Ni_xO_3$) greatly reduced carbon formation in ATR of JP-8 military fuel. In essence, the defects cause O_2 ions to be more weakly bound in the bulk material, and in doing so, O_2 can be released from the structure to the metal and oxidize the carbon from the surface.

1.6.3 Pyrochlores as a Novel CPOX Catalyst

Another class of mixed oxides, known as pyrochlores, shows potential to incorporate noble metals and other elements to form a catalyst that may endure the rigorous conditions in the CPOX of logistic fuels. A pyrochlore, similar to a perovskite, is a derivative of the fluorite structure. It is composed of ½ trivalent cations and ½ tetravalent cations in a cubic unit cell structure, shown in **Figure 1.8**, with the general stoichiometry $A_2B_2O_7$ [59]. The A-site is usually a large cation (typically rare earth elements) and is coordinated with 8 oxygen anions. The B-site cation has a smaller radius (usually transition metal) and is coordinated with 6 oxygen atoms. In order to form a stable pyrochlore, A and B cations must have an ionic radius ratio $rr=r_A/r_B$ between 1.4-1.8 [61].

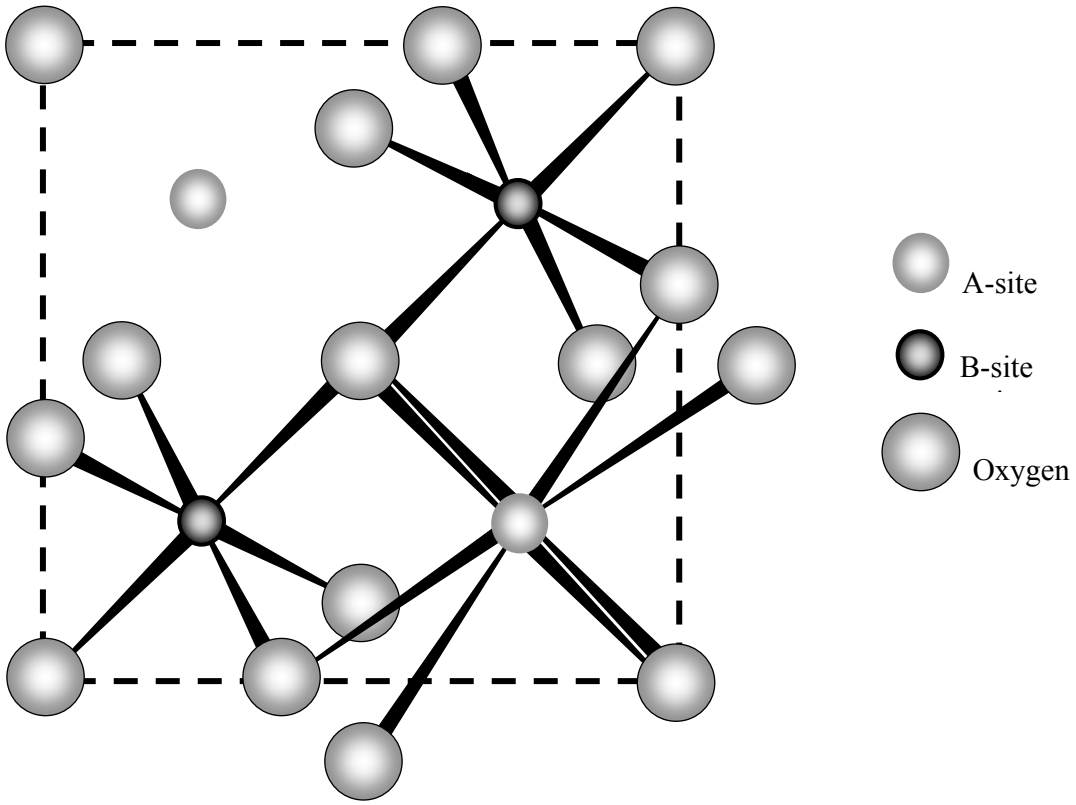

Figure 1.8 General unit cell structure of $A_2B_2O_7$ pyrochlore. Figure adapted from [61].

Both A and B sites can be exchanged for lower valence elements to create defects in the crystal structure (oxygen vacancies) to improve the lattice oxygen mobility [57, 60, 62]. Also, a reforming metal can be exchanged into the B-site to obtain a highly dispersed metal at the surface that is anchored into the structure [57].

In choosing an appropriate material for CPOX, the pyrochlore must maintain chemical and thermal stability at reaction conditions. As a catalyst for CPOX, $La_2Zr_2O_7$ lanthanum zirconate (LZ) pyrochlores are of considerable interest. Although the material has not been used for reforming applications to my knowledge, it has shown remarkable physical properties that suggest it is an attractive option as a CPOX catalyst. The material is currently being investigated as an alternative to yttrium stabilized zirconia (YSZ) as a thermal barrier coating for turbine engines because it has a high melting point and chemical stability [63-66]. It also has shown the mechanical strength to accommodate metal substitution to improve oxygen ion conductivity [65].

These features of LZ, along with the appropriate substitution of metals into the structure may create a thermally and chemically stable catalyst for the CPOX of liquid fuels. The substitution of rhodium into the B-site of the LZ structure may lead to well-dispersed metal particles that are highly active for the CPOX reaction. Metal incorporation may also alter the properties of the Rh-metal to decrease the driving force for irreversible carbon formation and sulfur poisoning that normally occurs on larger metal clusters. In addition, the exchange of A-site La^{3+} with Sr^{2+} may create structural defects that may increase lattice oxygen mobility in the bulk material to aid in the reduction of carbon formation.

1.7 Scope of Work

The purpose of the research described here was to synthesize, characterize and examine the CPOX activity of a $La_2Zr_2O_7$ pyrochlore substituted with Rh metal only as well as Rh and Sr together. Characterization will be discussed in Chapter 3 and includes: ICP to determine composition, XRD to examine phase of material, BET surface area, SEM and microanalysis, temperature programmed reduction (TPR), dispersion and mass transfer limitations. Chapters 4-7 discuss the effects of substitution on catalytic activity and its role in reducing deactivation by carbon and sulfur poisoning. Chapter 4 discusses the activity screening by the CPOX of n-tetradecane (TD) only. Chapter 5 examines ability to reform polynuclear aromatics using a 5 wt% mixture of 1-methylnaphthalene (MN) in TD. Chapter 6 discusses sulfur tolerance with a mixture of 1000 ppmw of dibenzothiophene (DBT) in TD. Finally Chapter 7 looks at the effect of the combination of 5 wt% MN and 1000 ppmw DBT in TD. In each case, the results of the experiments are compared to that of a supported $Rh/\gamma\text{-}Al_2O_3$ catalyst to demonstrate the effect of substitution.

Chapter 2. Experimental Section

2.1 Catalyst Synthesis

The pyrochlore catalysts shown in **Table 2.1** were prepared using a variation of the Pechini method [67-70], which is a synthesis route to produce mixed metal oxide compounds through a solid-gel (solgel) intermediate phase. It was chosen because it is a simple and fast method to produce highly uniform non-substituted and substituted catalyst crystals.

Table 2.1 Theoretical composition and metal loading of pyrochlore catalysts.

	$La_2Zr_2O_7$ (LZ)	$La_2Rh_{0.11}Zr_{1.89}O_{7-y}$ (LRZ)	$La_{1.5}Sr_{0.5}Rh_{0.10}Zr_{1.90}O_{7-y}$ (LSRZ)
Oxygen Stoichiometry (y)	0	0.055	0.30
Rh Loading (wt%)	0	2.0	2.0

Nitrate hydrates $La(NO_3)_3•6H_2O$ (GFS Chemicals), $ZrO(NO_3)_2•XH_2O$*, $Rh(NO_3)_3•2H_2O$*, and $Sr(NO_3)_2$* (* Alfa Aesar) were used as metal precursors. The metal nitrates were weighed according to the atomic ratio of the desired catalyst composition and dissolved separately in de-ionized (DI) water. The dissolved salts were then combined into a 1L beaker containing 0.1L of DI water. Citric acid (CA) was then added to the beaker as a chelating agent to form metal complexes in the solution. A 1:1 molar ratio of CA:metal was used to allow for complete metal complexation. The solution was then heated to 75°C while being stirred with a magnetic stir bar to ensure chelate formation and to remove nitrogen oxides and water. Once at 75°C, a 40:60 molar ratio of ethylene glycol to CA was added to disperse the metal complexes throughout the

solution via a polyesterfication reaction. The solution was further dried on the hot plate at 75°C until the liquid evaporated and a solid-gel like material remained. The gel-like material was then transferred to a crucible and placed in an oven at 110°C to dry overnight. Following drying the catalysts were calcined at 900°C for 5 hours to burn off organic species and to form the crystalline pyrochlore phase.

The $Rh/\gamma\text{-}Al_2O_3$ catalyst was obtained commercially from Alfa Aesar (Stock # 42507). Rhodium metal loading was 0.51 wt % and the alumina pellet size was 3mm.

2.2 Catalyst Characterization

2.2.1 ICP

An elemental analysis was performed using inductively coupled plasma (ICP) to determine the composition of the three pyrochlores. To ensure accuracy, duplicate samples of 0.1g catalyst were digested in molten lithium tetraborate in platinum crucibles at 950°C. They were then dissolved in warm, dilute hydrochloric acid to a final volume of 250 ml. The samples were analyzed on a Perkin Elmer Optima 3000 Radial View Inductively Coupled Plasma - Optical Emission Spectrometer (ICP-OES).

2.2.2 X-Ray Diffraction

Phase analysis of powder samples was examined using a PanAnalytical X'pert Pro X-Ray diffraction system, model number PW 3040 Pro. The device consisted of a ceramic diffraction X-ray tube containing Cu Kα radiation at a wave length of Kα (Å) 1.54184. Power requirements during operation were 45 kV and 40 mA. The divergence

slit angle for the incident X-ray beam was set to 1/2° and the anti-scatter slit was 1/4°. The receiving slit of the diffracted beam was 2°.

Three pyrochlores: LZ, LRZ, and LSRZ, were analyzed pre- and post-CPOX reactions to determine the phase of fresh material and the phase stability of the material after being exposed to the high reaction temperatures. Powder scan programs were the same for each catalyst: 2θ scanning range was 10-80° at scan speed of 0.0025°/s, which gave a total scan time of 7:46:43. Subsequent peak identification of the X-ray data was performed using X'pert High Score Plus software, version 2.1. Then the scan was analyzed and compared to similar X-ray patterns provided in the programs database.

2.2.3 BET Surface Area and Average Pore Size

Before analysis, all catalyst powders were pre-treated by a Quantachrome AUTOSORB-6 degasser. The unit consisted of 6 sample stations, each with individual heating and vacuum control. 1.6g of pyrochlore powder and 0.18g $Rh/\gamma\text{-}Al_2O_3$ were loaded into quartz tubes and degassed under 5 mtorr at 150°C overnight to remove water and other impurities.

BET surface area experiments were performed in a Quantachrome AUTOSORB-6 gas adsorption unit. The unit contained 6 sample stations, each equipped with an individual Dewar flask filled with liquid nitrogen. The adsorption isotherm consisted of a 40 point analysis of P/Po versus volume adsorbed (cc/g) to increase the accuracy of the surface area. Nitrogen adsorption occurred over a P/Po range 0.054 to 0.15 at -204°C (77 K). In addition, the average pore size was determined from a pore size distribution measurement that was made using the BJH method.

2.2.4 Temperature Programmed Reduction/Dispersion Analysis

Temperature programmed reduction (TPR) and dispersion analysis experiments were carried out in a Micromeritics Autochem 2910 unit. A schematic of the instrument used is illustrated in **Figure 2.1**. Sample gases 5% H_2/Ar, 2% O_2/He, and Ar were connected to inlet ports 1, 2, and 3 in the preparation, carrier and loop sections, respectively. To measure concentration changes, the unit consisted of dual thermal conductivity detectors (TCD) to monitor the change in thermal conductivity between the gas after it flows over the sample and a reference gas stream. The catalyst samples were placed in a U-shaped quartz tube, and held in place by quartz wool. A thermocouple ran axially down the tube and was placed in the middle of the sample, or as close as possible depending on the sample size.

2.2.4.1 Temperature Programmed Reduction (TPR)

TPR studies were performed on four catalysts: LZ, LRZ, LSRZ, and Rh/γ-Al_2O_3. The sample weight was the same, 0.35g, for each catalyst. Before the start of the TPR, each catalyst was oxidized to burn off any impurities or organic material that may have remained on the surface from the synthesis. The sample was ramped up to 900°C at 15°C/min under 50 sccm of 2% O_2/He, and held at 900°C for 10 minutes. After oxidation, the catalyst was purged with 50 sccm of Ar at 900°C for 15 minutes. Next the sample was cooled, still under Ar, down to 100°C at 90°C/min to begin the TPR. Once at 100°C, the gas composition was changed to the mixture of 5% H_2/Ar at a flow rate of 15 sccm. The sample was then ramped from 100°C to 950°C by 5°C/min under the 5% H_2/Ar mixture and held isothermally at 950°C for 30 minutes.

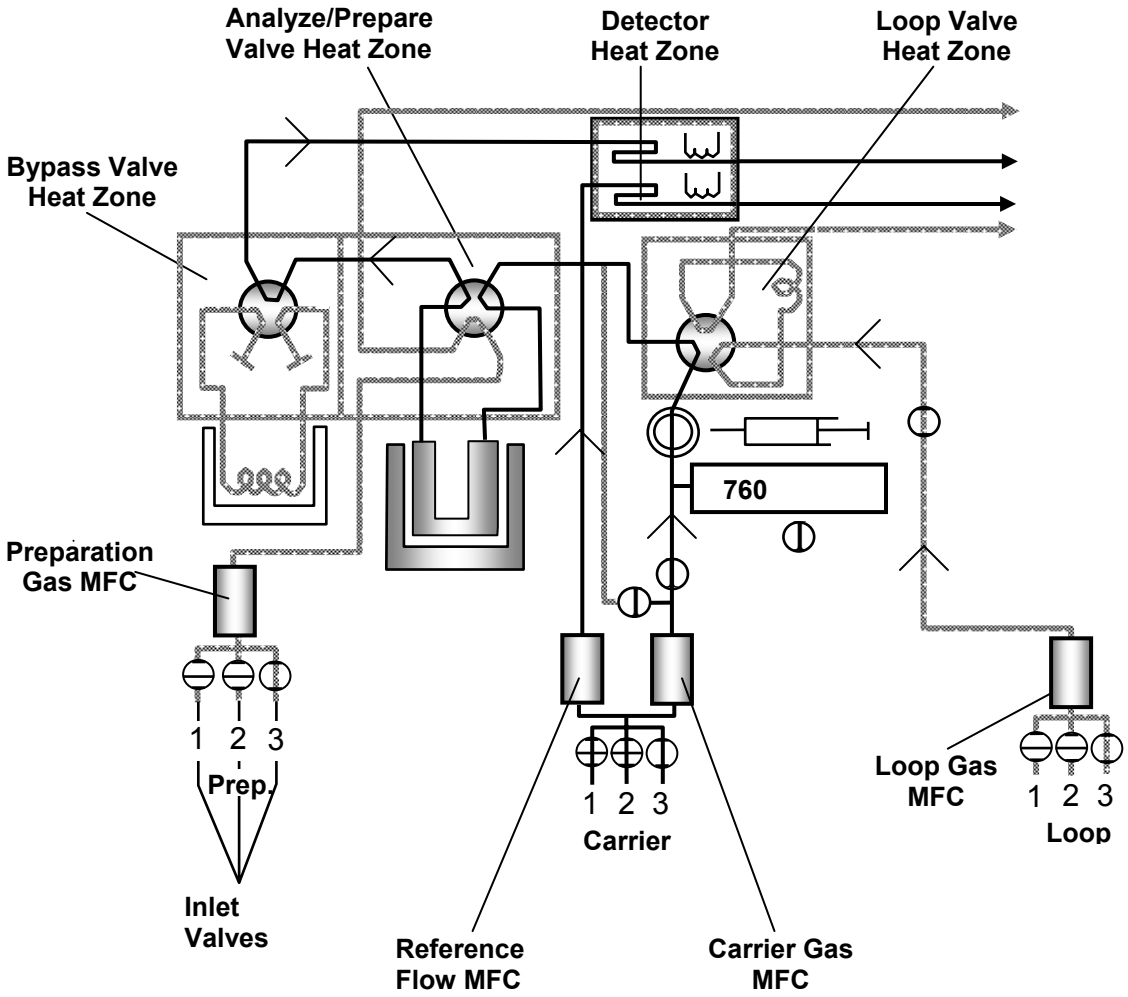

Figure 2.1 Schematic of Micromeritics unit used to perform TPR and Dispersion studies.

2.2.4.2 Dispersion

Metal dispersion for three catalysts, LRZ, LSRZ, and Rh/γ-Al_2O_3 was determined by the pulse chemisorption of H_2. For dispersion analysis, the unit contained a sample loop with a volume of 0.5377cm^3 to dose catalyst with the H_2 gas. During pulse chemisorption experiments, the sample was purged with carrier gas Ar while the loop gas (5% H_2/Ar) purged the sample loop until the time of injection. Once the pulse was

initiated, the loop valve opened and the H_2 gas mixture was forced over the sample by the carrier gas. After dosing, the loop valve closed and loop was purged with the 5% H_2/Ar mixture to prepare for another dose.

The mass of sample used for this experiment was the same for all experiments, 0.2g. Before chemisorption experiments, the catalyst was reduced under H_2 to remove surface oxygen. To reduce the catalyst, the sample was ramped to 700°C by 20°C/min under 25 sccm 5% H_2/Ar and held at temperature for 10 minutes. After reduction, the catalyst was purged under Ar at 700°C for 30 minutes to desorb H_2 from the surface. The sample was then cooled to 50°C, under Ar, by 50°C/min to begin H_2 chemisorption. At 50°C the system was purged under Ar until the TCD's read a stable baseline. Once stable, the catalyst sample was dosed with 0.5377 sccm 5% H_2/Ar for 2 minutes. The dosing process was repeated until the peaks areas were equal. In analyzing the data, a 1:2 stoichiometric ratio of H_2:metal was used [71, 72].

2.2.5 Scanning Electron Microscopy and Electron Dispersive X-ray Analysis

Electron Microscopy and X-ray microanalysis were performed in a JEOL FESEM-6300 Field Emission Electron Microscope. The microscope was coupled with a Thermo-Electron (Thermo-Noran) System Six X-ray Ultra Dry EDX detector (model no. 6650D-1UPS-SN). Detector calibration was completed utilizing the Cu Kα at 8.046 KeV. The electron beam accelerating voltage used during microanalysis analysis was set to 10 kV, which was well over the 4.65 kV needed to detect the n-line for the largest molecule, La. Before imaging and EDX, samples were dispersed onto an adhesive graphite tape. To ensure optimal visual and microanalysis capabilities the samples were plasma-coated with gold in a Bio-Rad SEM coating system.

2.3 CPOX Activity Measurements

2.3.1 Reactor

The schematic of the fixed bed continuous-flow reactor (Autoclave Engineers, Model no. BTRS Jr) used to screen catalyst activity is illustrated in **Figure 2.2**. Two 2000 sccm Brooks mass flow controllers (model no. 5890E) were used to deliver N_2 and air to the system with reported error of ± 1% range of controller. The hydrocarbon fuel was fed to the reactor by an HPLC pump (Dionex Corp., Model no. P680A HPG) with a reported accuracy of ± 1%. Carbon balances for all experiments were 100 ± 5%. The inlet gases passed through pre-heating coils then combined before the reactor inlet. The coils served to provide a longer residence time in the hot box to ensure complete vaporization of the fuel and thorough heating of the gases. N_2 was used as a carrier gas to transport the vaporized hydrocarbon to the reactor inlet, where the fuel/N_2 and air combined before they entered the catalytic reactor. A furnace, or hot box, surrounded the reactor components to vaporize the fuel and maintain uniform inlet and product gas temperatures. The hot box temperature was set to 375°C and controlled by a programmable temperature controller (Eurotherm, Model no. 2416). Catalysts were placed in an 8 mm i.d. tubular reactor with an axially centered thermocouple. A split tube furnace (Series 3210, Applied Test Systems, Inc.) encapsulated the reactor and the temperature was controlled by a programmable controller (Eurotherm, Model no. 2416). The catalyst was diluted with quartz sand (5/1 by weight), of the same particle size as the catalyst, to minimize temperature gradients and channeling throughout the bed.

2.3.2 Product Analysis

The dry gas products: H_2, CO, CO_2 CH_4 and N_2 were analyzed continuously by means of an online Thermo Onix mass spectrometer (Model no. Prima δb, a 200 a.m.u. scanning magnetic sector) with standard ± 2% analytical error in gas concentration results. Larger hydrocarbon products were analyzed with an HP5890 gas chromatograph (± 2% error was assumed in response factor) equipped with a flame ionization detector (FID). 5 GC samples were taken over the course of a 5 hour experiment: the first at steady state, then one per hour as the experiment progressed. Steam concentration was not measure analytically; however, it was estimated indirectly from mass balance calculations of hydrogen and oxygen- containing species in the product stream.

The following equations (4.1-4.3) were used to calculate the data presented in Chapters 4-7. The yield of each dry gas product, i.e. H_2, CO, CO_2, and CH_4 was calculated by equation 4.1.

$$\text{Yield of A (\%)} = \frac{\text{Moles of A produced x 100}}{\text{N x moles of hydrocarbon fed to the reactor}} \qquad 4.1$$

Where N is the number of moles of H_2 per mole of hydrocarbon for H_2 yields and is the number of moles of carbon in the hydrocarbon fuel for yields of carbon containing products.

Hydrocarbon (HC) and olefin yields were determined using equation 4.2.

$$\text{HC/Olefin Yield (\%)} = \frac{\text{Moles of HC or olefin produced x 100 x i}}{\text{N x moles of hydrocarbon fed to the reactor}} \qquad 4.2$$

Where i is the number of moles of carbon per mole of hydrocarbon in the product (i.e. i would be 2 for ethane) and N is the number of moles of carbon in the hydrocarbon fuel.

A carbon balance was calculated by equation 4.3.

$$\text{Carbon balance}\,(\%) = \frac{(CO + CO_2 + \sum_{i}^{i=1\text{-}6} iC_iH_r)\ \text{x}\ 100}{\text{N x moles of hydrocarbon fed to the reactor}} \qquad 4.3$$

Where i is the number of moles of carbon per mole of hydrocarbon in the product (i.e. i would be 2 for ethane), N is the number of moles of carbon in the hydrocarbon fuel and r is the number of hydrogen atoms contained in the hydrocarbon product.

Steam formation was not measured directly using the analytical equipment. However it was evaluated by assuming the unconverted H_2 and O_2 molecules were in the correct ratio (2/1) to assume steam was forming. The unconverted H and O values were obtained by a mass balance over inlet and exiting species containing H and O. The mole balances were calculated by the following equations:

$$H_2\ \text{balance(mol/s)} = TD_{in}\ \text{x}\ 15 - H_{2\,out} - \sum_{i}^{i=1\text{-}6} rC_iH_r - (1 - \frac{CB}{100})\ \text{x}\ TD_{in}\ \text{x}\ 12\ \text{x}\ 2 \qquad 4.4$$

$$O_2\ \text{balance(mol/s)} = O_{2\,in} - CO_2 - \frac{CO}{2} \qquad 4.5$$

Where r is the number of hydrogen atoms contained in the hydrocarbon product, and the $(1 - \frac{CB}{100})\ \text{x}\ TD_{in}\ \text{x}\ 12\ \text{x}\ 2$ term is the H_2 associated with unconverted hydrocarbon: CB is the carbon balance and a 2/1 ratio of hydrogen to carbon in the unconverted fuel was assumed.

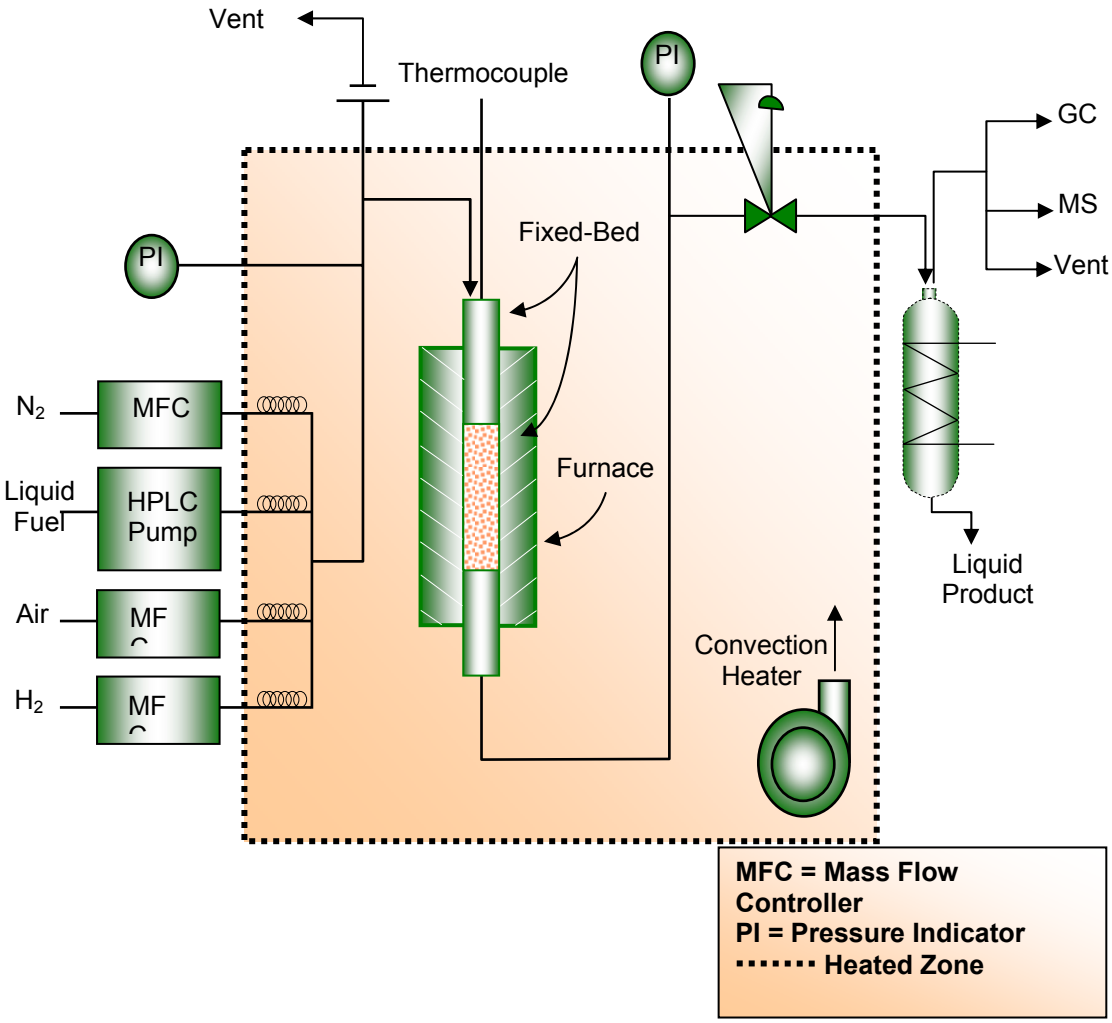

Figure 2.2 Schematic of catalyst testing system.

2.3.3 External Mass Transfer Limitations

In the presence of external mass transfer limitations, the transport of reactants from the bulk fluid to the catalyst surface controls the observed rate of reaction [71].

$$r_{obs} = \bar{k}_c (C_{AB} - C_{AS}) \qquad 2.3.1$$

The limitations are mainly due to diffusional resistances through the boundary layer that surrounds the catalyst particle. A mass transfer correlation, derived elsewhere [71], shows the mass transfer coefficient for the transport of reactants to the catalyst surface can be put in terms of adjustable process variables.

$$\bar{k}_c \alpha \frac{(D_{AB})^{2/3} u^{1/2} \rho^{1/6}}{(R_p)^{1/2} (\bar{\mu})^{1/6}} \qquad 2.3.2$$

Where D_{AB} is the binary diffusion coefficient, u is the linear velocity, ρ is the fluid density, R_p is particle radius, and μ is the fluid viscosity. From this relationship, external transport limitations can be quantified by varying the linear velocity while keeping the overall weight hourly space velocity (WHSV) the same. The catalyst weight must also be increased by the same magnitude as the fluid velocity to maintain the same WHSV.

A series of CPOX experiments were performed on the Rh/γ-Al_2O_3, to determine the extent of external mass transfer resistance in the tubular reactor. The flow rates and catalyst mass were calculated such that the WHSV would be similar to that which was used during the CPOX reforming studies. The flow rates and mass of samples are shown in **Table 2.2**.

Table 2.2 Flow rates for external mass transport studies.

Run	**Weight** (mg)	**N_2** (sccm)	**n-TD** (ml/min)	**Air** (sccm)	**WHSV** (scc g_{cat}^{-1} h^{-1})
A	280	29	0.057	199	50,000
B	380	40	0.078	270	50,000
C	480	50	0.099	342	50,000
D	580	61	0.119	413	50,000

2.3.4 Internal Mass Transport Resistances

In the presence of internal mass transport limitations diffusion resistances of the reactants inside the catalyst particle can inhibit the rate of reaction. The Thiele Modulus is a dimensionless expression that can indicate if internal transport limitations are present.

$$\phi = R_p \sqrt{\frac{k}{D^e_{TA}}} \qquad 2.3.3$$

Where R_p is particle radius, k is the reaction rate constant, and D^e_{TA} is the effective diffusivity. These parameters (R_p, k, D^e_{TA}) are estimated to calculate a value for the Thiele Modulus, which is then used in the following expression for the effectiveness factor (η) to evaluate the extent of internal mass transport limitations in the system.

$$\eta = \frac{robs}{rmx} = \frac{3}{\phi}\left[\frac{1}{\tanh(\phi)} - \frac{1}{\phi}\right] \qquad 2.3.4$$

If $\phi \leq 1$, then no internal transport limitations and $\eta \sim 1$

If $\phi > 1$, then internal limitations exist and $\eta < 1$

It should be noted that some assumptions are necessary to calculate the parameters for the Thiele Modulus. Those made will assume the worst case scenario for internal transport limitations to occur, so that if transport limitations do not exist for the worst case conditions, then they will not exist at others which are less conducive for internal mass transport resistances.

2.3.5 CPOX Studies

Four experiments were performed on each catalyst using model compounds to simulate logistic fuels. n-Tetradecane (TD) was used to represent the paraffin component of the fuel, and 1-methlynaphthalene (1-MN) and dibenzothiophene (DBT) were used to simulate aromatic and organic sulfur compounds, respectively. The CPOX of TD only was used to examine the catalyst activity and selectivity. A mixture of 5 wt% 1-MN/TD was then used to simulate the effects of aromatic compounds. Next, the sulfur tolerance was examined by the CPOX of 1000 ppmw of DBT/TD. Finally, a mixture of 5 wt % 1-MN + 1000 ppmw DBT was used to verify the combined effects of the contaminants on the catalysts. Experimental conditions for these experiments are detailed below in **Table 2.3**.

Table 2.3 Experimental conditions for CPOX experiments.

Feed Concentration		mmol/L	mol %
	N_2	36.0	80.1
	O_2	8.0	17.8
	TD	0.95	2.1
O/C	1.2		
WHSV (scc g_{cat}^{-1} h^{-1})	50,000		
Temperature (°C)	900		
Catalyst Bed (mg)	480		
Pressure (MPa)	0.23		

After CPOX experiments a temperature programmed oxidation (TPO) was performed to determine the amount of carbon deposited on the spent catalyst. The carbon was oxidized by passing a 5 % mixture of O_2/N_2 over the catalyst while it was heated

from 200°C to 900°C by 1°C/min. The catalyst was left at 900°C overnight and cooled to ambient in the morning. CO_2 emissions were measured by an online mass spectrometer.

Chapter 3. Results and Discussion: Pre-CPOX Catalyst Characterization

3.1 ICP

The compositions of the three mixed oxide pyrochlores synthesized by the Pechini method are shown in **Table 3.1**. The measured elemental compositions are compared to the theoretical to show the accuracy of the Pechini method.

Table 3.1 Elemental analysis with ICP.

Catalyst Designation		**LZ**	**LRZ**	**LSRZ**
Composition	T	$La_2Zr_2O_7$	$La_2Rh_{0.11}Zr_{1.89}O_{6.95}$	$La_{1.5}Sr_{0.5}Rh_{0.10}Zr_{1.90}O_{6.7}$
	A	$La_{2.31}Zr_{1.82}O_{5.14}$	$La_{2.28}Rh_{0.025}Zr_{1.62}O_{6.45}$	$La_{1.67}Sr_{0.54}Rh_{0.03}Zr_{1.66}O_{7.07}$
Wt % La	T	48.6	48.6	38.4
	A	56.3	55.3	42.7
Wt % Sr	T	0.0	0.0	8.0
	A	0.0	0.0	8.7
Wt % Rh	T	0.0	2.0	2.0
	A	0.0	0.45	0.59
Wt % Zr	T	31.9	30.0	31.9
	A	29.4	26.2	28.0

T= Theoretical; A= Actual average of two samples.

3.2 X-Ray Diffraction

The X-ray diffraction patterns for the pyrochlore catalysts after calcination are shown in **Figure 3.1**. LZ material demonstrates a single-phase, cubic unit cell structure distinctive to the pyrochlore material and resembles similar patterns seen in the literature [65, 73]. The similar pattern for LRZ indicates the metal concentration of Rh^{+3} is low enough that substituting for the B-site Zr^{+4} ions does not result in any peak shifts or phase changes in the bulk crystalline properties of the material. Sr substitution, however, results in a multi-phase perovskite-pyrochlore material. The displacement of La^{+3} ions

by Sr^{+2} forms a hexagonal $SrZrO_3$ perovskite phase in addition to the pyrochlore. Evidence of this can be seen by certain peaks in the LSRZ diffraction pattern at 31°, 45°, 55°, 65°, and 73° that have been identified in the literature to be characteristic to the $SrZrO_3$ perovskite [74].

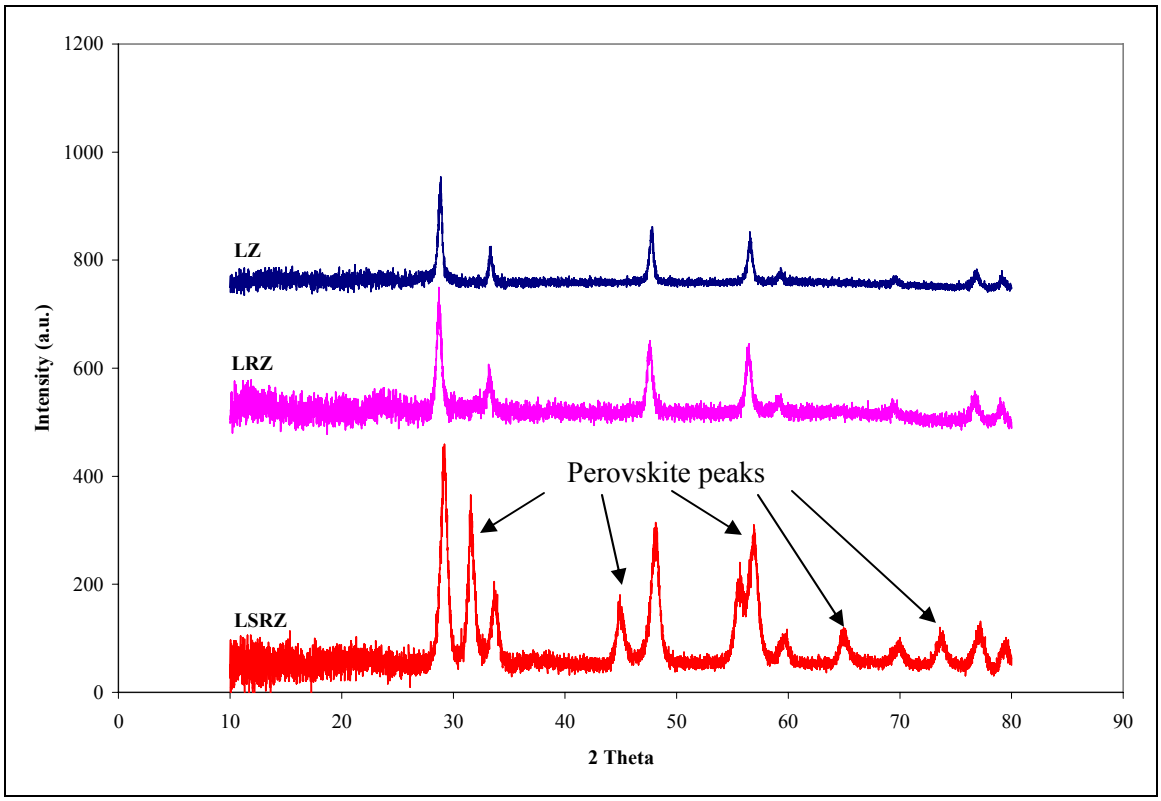

Figure 3.1. XRD diffraction patterns illustrating the structural changes on LZ after substitution of Rh only, and Rh and Sr.

3.3 BET Surface Area and Average Pore Size

BET surface area values and average pore sizes for each catalyst are presented in **Table 3.2**. It is obvious from the data that surface area is inversely related to pore size. This relationship is to be expected because the total surface area of the particle is equal to the summation of all individual pore wall areas [75]:

$$A_{tot} = A_i + A_{i+1} + \ldots + A_{i+n}, \text{ where } A_i = \frac{4V_i}{D_i} \text{ (assuming cylindrical geometry)}$$

and a sample with small pore sizes has a larger surface area due to the larger number of individual pore areas that can be combined into the overall area. Thus, each of the pyrochlores has a surface area an order of magnitude smaller than the supported Rh/γ-Al_2O_3 because of their much larger pore size compared to the alumina support. Also, substitution of Rh and Sr ions into the structure has little effect on surface area for the pyrochlore.

Table 3.2 BET surface areas and average pore diameters of rhodium and pyrochlore catalysts.

Catalyst	BET Surface Area (m^2/gcat)	Average Pore Size (Å)
Rh/γ-Al_2O_3	100	92.7
LZ	10.6	182
LRZ	9.6	210
LSRZ	11.5	148

3.4 Temperature Programmed Reduction (TPR)

TPR profiles for the four catalysts are shown in **Figure 3.2**. The reduction of Rh/γ-Al_2O_3 shows two peaks: a low temperature peak at 136°C and another at slightly higher temperature at 260°C. These can be attributed to the reduction of two different phases of rhodium oxide (RhO_x) [76-79]. However, the reduction temperatures for these peaks may vary from literature values due to the extent of interaction between the rhodium and alumina support [76, 78]. Reduction of the LZ material exhibits a single, broad reduction peak at 527°C. LRZ and LSRZ show high temperature peaks similar to

the LZ, at 549°C and 540°C respectively. The peak is shifted to a slightly higher temperature probably as a result of the substitution of rhodium and strontium.

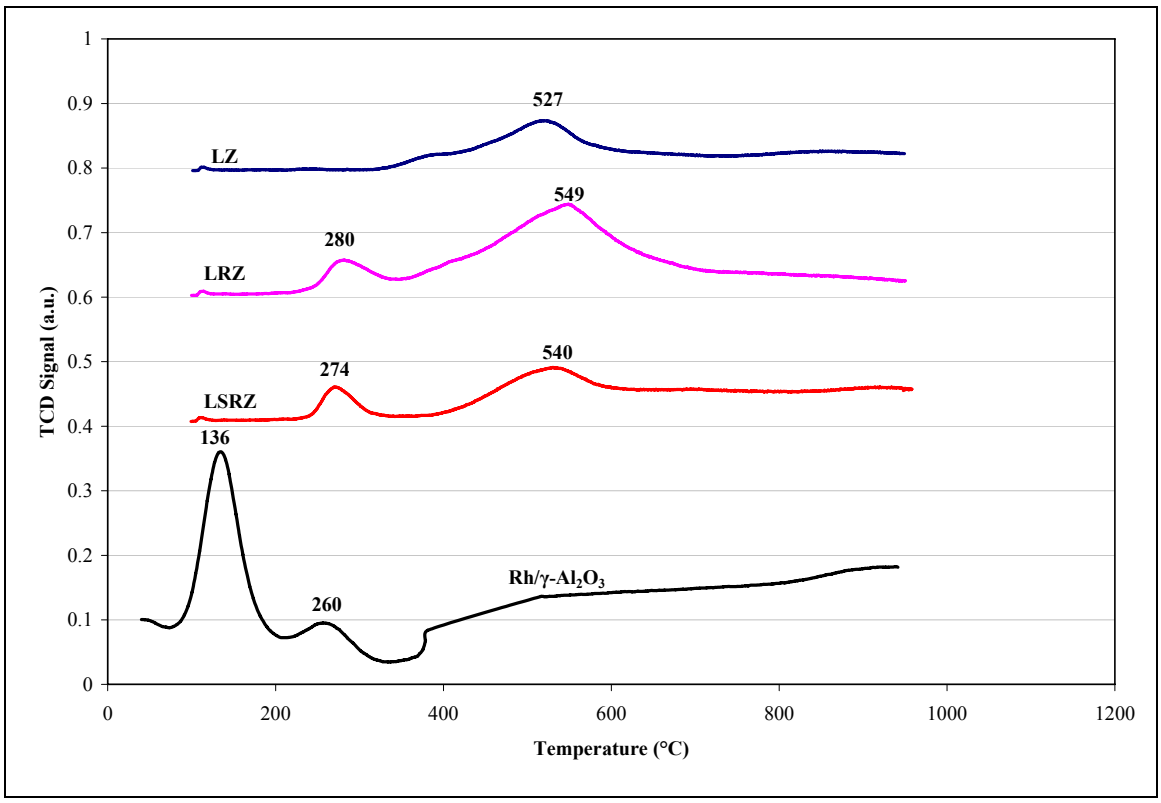

Figure 3.2. TPR results illustrating the change in reduction properties of LZ after the addition of Rh only, or Rh and Sr and compared to Rh/γ-Al_2O_3.

After Rh substitution a distinct, low temperature peak (280°C for LRZ and 274°C for LSRZ) occurs. This peak appears to be qualitatively similar to the secondary oxidation state seen on the Rh/γ-Al_2O_3 (260°C), only shifted to a higher temperature due to the interaction with surrounding elements in the pyrochlore structure. This is an indication that even though the metal is substituted throughout the structure, some metal atoms are accessible at the surface and can be reduced. The peaks are likely the result of

the reduction of a small amount of partially coordinated surface Rh atoms to their metallic state.

3.5 Metal Dispersion

Table 3.3 presents the amount of accessible rhodium metal on each catalyst. The pyrochlores show metal dispersion approximately an order of magnitude smaller than the Rh/γ-Al_2O_3. Low dispersion values for the LRZ and LSRZ initially suggest that large Rh metal clusters may have formed on the surface. However, as there was no low temperature reduction peak for Rh in the pyrochlores, compared to the reduction peak at 136°C for the Rh/γ-Al_2O_3, indicates that most of the metal is contained within the structure.

Table 3.3 Rhodium metal dispersion.

Catalyst	% Dispersion
0.51 wt % in Rh/γ-Al_2O_3	72.6
0.5 wt % in LRZ	4.0
0.6 wt % in LSRZ	9.9

3.6 Scanning Electron Microscopy and Electron Dispersive X-ray Analysis

The SEM images, shown in **Figure 3.3 and Figure 3.4**, depict the surface morphology of the LSRZ pyrochlore, which is the most active catalyst. As indicated by the low surface area from the BET analysis, the catalyst shows large pores in Figure 3.3, with pore diameters as large as 50μm. These large pores are beneficial for the reforming of diesel, because they facilitate the diffusion of the larger hydrocarbon molecules into the catalyst particle where they can be reacted and converted to synthesis gas.

SEM images were taken for the other three catalysts and are displayed in **Appendix A**. These results confirm that the LZ and LRZ also consist of large pores, with some shown to begreater than 25μm, while the alumina support has a porous surface with very small pore sizes << 5 μm. Rh clusters were too small to be observed by the SEM.

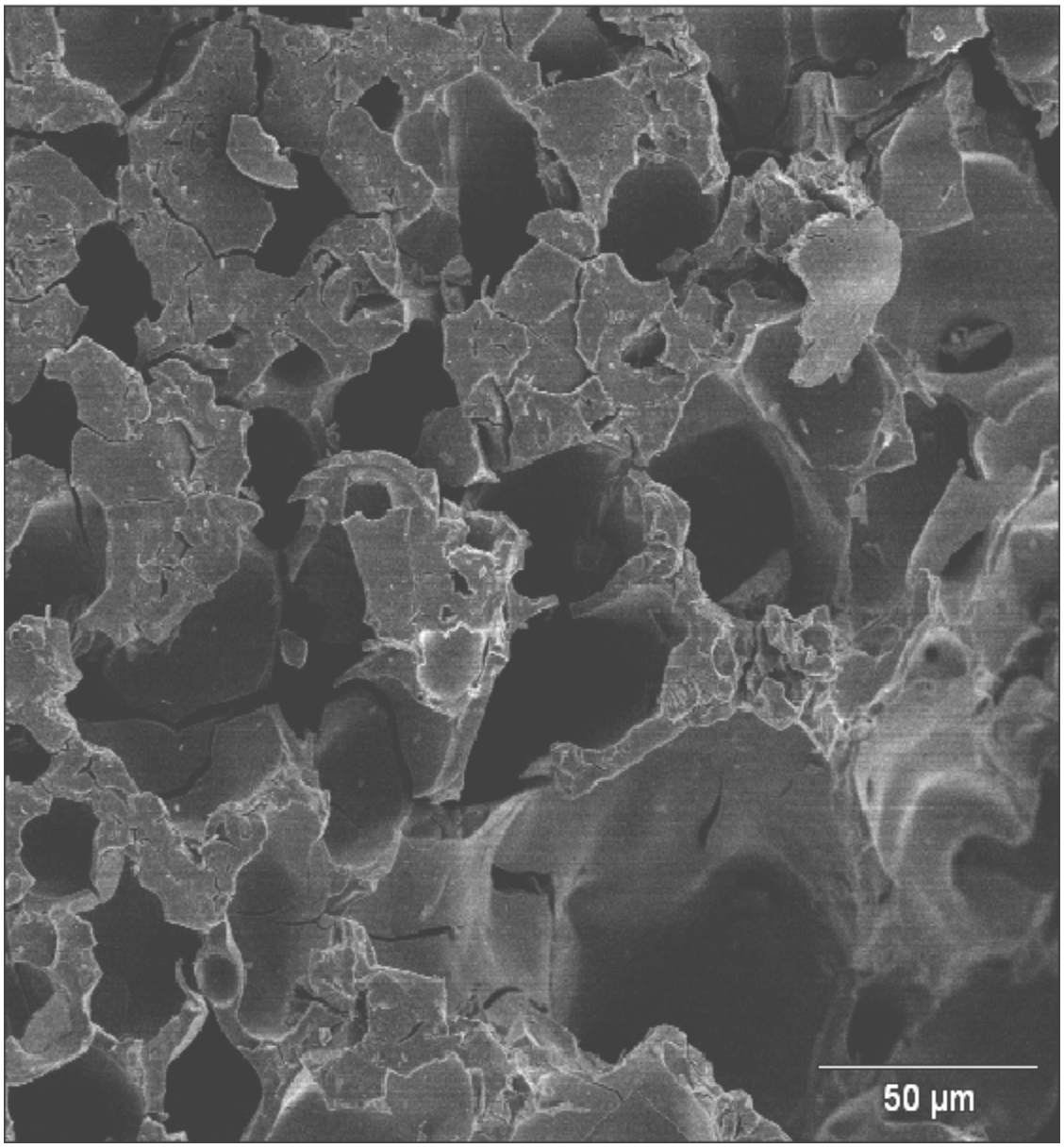

Figure 3.3. SEM image of LSRZ pyrochlore at 500x magnification and 10kV accelerating voltage.

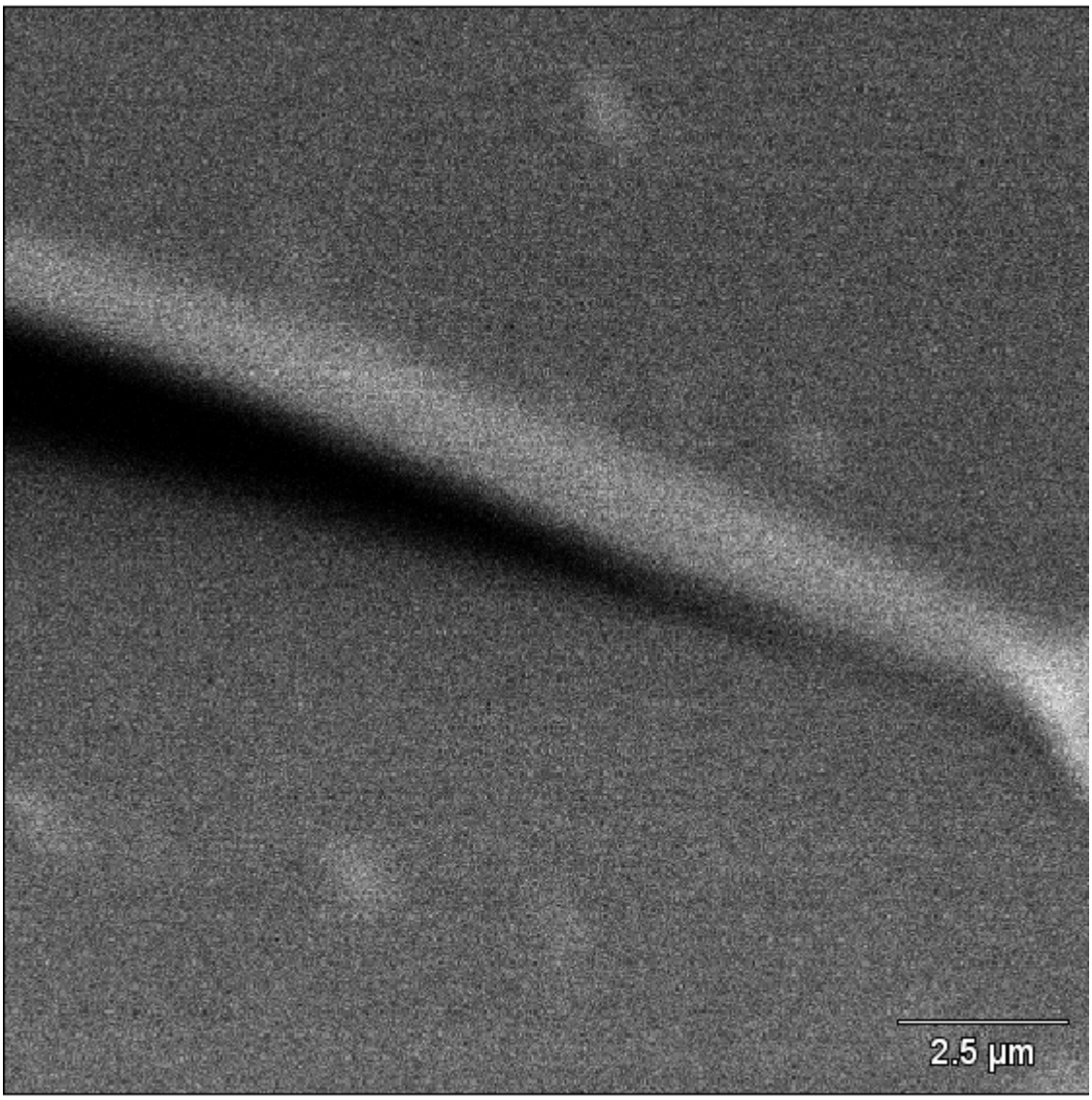

Figure 3.4. SEM image of LSRZ pyrochlore at 7500x magnification and 10kV accelerating voltage.

After imaging, the surface of two different LSRZ catalyst particles were analyzed using the EDX to determine the surface elemental composition. The results of the microanalysis are shown in **Figure 3.4 a and b**. After comparing the two figures, both show similar detection profiles, with roughly the same intensity. This verifies the Pechini method is capable of producing a material with a uniform composition. Also, the n-line

for Rh, at 2.7 kV, is barely visible in contrast to the background noise, which shows it is present but in a less detectible concentration compared to the other elements.

(a)

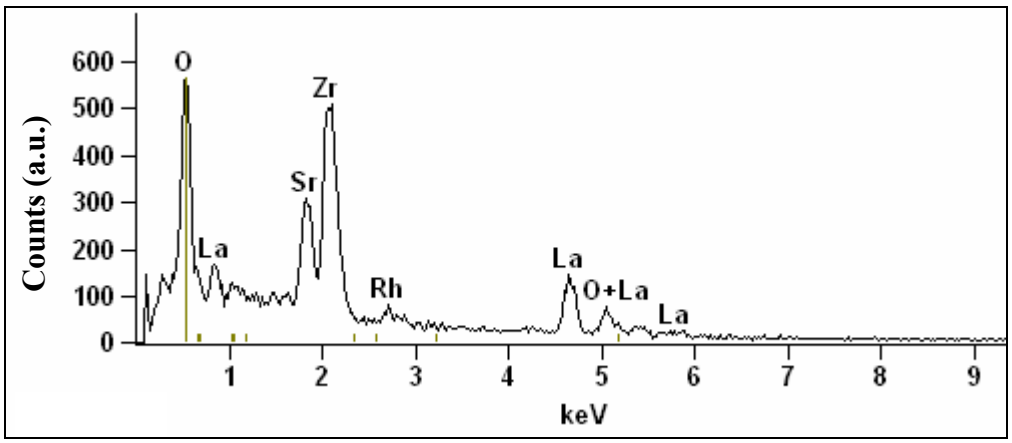

(b)

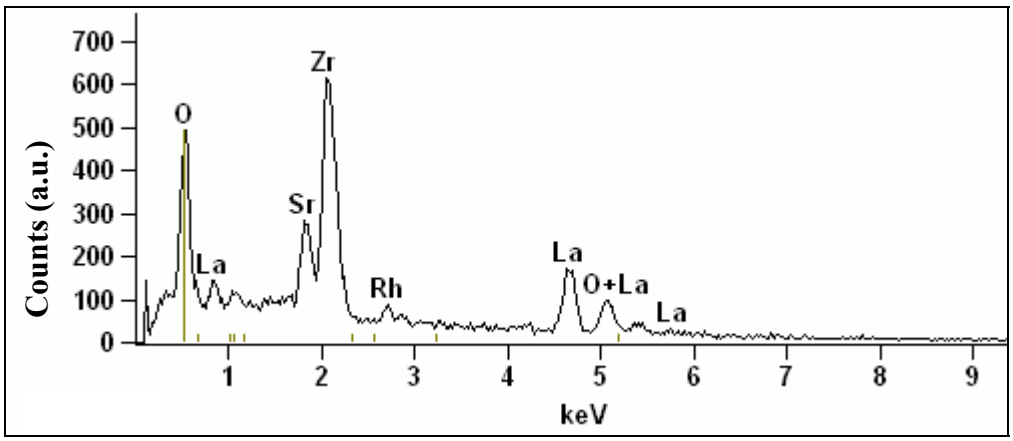

Figure 3.4 (a) and (b). EDX microanalysis results on two different LSRZ particles.

3.7 Mass Transfer Effects/Regimes

3.7.1 External Mass Transfer Limitations

An experiment was conducted on the Rh/γ-Al_2O_3 catalyst based on the correlation shown below to verify whether external mass transport limitations exist at the WHSV (50,000 scc g_{cat}^{-1} h^{-1}) defined for the CPOX experiment in Section 2.3.5. The results from the flow experiments shown in **Table 3.4** demonstrate that at high linear velocities the catalyst is not significantly limited by external transport effects. This is because, as the catalyst weight and corresponding linear fluid velocity are increased, the boundary layer between the bulk gas and catalyst surface is reduced. Conversion values increase at linear velocities above 630 cm/min because diffusion resistances through the boundary layer decrease.

$$\overline{k_c} \propto \frac{(D_{AB})^{2/3} u^{1/2} \rho^{1/6}}{(R_P)^{1/2} (\overline{\mu})^{1/6}}$$

Table 3.4 Conversion measurements for external mass transport limitations.

Catalyst Weight (g)	Conversion (%)	Linear Velocity (cm/min)	WHSV (scc g_{cat}^{-1} h^{-1})
0.28	92.6	463.0	50,000
0.38	99.2	630.0	50,000
0.48	100	798.0	50,000
0.58	100	964.0	50,000

3.7.2 Internal Mass Transfer Limitations

Internal transport resistances were estimated by calculating particle radius Rp, reaction rate constant k, and effective diffusivity D^e_{TA} values for the Thiele Modulus. In

calculating these values assumptions were made to assume worst case scenario for intraparticle mass transport limitations:

- Assume Knudsen diffusivity only, as catalyst pore sizes are small enough wall collisions dominate. In determining Knudsen diffusion coefficient, $D_{KTD} = (9.7x10^3) \bullet R_{pore} \bullet \left(\frac{T}{M_{TD}} \right)^{1/2}$ [71], the pore radius for LRZ was used (**Table 3.2**), so the calculation would result in the highest diffusion coefficient.
- No rate expression was available for POX, so a power law rate expression $r_{HC} = k_0 e^{\frac{-E_A}{RT}} C_{HC}^{a} C_{H_2O}^{b} C_{O_2}^{c}$ for diesel ATR was assumed [17], with b = 0 for POX.
- The kinetic parameters k_0, E_a, a, and c are intrinsic to reforming metal used. However, no parameters are reported for Rh/γ-Al_2O_3, only Pt/γ-Al_2O_3, Pd/γ-Al_2O_3, and Ru/γ-Al_2O_3. Thus, the kinetic parameters for Pd were used because it has the highest pre-exponential factor which would result in the highest reaction rate.
- The reaction rate was set to a pseudo first order rate expression to obtain a rate constant for the Thiele Modulus: $r_{HC} = k' C_{HC}$, then $\phi = R_p \sqrt{\frac{k'}{D_{TTD}^e}}$.
- 60-100 mesh particle size was used during experiment. This corresponds to 0.00745-0.0125 cm range of R_p. The smallest particle size, 100 mesh (0.00745 cm R_p), was assumed because if limitations were present at lowest R_p, they would also exist in largest size as well.
- 0.95 is the value for Thiele Modulus where transport limitations start.

After these assumptions, the parameters for the Thiele Modulus were calculated to be R_p= 0.00745cm; D^e_{TTD} 0.0031cm^2/s; k' = 0.13s^{-1}. These values gave a Thiele Modulus of roughly 0.047 which is much less than the 0.95 value where internal transport limitations start. Therefore, with the assumptions made, there are no internal transport resistances occurring in the reactor system.

Chapter 4. Results and Discussion: Activity Screening: CPOX of TD Only

Paraffins are the most reactive compounds in logistic fuel mixtures and they make-up a large portion of typical fuels [35], roughly 40 wt-%. Therefore the initial CPOX activity screening was evaluated using n-tetradecane (TD) as a model paraffin compound. This chapter compares the synthesis gas yields and selectivity of each catalyst to those of equilibrium and a blank reactor. In addition, carbon formation will be assessed by analyzing TPO profiles and amount of carbon deposited.

The results show that each of the Rh substituted pyrochlores has activity and selectivity comparable to the supported Rh/γ-Al_2O_3, and each Rh catalyst produces synthesis gas yields comparable to equilibrium levels. The unsubstituted pyrochlore has the lowest activity of all catalysts tested. Although synthesis gas yields varied for each catalyst, conversion of n-tetradecane was complete for each catalyst. The carbon formed over each catalyst is qualitatively similar, and the Sr and Rh substituted pyrochlore showed the lowest amount of carbon formed.

4.1 Reforming Results: CPOX of TD Only

4.1.1 Thermodynamic Equilibrium

The thermodynamic equilibrium product values, including yields of H_2, CO, CO_2, CH_4, olefins and overall conversion, for the CPOX of TD into a synthesis gas mixture are shown in **Table 4.1**. Equilibrium values were determined by a Gibbs free energy minimization calculation using HSC chemistry software [45]. The calculations were made assuming a mixture of 2 mol % TD, 18 mol % O_2, and 80 mol % N_2 (O/C= 1.2), P=2 atm and 900°C. The results show that high H_2 and CO yields are favorable at a ratio

of H_2/CO <1, with no carbon formation. Equilibrium values also serve as a reference to judge the activity of the catalysts.

Table 4.1 Equilibrium product yield, conversion, and carbon formation for the CPOX of TD at O/C= 1.2, P= 0.23 MPa and 900°C. Values were calculated by a Gibb's free energy minimization technique using HSC Chemistry Thermodynamic software.

H_2 Yield (%)	89.5
CO Yield (%)	91.6
CO_2 Yield (%)	8.5
CH_4 Yield (%)	0.1
H_2O Yield (%)	9.6
C_2-C_6 Yield (%)	0.0
Conversion (%)	100
Elemental Carbon	0.0

4.1.2 Blank Reactor (Quartz Sand)

The CPOX of TD over inert quartz sand was performed to establish a baseline for hydrocarbon conversion and product yields in the absence of a catalyst in the reactor system. All yields presented from here on (i.e. H_2, CH_4 or C_6H_6) have been determined to have standard error of ± 9% for each experiment. The dry gas yields as well as hydrocarbon conversion for the quartz at 900°C, 2.3 atm, and WHSV of 50,000scc/$g_{catalyst}$/h are shown in **Figure 4.1**. These yields are similar to a blank that was run previously in this same system, under the same conditions, only at 850°C [80]. It can be seen that the hydrocarbon conversion was very high in the blank reactor. However, a significant amount of the TD is converted to olefins (~24%) and lower hydrocarbons such as methane (~10%). The distribution of olefins formed is shown in **Table 4.2**. The product selectivity of the C_2+ olefins formed are mainly ethylene and

propylene, which is consistent with gas-phase reaction products seen in other results [51, 81]. Although these hydrocarbons contain H_2, their formation cannot account for the difference in H_2 yields compared to equilibrium values shown in **Table 4.1**. A mass balance over O_2 and H_2 atoms shows an H/O ratio of roughly 2.4 over the 5 h experiment, suggesting that water formation is occurring. Coupling this data with the dry gas profile in **Figure 4.1** suggests that the net overall reaction can be described as:

$$C_nH_m + O_2 \rightarrow CO + H_2O + CO_2 + H_2$$

which implicitly involves water-gas shift and reforming reactions.

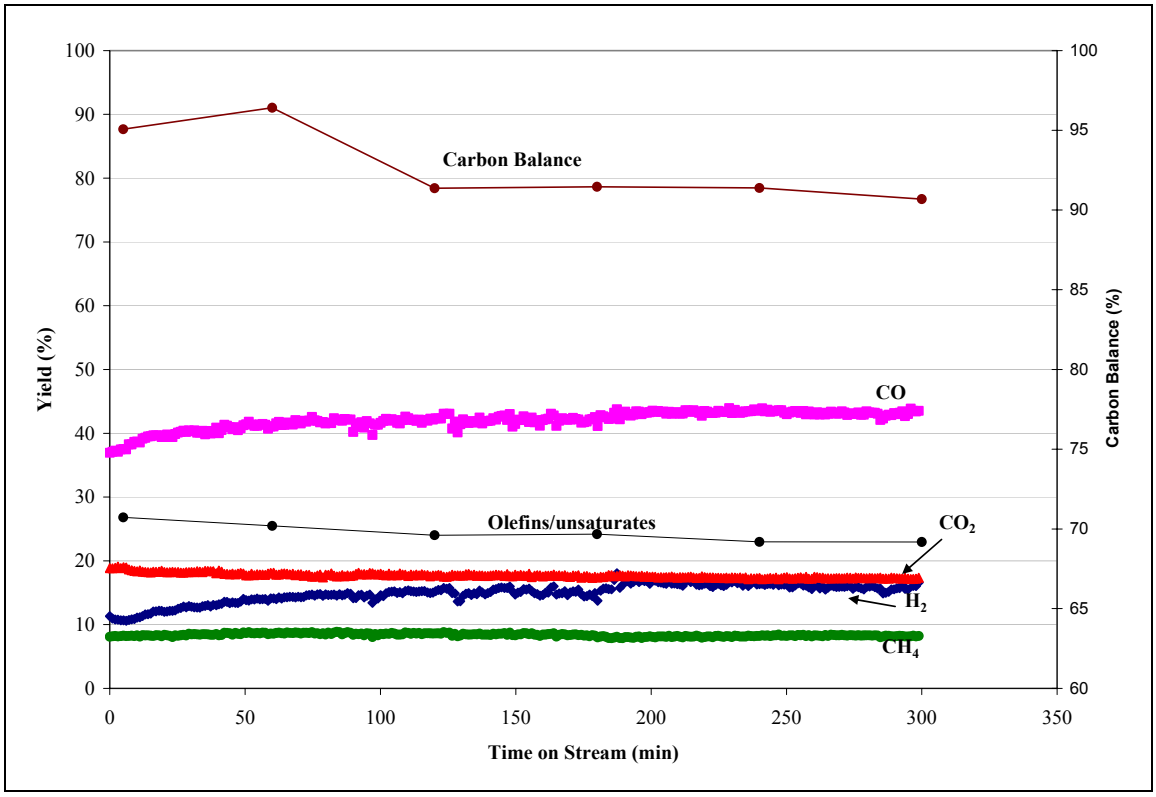

Figure 4.1 Synthesis gas selectivity and carbon balance of blank reactor (quartz sand) reforming TD for 5 hours at O/C=1.2, 0.23 MPa, 900°C and 50,000 scc/$g_{catalyst}$/h. H_2 (♦), CO (■), CO_2 (▲), CH_4 (●).

Table 4.2 C_2, C_3, C_4 and benzene yields after CPOX of TD for 5 hours over quartz sand at O/C=1.2, 0.23 MPa, 900°C and 50,000 scc/$g_{catalyst}$/h.

Compound	Yield (%)	Measurement Error (%)
Ethane	0.70	±9
Ethylene	16.30	±9
Propylene	17.0	±9
1,3-Butadiene	1.0	±9
Benzene	3.90	±9

4.1.3 Rh/γ-Al_2O_3

Synthesis gas and higher hydrocarbon yields that result from the CPOX of TD over Rh/γ-Al_2O_3 are presented in **Figure 4.2** and **Table 4.3** respectively. The results demonstrate that rhodium metal is highly active for the CPOX of higher hydrocarbons. All carbon was accounted for, and the H_2 and CO yields produced were close to equilibrium levels while olefin and benzene yields remained low. Also, the catalytic activity was stable, at least over the time of the experiment (5 h). This activity is consistent with the results of Schmidt et al. [28, 43, 44, 48, 82], who have reported high H_2 and CO selectivities (>70%) in the CPOX (O/C=1.2) of model paraffin compounds n-decane (C_{10}) [28, 44] and n-hexadecane (C_{16}) [28, 82] over a Rh/γ-alumina coated onto an α-Al_2O_3 foam monolith.

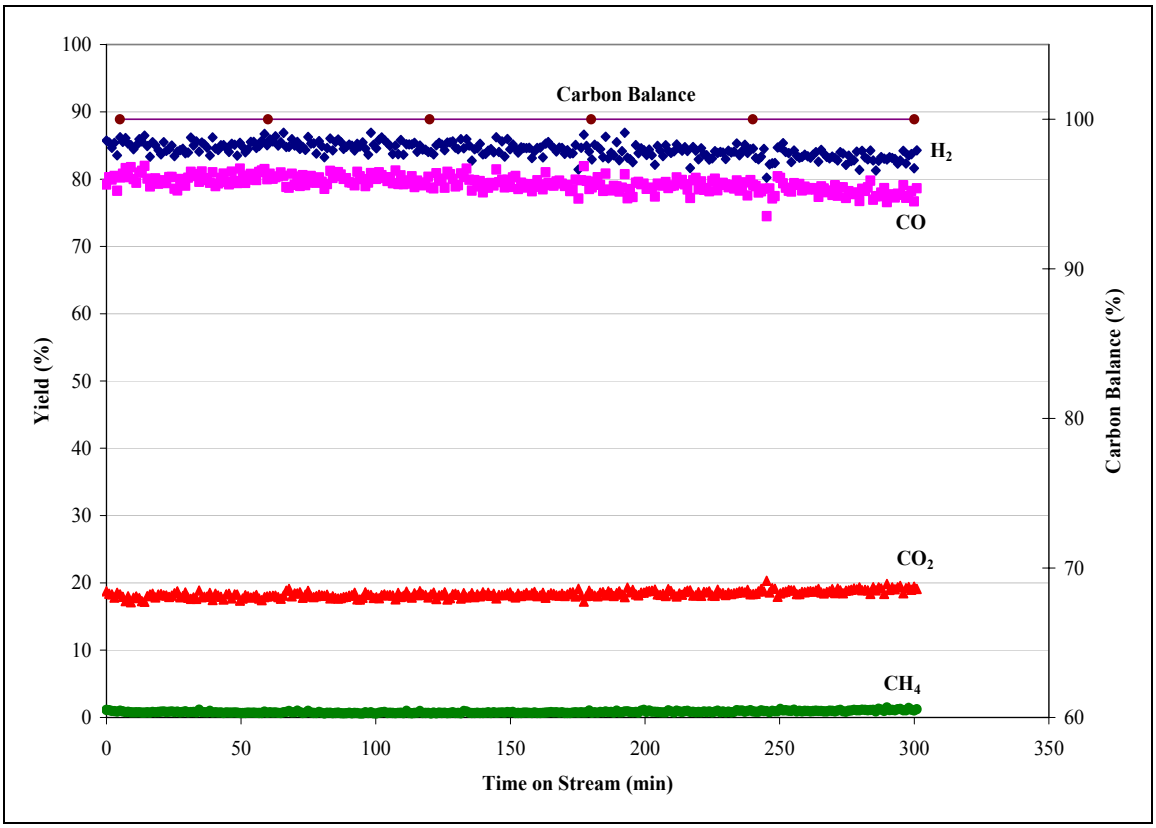

Figure 4.2 Synthesis gas yield for Rh/γ-Al_2O_3 reforming TD for 5 hours at an O/C= 1.2, 0.23 MPa, 900°C and 50,000 scc/$g_{catalyst}$/h. H_2 (♦), CO (■), CO_2 (▲), CH_4 (●).

Table 4.3 C_2, C_3, C_4, and benzene yields as well as H_2 and O_2 mole balances after 5 hours of reforming TD at O/C= 1.2, 900°C and 50,000scc/$g_{catalyst}$/h.

	Equilibrium[a]	Quartz Sand (Blank)	Rh/γ-Al_2O_3
Ethane Yield (%)	0.0	0.70	0.10
Ethylene Yield (%)	0.0	16.30	0.10
Propylene Yield (%)	0.0	17.0	n.d.[b]
1,3-Butadiene Yield (%)	0.0	1.0	n.d.
Benzene Yield (%)	0.0	3.90	0.06

a- Equilibrium calculations were made using a Gibb's minimization technique in HSC Chemistry Thermodynamic Software. Calculations were made assuming a mixture of 2 mol % TD, 18 mol % O_2, and 80 mol % N_2 (O/C= 1.2), P=2 atm and 900°C.

b- n.d.- Not Detected

4.1.4 Lanthanum Zirconate (LZ)

Yields of synthesis gas and higher hydrocarbons produced after the CPOX of TD over LZ pyrochlore are presented **Figure 4.3** and **Table 4.3**, respectively. Surprisingly, LZ is active in a CPOX reforming environment; however the yields are not as stable, as there is a clear decrease (5%) in H_2 and CO yields over 5 h experiment. In comparison to Rh/γ-Al_2O_3, LZ is less selective towards synthesis gas, which is to be expected in the absence of a noble metal catalyst. The carbon balance shows all carbon is accounted for but the pyrochlore produces a noticeably larger quantity of methane, as well as C_2-C_3 hydrocarbons than Rh/γ-Al_2O_3. It is the formation of these products that results in lower H_2 and CO yields and a synthesis gas ratio (H_2/CO) ≤ 1. A mass balance of hydrogen-containing species in the product stream of LZ shows the equivalent yield of H_2 contained in these hydrocarbons to be between 10-11% over the 5 h of the experiment. This indicates that the lower H_2 formation between LZ and Rh can be accounted for by the increase in formation of CH_4, and C_2-C_3 hydrocarbons (mainly ethylene).

Table 4.4 C_2, C_3, C_4, and benzene yields as well as H_2 and O_2 mole balances after 5 hours of reforming TD at O/C= 1.2, 900°C and 50,000scc/$g_{catalyst}$/h.

	Equilibrium[a]	Quartz Sand (Blank)	Rh/γ-Al_2O_3	LZ
Ethane Yield (%)	0.0	0.70	0.10	0.90
Ethylene Yield (%)	0.0	16.30	0.10	1.90
Propylene Yield (%)	0.0	17.0	n.d.[b]	0.30
1,3-Butadiene Yield (%)	0.0	1.0	n.d.	n.d.
Benzene Yield (%)	0.0	3.90	0.06	0.40

a- Equilibrium calculations were made using a Gibb's minimization technique in HSC Chemistry Thermodynamic Software. Calculations were made assuming a mixture of 2 mol % TD, 18 mol % O_2, and 80 mol % N_2 (O/C= 1.2), P=2 atm and 900°C.

b- n.d.- Not detected, LZ= $La_2Zr_2O_7$

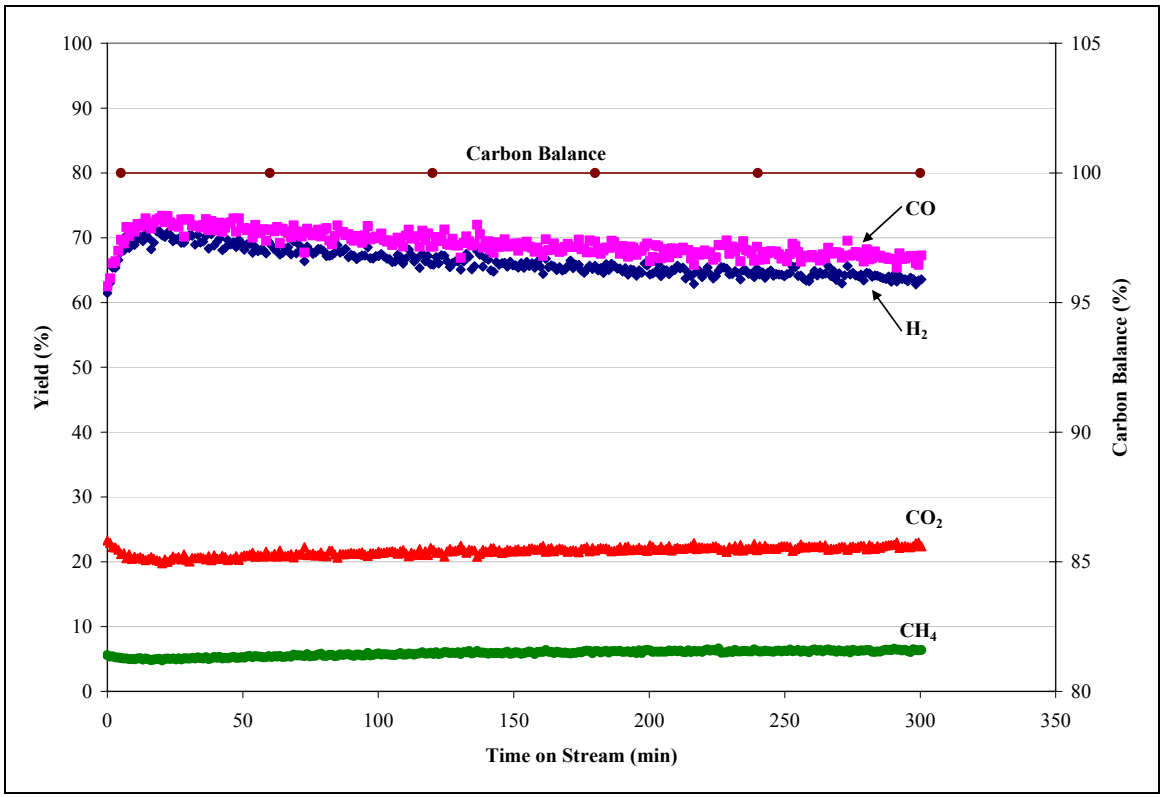

Figure 4.3 Synthesis gas yield for LZ reforming TD for 5 hours at an O/C=1.2, 0.23 MPa, 900°C and 50,000 scc/$g_{catalyst}$/h. H_2 (♦), CO (■), CO_2 (▲), CH_4 (●).

4.1.5 LRZ

The exchange of rhodium for B-site zirconium gives LRZ comparable synthesis gas and olefin yields to Rh/γ-Al_2O_3 for the CPOX of TD (shown in **Figure 4.4** and **Table 4.3**). This indicates that the available rhodium retains its high activity and selectivity after it is substituted in this structure. The activity likely results from the rhodium metal atoms at the surface that are only partially coordinated with oxygen molecules, rather than fully coordinated within the structure. This is consistent with TPR results for LRZ presented earlier, in **Figure 3.2**, where a low temperature reduction peak indicates that a small amount of Rh is accessible at the surface and is reducible. In this case, the partial coordination of rhodium permits the metal to readily react with TD or other hydrocarbons

and oxygen at the surface. A similar behavior was reported by Liu et al. [57] for the ATR of surrogate diesel fuel mixture using a ruthenium substituted perovskite catalyst. They reported the most active sites for ATR activity were ruthenium atoms distributed at the B-site at the surface [57].

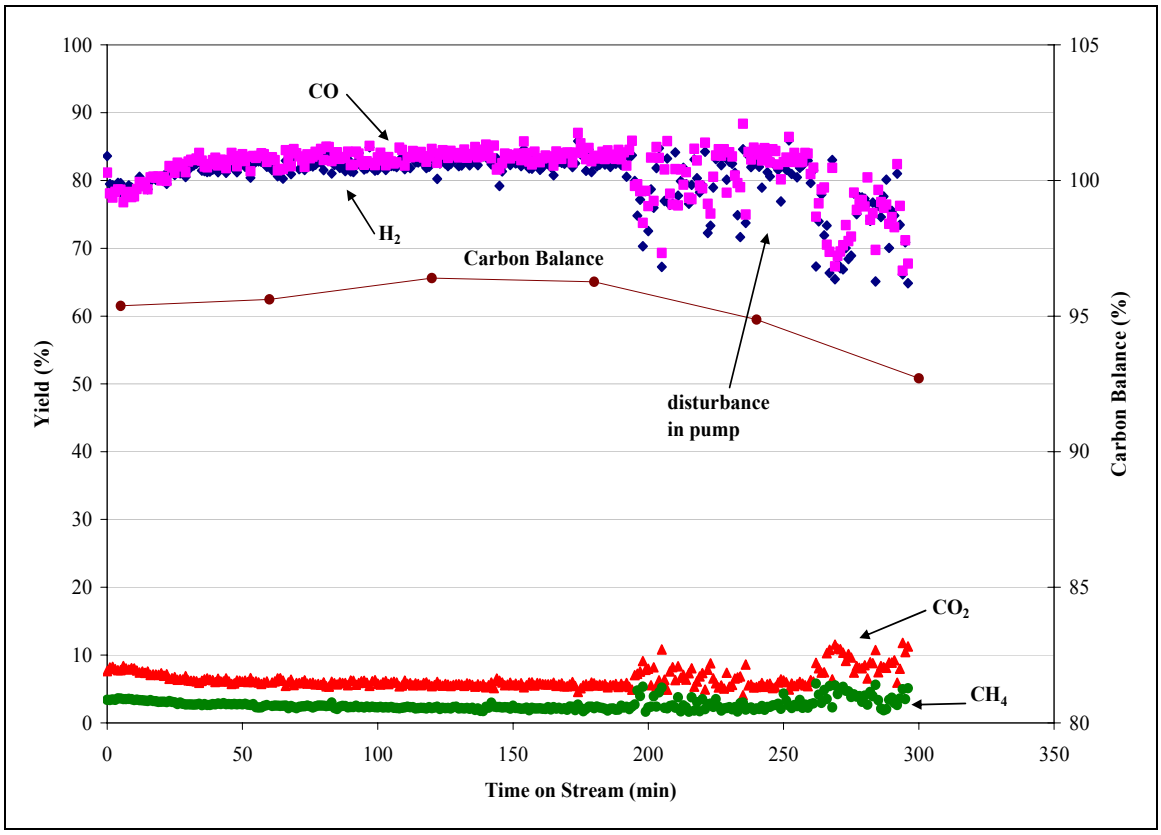

Figure 4.4 Synthesis gas yield for LRZ reforming TD for 5 hours at an O/C=1.2, 0.23 MPa, 900°C and 50,000 scc/$g_{catalyst}$/h. H_2 (♦), CO (■), CO_2 (▲), CH_4 (●).

Table 4.5 C_2, C_3, C_4, and benzene yields for Rh/γ-Al_2O_3, LZ and LRZ after CPOX of TD for 5 hours at O/C= 1.2, 0.23 MPa, 900°C and 50,000scc/$g_{catalyst}$/h.

	Equilibrium[b]	Quartz Sand (Blank)	Rh/γ-Al_2O_3	LZ	LRZ
Ethane Yield (%)	0.0	0.70	0.10	0.90	0.10
Ethylene Yield (%)	0.0	16.30	0.10	1.90	0.40
Propylene Yield (%)	0.0	17.0	n.d.[a]	0.30	n.d.
1,3-Butadiene Yield (%)	0.0	1.0	n.d.	n.d.	n.d.
Benzene Yield (%)	0.0	3.90	0.06	0.40	0.50
H_2 balance (mol/s)	0.0	2.1E-3	9.1E-4	1.0E-3	8.8E-4
O_2 balance (mol/s)	0.0	1.0E-3	n.d.	6.1E-5	5.7E-4

a- Equilibrium calculations were made using a Gibb's minimization technique in HSC Chemistry Thermodynamic Software. Calculations were made assuming a mixture of 2 mol % TD, 18 mol % O_2, and 80 mol % N_2 (O/C= 1.2), P=2 atm and 900°C.

b- n.d.- Not detected, LZ= $La_2Zr_2O_7$, LRZ= $La_2Rh_{0.11}Zr_{1.89}O_{6.95}$

4.1.6 LSRZ

Figure 4.5 and **Table 4.6** show the synthesis gas and C_2-C_4 and benzene yields for the LSRZ pyrochlore. The results indicate that doping the catalyst with strontium and rhodium together results in a catalyst that produces a synthesis gas mixture roughly equal to equilibrium values. During CPOX, roughly ≥ 94% of the carbon is accounted for, which is roughly within the range of error in the carbon balance (±5%), and no olefins are detected over the time of the experiment. The higher activity may be due to the larger amount of partially coordinated rhodium on the surface, as was seen by the results of the chemisorption experiments in Chapter 3. Lattice oxygen mobility that results from the substitution of Sr^{2+} for La^{3+} may also further enhance CPOX activity [57, 61]. The structural defects created by the substitution of strontium may eliminate olefin formation because mobilized lattice oxygen can react with the strongly adsorbed carbon containing species to form CO.

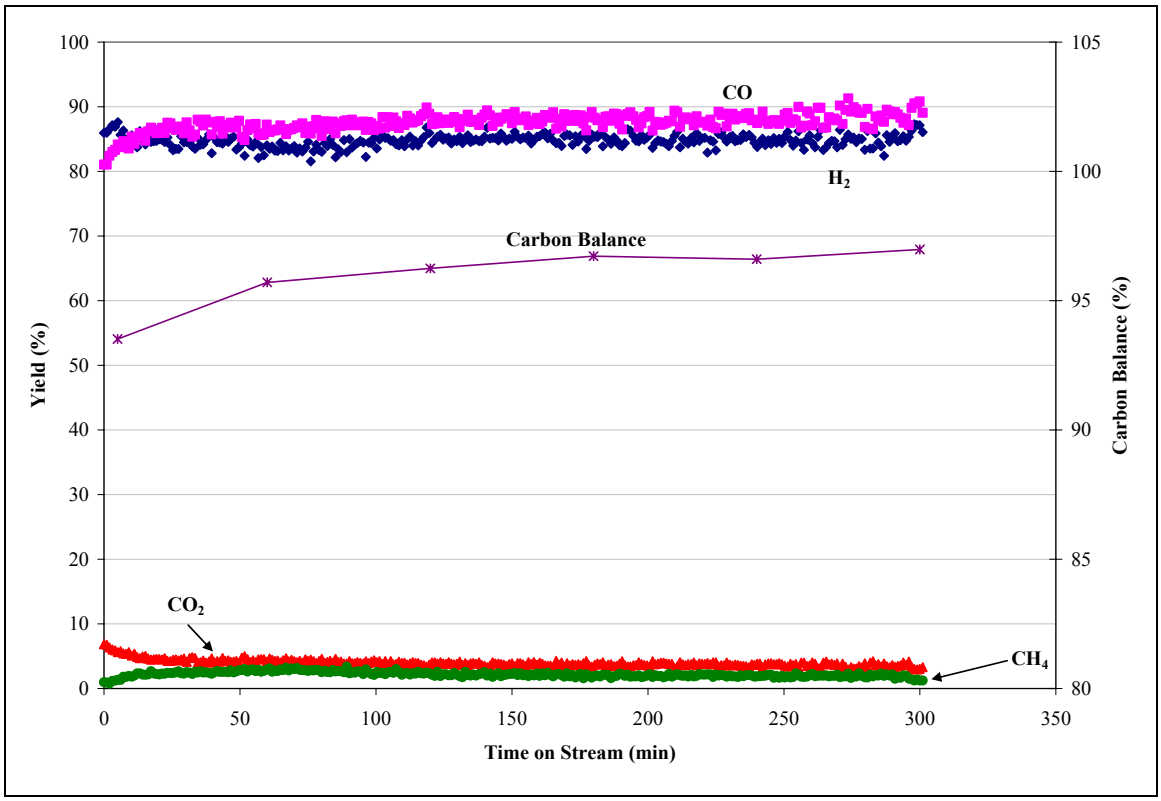

Figure 4.5 Synthesis gas yield for LSRZ reforming TD for 5 hours at an O/C=1.2, 0.23 MPa, 900°C and 50,000 scc/$g_{catalyst}$/h. H_2 (♦), CO (■), CO_2 (▲), CH_4 (●).

Table 4.6 C_2, C_3, C_4, and benzene yields for Rh/γ-Al_2O_3 and pyrochlores after 5 hours of reforming TD at O/C= 1.2, 0.23MPa, 900°C and 50,000scc/$g_{catalyst}$/h.

	Equil.[a]	Quartz Sand (Blank)	Rh/γ-Al_2O_3	LZ	LRZ	LSRZ
Ethane Yield (%)	0.0	0.70	0.10	0.90	0.10	n.d.
Ethylene Yield (%)	0.0	16.30	0.10	1.90	0.40	n.d.
Propylene Yield (%)	0.0	17.0	n.d.[b]	0.30	n.d.	n.d.
1,3-Butadiene Yield (%)	0.0	1.0	n.d.	n.d.	n.d.	n.d.
Benzene Yield (%)	0.0	3.90	0.06	0.40	0.50	n.d.

a- Equilibrium calculations were made using a Gibb's minimization technique in HSC Chemistry Thermodynamic Software. Calculations were made assuming a mixture of 2 mol % TD, 18 mol % O_2, and 80 mol % N_2 (O/C= 1.2), P=2 atm and 900°C.

b- n.d.- Not detected, LZ= $La_2Zr_2O_7$, LRZ= $La_2Rh_{0.11}Zr_{1.89}O_{6.95}$, LSRZ= $La_{1.5}Sr_{0.5}Rh_{0.10}Zr_{1.90}O_{6.7}$.

4.2 Carbon Formed after CPOX of TD

The CPOX of TD is inevitably accompanied by the formation of carbon. This becomes a major concern because the accumulation of carbon will deactivate the catalyst and decrease the production of synthesis gas. In order to avoid this problem, it becomes important to understand the physical properties of the adsorbed carbon.

Although paraffins are the most reactive compounds in diesel fuel, at elevated temperatures the long chains have a tendency to dehydrogenate and aromatize on the catalyst surface to form coke or graphitic carbon. Guisnet et al. [83] reported that for hydrocarbon reforming reactions above 350°C, the adsorbed carbon species generally consist of polyaromatic compounds, which are also known as coke. Therefore, as the CPOX of TD takes place at 900°C, or higher, it is probable that the carbon formed on each catalyst contains a variation of this structure. The carbon/coke content for each catalyst was quantified by a TPO, and the results are shown in **Figure 4.6** and **Table 4.7**.

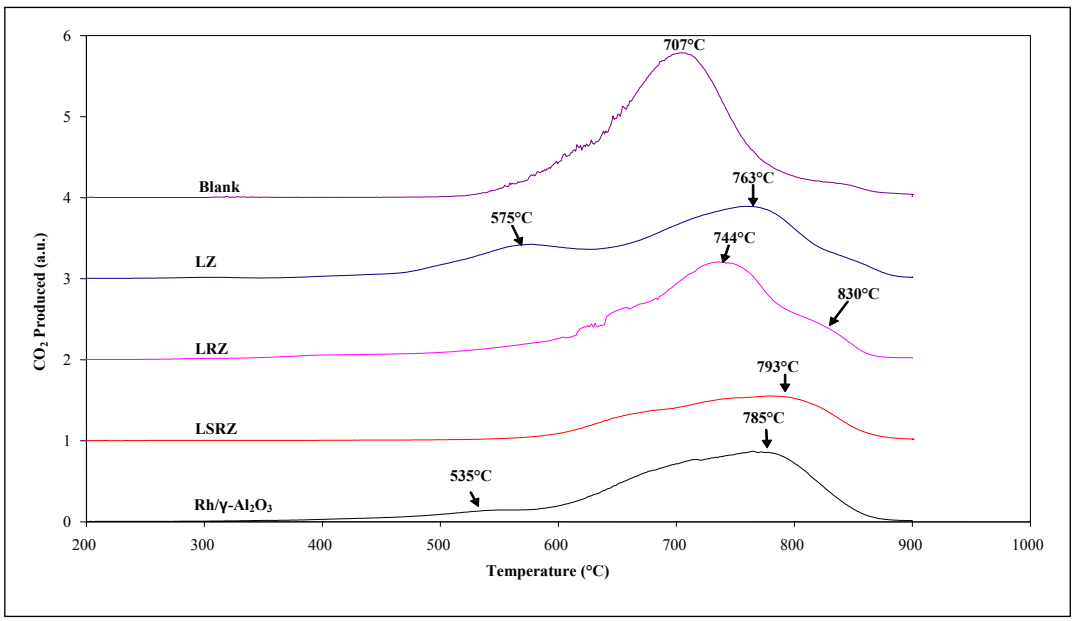

Figure 4.6 TPO profiles after CPOX of n-TD only for blank reactor, LZ, LRZ, LSRZ and Rh/γ-Al_2O_3.

Table 4.7 Carbon deposited after CPOX of TD for 5 hours; 900°C, 50000 h^{-1}.

Catalyst	Carbon Accumulated ($g_{carbon}/g_{catalyst}$)
LZ	0.29
LRZ	0.32
LSRZ	0.17
Rh/γ-Al_2O_3	0.27
Blank	0.40

$g_{catalyst}$- carbon normalized to total amount of catalyst in reactor (480 mg).

4.2.1 Blank

The carbon deposited on the surface of the quartz sand is formed as a result of the thermal cracking of TD. Thermal decomposition of TD involves the dehydrogenation of the alkenes into olefins, then the subsequent breakage of C-C bonds into radicals and smaller hydrocarbons [38]. Either of these steps forms reactive products/intermediates that form carbon. These compounds then adsorb on the surface as ordered compounds and require high temperatures for burn-off.

4.2.2 Rh/γ-Al_2O_3

Two peaks arise during the TPO of Rh/γ-Al_2O_3: a small shoulder around 535°C then a larger peak at 785°C. These two peaks suggest that carbon has deposited onto different parts of the surface with different reactivities. Several studies have indicated that the low temperature peak can be attributed to the carbon deposited onto or near the metal, while the high temperature peak can be associated to the more refractory carbon on the support [40, 42, 84, 85]. Therefore, the low temperature shoulder, at 535°C, is probably the carbon deposited on or near the Rh metal surface. It is oxidized at a lower temperature because the metal catalyzes the oxidation of the carbon. The high temperature peak (observed ~ 785°C) is then a result of the carbon deposited on the

alumina support. This carbon is much more stable on the surface of the support, and thus is oxidized at a higher temperature because there is no metal to catalyze the burn-off.

4.2.3 LZ

The carbon formed on LZ material is qualitatively and quantitatively similar to the carbon that accumulated on the Rh/γ-Al_2O_3 catalyst. This suggests that there are two parts of the surface that adsorb carbon, and the reactivity of this carbon is similar to that which adsorbs onto the Rh/γ-Al_2O_3. The first peak/shoulder, at roughly 575°C, may be attributed to a more hydrogenated form of coke, which has been reported as the structure of carbon that adsorbs onto the metal of supported metal catalysts [84]. The high temperature peak may then be due to an unsaturated form of coke [84]. This type of coke takes the form of a dehydrogenated polynuclear aromatic structure, which has a slow oxidation rate and requires a higher temperature to burn off.

4.2.4 LRZ

Rhodium substitution does not reduce the amount of carbon that accumulates on the pyrochlore material, as the values in **Table 4.7** show that the amount of carbon on LZ and LRZ are relatively the same. However, no low temperature peak is observed for the LRZ that would correspond either to carbon deposited on rhodium metal (seen in the TPO for Rh/Al_2O_3) or reactive coke seen on LZ. The carbon that does accumulate is qualitatively similar to the high temperature carbon on LZ, but there is more of it.

4.2.5 LSRZ

The substitution of lower valence elements into the A-site of perovskite catalysts has been shown to create structural defects which lead to the movement of oxygen ions throughout the lattice [57, 60, 61, 86]. In the presence of a reforming metal, oxygen mobility has been linked to lower carbon formation [57, 60]. Erri et al. [60] reported the addition of ceria to the A-site of a $LaFe_{0.4}Ni_{0.6}O_3$ perovskite reduced the amount of carbon compared to the undoped version during the ATR of JP-8 fuel. In the present study, LSRZ has the lowest amount of carbon formed, compared to the other 3 catalysts. This suggests that strontium addition may create structural defects which enhance the oxygen mobility in the material. This in turn, reduces the amount of carbon that is able to form on the surface because carbon deposited on the surface reacts with mobilized oxygen from the lattice. The reactivity of the carbon deposited on LSRZ is qualitatively similar to LRZ, but this catalyst has less carbon (0.17 $g_{carbon}/g_{catalyst}$) than any other catalyst in **Table 4.7** and roughly half that of the non-strontium containing LRZ, (0.32 $g_{carbon}/g_{catalyst}$). Again, there is no metal peak at 535°C corresponding to carbon adsorbed on the rhodium, only a TPO peak resembling the high temperature coke on the LZ.

Chapter 5. Results and Discussion: Effects of Polynuclear Aromatics

In middle distillate fuels, polynuclear aromatics can be present in concentrations between 5-15 wt-% [35]. These compounds can deactivate metal catalysts because they are less reactive on the surface than the paraffinic compounds [17, 87]. This chapter will discuss the effects of the addition of 5 wt-% of the polyaromatic compound 1-methylnapthalene (MN) to n-tetradecatne (TD) on synthesis gas yield and carbon formation.

The results, discussed below, show that the substitution of Rh only and Sr and Rh into the pyrochlore lattice results in higher synthesis gas yields in the presence of MN when compared to LZ and Rh/γ-Al_2O_3. The resistance toward carbon formation also increases compared to LZ for both the LRZ and LSRZ; however when compared to Rh/γ-Al_2O_3 only, LSRZ has quantitatively less carbon.

5.1 Reforming Results: 5 wt-% MN

The CPOX of TD was run for 1 hour before the addition of MN. The synthesis gas yields produced during this time, **Table 5.1**, over rhodium catalysts Rh/γ-Al_2O_3, LRZ and LSRZ are comparable to the equilibrium levels of CPOX of TD only shown in Table 4.1. As seen in Chapter 4 Section 4.1.4, LZ had the lowest H_2 and CO yields because the transition metal active sites are less selective towards synthesis gas than the Rh. After 1 h, 5 wt% MN was added to the TD. While MN was present in the feed, all catalysts suffered activity loss; however, the effects on product yield and carbon formation were different for each catalyst.

Table 5.1 Synthesis gas yields for each catalyst during the CPOX of TD after 1 h time on stream at an O/C=1.2, 0.23 MPa, 900°C and 50,000 scc/$g_{catalyst}$/h.

	$Rh/\gamma\text{-}Al_2O_3$	LZ	LRZ	LSRZ
H_2 Yield (%)	85.0	62.0	89.0	91.0
CO Yield (%)	80.0	64.0	94.0	91.0

5.1.1 $Rh/\gamma\text{-}Al_2O_3$

5.1.1.1 Effect of MN on Synthesis Gas Yield

The effects of MN on the activity and conversion of $Rh/\gamma\text{-}Al_2O_3$ are shown in **Figures 5.1 and 5.2**. Although the carbon balance remains near 100%, the addition of MN results in a drastic change in product selectivity. Over the 2 hours MN is present, H_2 yield decreases continuously while CO decreases, but less rapidly. The decrease in synthesis gas yield is accompanied by a large increase in unsaturated hydrocarbons and ethane (Figure 5.2). This behavior has been reported previously for the CPOX of a 5 wt-% MN/TD mixture at 850°C over Pt and carbide catalysts [42, 80].

This behavior is likely a result of the deactivation of the $Rh/\gamma\text{-}Al_2O_3$ by the MN. Initially, it appears that the MN kinetically inhibits the CPOX reaction, since H_2 and CO yields are suppressed to similar levels. However, over the two hours, MN further deactivates the catalyst and the dry gas yield for the $Rh/\gamma\text{-}Al_2O_3$ catalyst (during the time MN is present) approaches yields of the blank reactor shown, in Figure 4.1. Deactivation occurs as a result of the different reactivities between TD versus MN over the $Rh/\gamma\text{-}Al_2O_3$ catalyst. Subramanian et al. performed a study to investigate the optimal O/C ratio needed to give the maximum synthesis gas yield for the CPOX of surrogate gasoline and diesel mixtures over a Rh coated monolith [43].

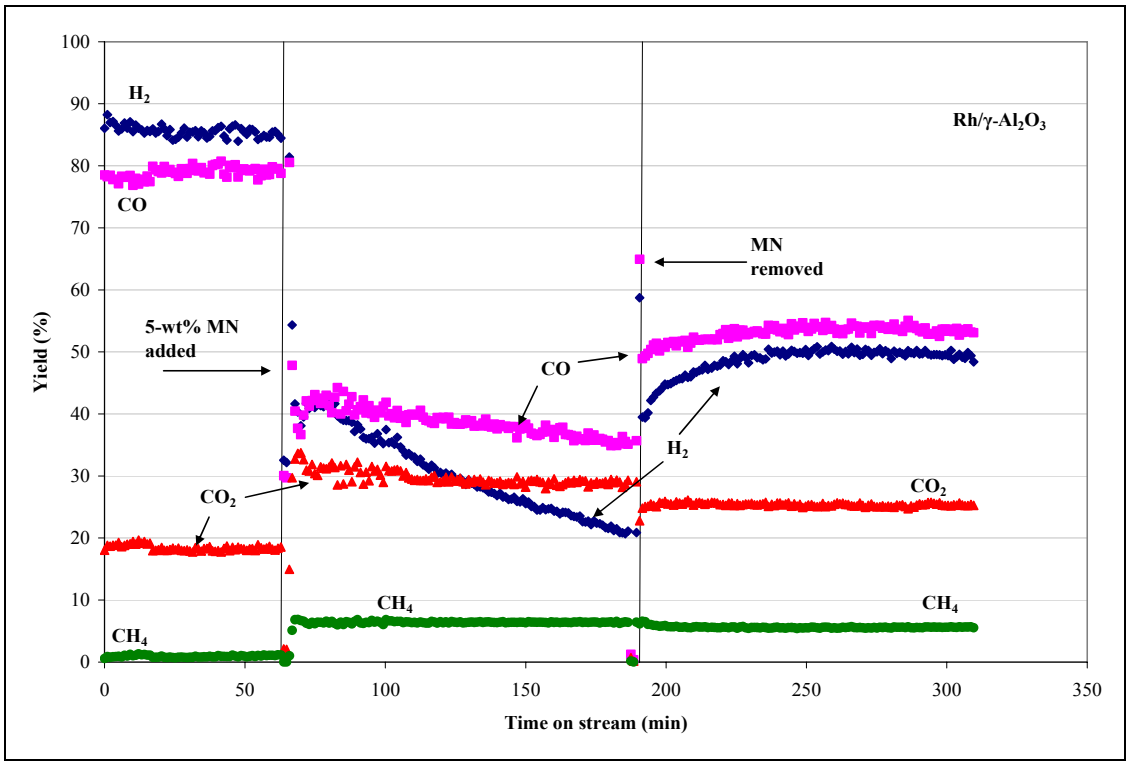

Figure 5.1 Step response plot for Rh/γ-Al_2O_3 after the addition of 5-wt% MN at an O/C=1.2, 0.23 MPa, 900°C and 50,000 scc/$g_{catalyst}$/h. H_2 (♦), CO (■), CO_2 (▲), CH_4 (●).

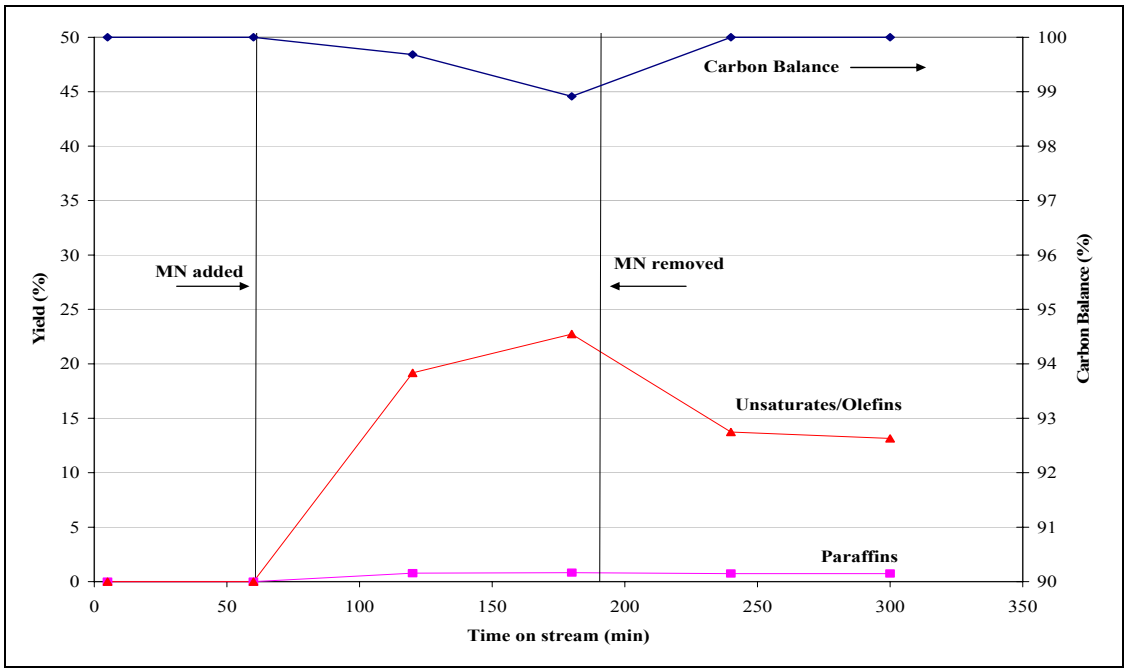

Figure 5.2 Paraffins, unsaturates yields and carbon balance for Rh/γ-Al_2O_3 during the 5-wt% MN experiment at an O/C=1.2, 0.23 MPa, 900°C and 50,000 scc/$g_{catalyst}$/h. Conversion (♦), Olefins (▲), Paraffins (■).

The study was conducted because gasoline and diesel fuel compositions are mixtures of different complex compounds with different reactivities. They concluded that at each O/C ratio, the fuel reactivities were not an average of the two fuels, but instead the most reactive fuel reacted with the O_2 first [43]. Unfortunately, for comparative purposes with the present study, they only demonstrated the conversion and selectivity at steady state for each O/C, not the continuous effects of the fuel mixtures on catalytic activity over time. Nonetheless, a similar condition arises in this experiment with the combination of TD and MN. Reforming MN is difficult because the dehydrogenated aromatic structure is relatively stable, being chemically similar to coke [40, 85]. Therefore, as it adsorbs to the catalyst, it is believed that the electron rich double bonds (pi-bonds) may form a π-complexation with the d-orbitals of the Rh metal clusters and reside on the surface for a longer time [17, 42]. Then as the accumulation of MN occurs on the surface, the surface catalytic chemistry is limited and homogeneous chemistry increases, as occurs in the blank reactor. Olefins, which are an indication of gas-phase chemistry [38, 81, 88], increase to amounts that are similar to a blank reactor (**Table 5.2**).

As the gas-phase reactions increase, there is a corresponding increase in the calculated balances of unconverted H and O. The literature suggests the gas-phase reactions lead to steam [88, 89]. In the results reported here, the atomic ratio of H/O during the time MN is present, is ~4.5/1 ±1.8, which is not consistent with the formation of steam alone as the only product containing H and O atoms.

Nevertheless, the formation of steam may be responsible for the continual decrease in H_2 yield over the 2 h during which MN is present in the feed. This continual drop in H_2 has been reported in previous studies for the CPOX of 5 wt% MN/TD at an

O/C of 1.2 and 850°C over Pt and carbide catalysts [17, 80]. To explain this behavior, Haynes et al. [80] postulated that methanation ($CO + H_2 \rightarrow CH_4 + H_2O$) or reverse water gas shift ($H_2 + CO_2 \rightarrow CO + H_2O$) reactions may be possible mechanisms for water formation. However the rates of formation of products and disappearance of reactants in these two reactions did not explain the data quantitatively. The same is true for this experiment. It is highly probable steam formation is occurring in the system, but the mechanism through which it is formed has yet to be understood.

Table 5.2 Comparison of C_2-C_6 and benzene yields between blank reactor and Rh/γ-Al_2O_3 for CPOX of TD only and after 2 hours of 5 wt% MN/TD mixture at O/C=1.2, 0.23 MPa, 900°C and 50,000 scc/$g_{catalyst}$/h.

	Blank	**Rh/γ-Al_2O_3**	
	TD only	TD only (before MN)	5 wt-% MN
Ethane	0.70	0.1	0.8
Ethylene	16.30	0.1	13.5
Propylene	17.0	n.d.	2.1
1,3-Butadiene	1.0	n.d.	1.5
1-Hexene	n.d.[a]	n.d.	1.0
Benzene	3.90	n.d.	3.8

a- n.d.- not detected

5.1.1.2 Removal of MN

After MN is removed, activity returns for the Rh/γ-Al_2O_3 catalyst, but to significantly lower levels than before MN was added. Conversion returns to 100%, but the formation of synthesis gas remains low compared to initial activity (before MN was added) and the H_2/CO ratio is <1. Olefin levels also remain high during recovery indicating that most of the Rh metal sites have been deactivated. The inability of the Rh

to fully recover activity suggests that the MN acts as an irreversible poison on the metal surface.

5.1.1.3 Carbon Formation

Because the catalyst was unable to recover activity, it is likely that carbon accumulation on the surface is responsible for the loss of activity during the recovery in TD. **Table 5.3** indicates that the addition of MN resulted in nearly 3 times as much carbon on the surface of the $Rh/\gamma\text{-}Al_2O_3$ than the CPOX of TD only. The TPO profiles for these two experiments are presented below in **Figure 5.3**. Both profiles show low temperature shoulders between ~520-535°C that correspond to carbon deposited on the rhodium metal [40, 42, 84, 85]. However, the MN profile has a much greater area for this shoulder, indicating more carbon is adsorbed to the surface of the metal during this experiment. This further suggests that the refractory MN compound (or derivative thereof) strongly adsorbs to the metal surface and is responsible for deactivation. The metal peak for the MN profile is less defined because it overlaps with a large broad peak at 670°C, which is not seen in the TD only profile. This carbon is of an intermediate activity between the metal and support peaks and is believed to be associated with carbon formed on the metal-support interface [40, 90]. Finally both profiles end with high temperature peak/shoulder between 785-795°C. This carbon peak appears to be quantitatively and qualitatively similar for both experiments, and is likely associated with the carbon deposited onto the alumina support [40, 42, 84, 85].

Table 5.3 Amount of carbon formed on Rh/γ-Al_2O_3 after CPOX of TD only and 5 wt% MN/TD respectively; 900°C, 50000 scc/$g_{catalyst}$/h.

	Carbon ($g_{carbon}/g_{catalyst}$)
TD Only	0.27
5 wt% MN/TD	0.80

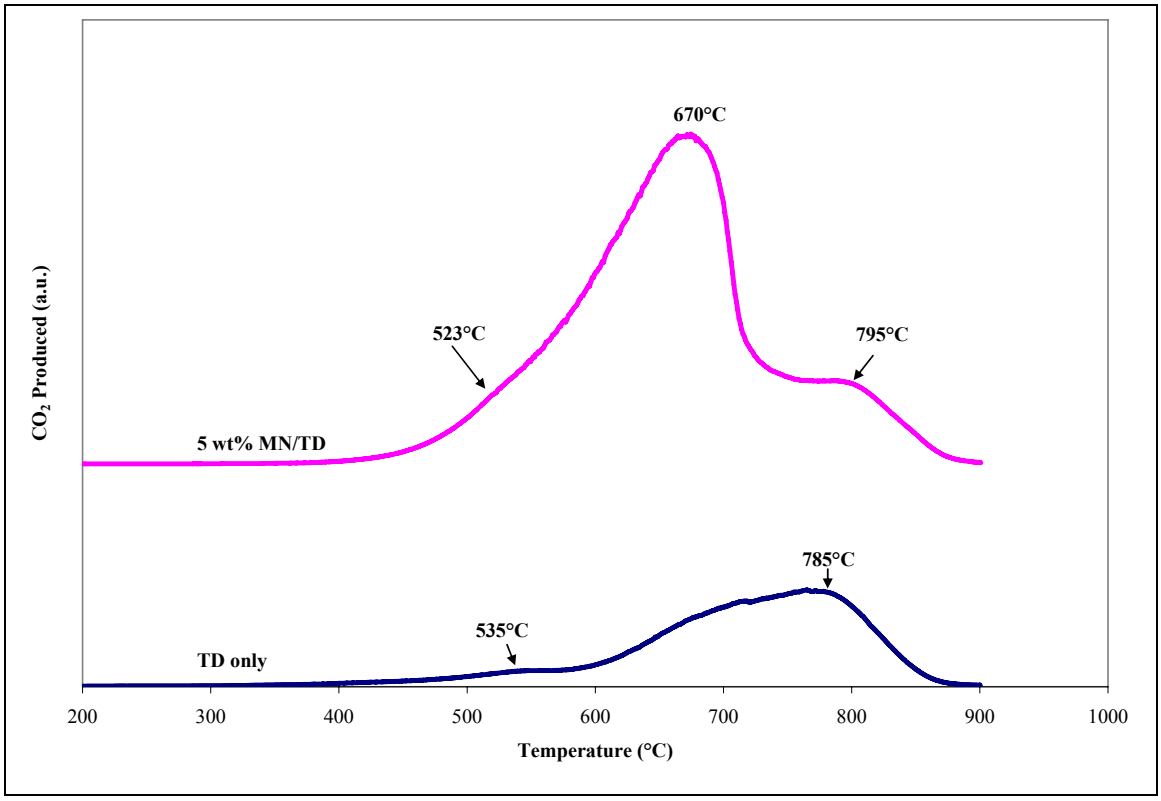

Figure 5.3 TPO profiles for Rh/γ-Al_2O_3 after CPOX of 5 wt% MN/TD and TD only.

5.1.2 LZ

5.1.2.1 Effect of MN on Synthesis Gas Yield

Step response plots detailing the effect of 5 wt% MN on the synthesis gas yields of the un-doped pyrochlore (LZ) are shown in **Figures 5.4** and **5.5**. Similar to the Rh/γ-Al_2O_3, the presence of MN decreases the hydrocarbon reforming rate on the LZ surface and therefore leads to an increase in gas phase chemistry. This is confirmed by the

increase in olefins seen in **Figure 5.5** and **Table 5.4**. This also explains the qualitatively similar behavior seen in **Figures 5.1** and **5.4**, as well as the quantitatively similar values of ethylene, propylene and benzene in **Tables 5.4** and **5.2**. But in this case, the MN has a greater effect in the deactivation of LZ, causing a 15% drop in the carbon balance over the 2 h. This imbalance in carbon indicates hydrocarbons are passing through the reactor that are larger than the detection capability of the GC, > C_6, but likely smaller than TD. Also, the synthesis gas yields drop to levels that more closely resemble a blank reactor, shown in Figure 4.1, than the Rh/γ-Al_2O_3. This behavior implies that the MN adsorbs more strongly to the active sites of the LZ than for the Rh/γ-Al_2O_3.

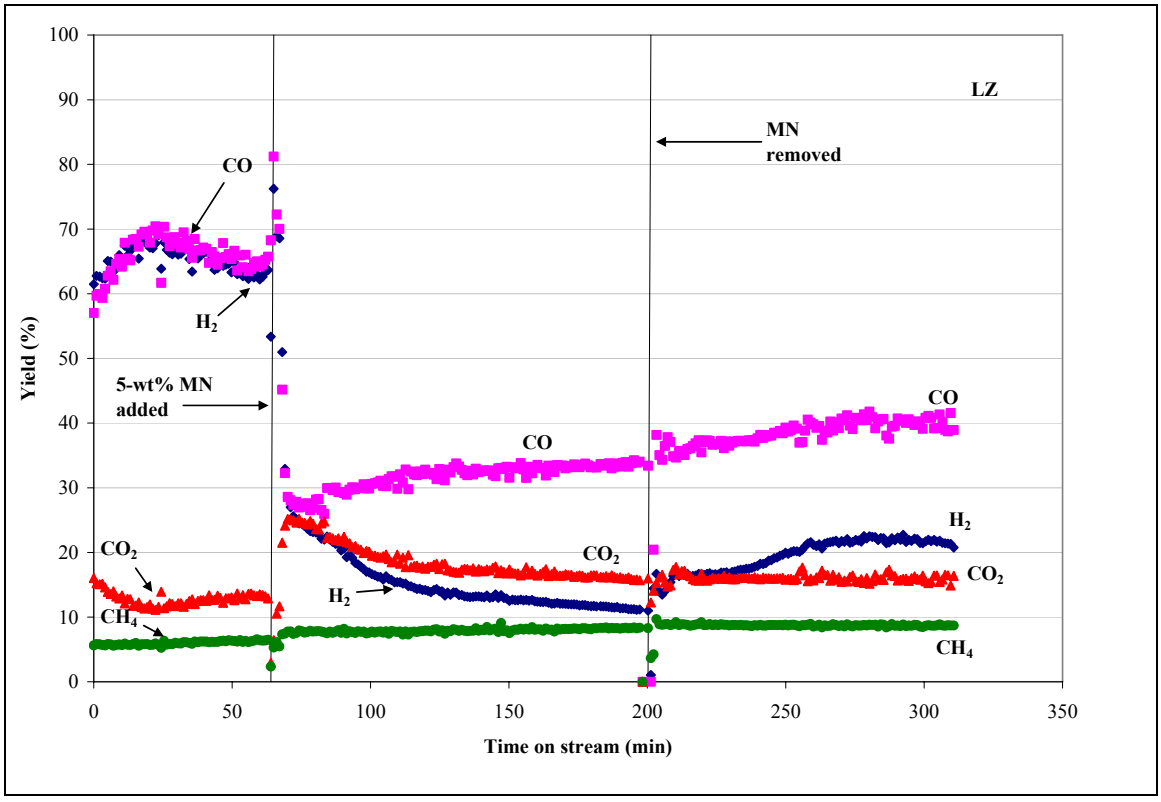

Figure 5.4 Step response plot for LZ after the addition of 5-wt% MN at an O/C=1.2, 0.23 MPa, 900°C and 50,000 scc/$g_{catalyst}$/h. H_2 (♦), CO (■), CO_2 (▲), CH_4 (●).

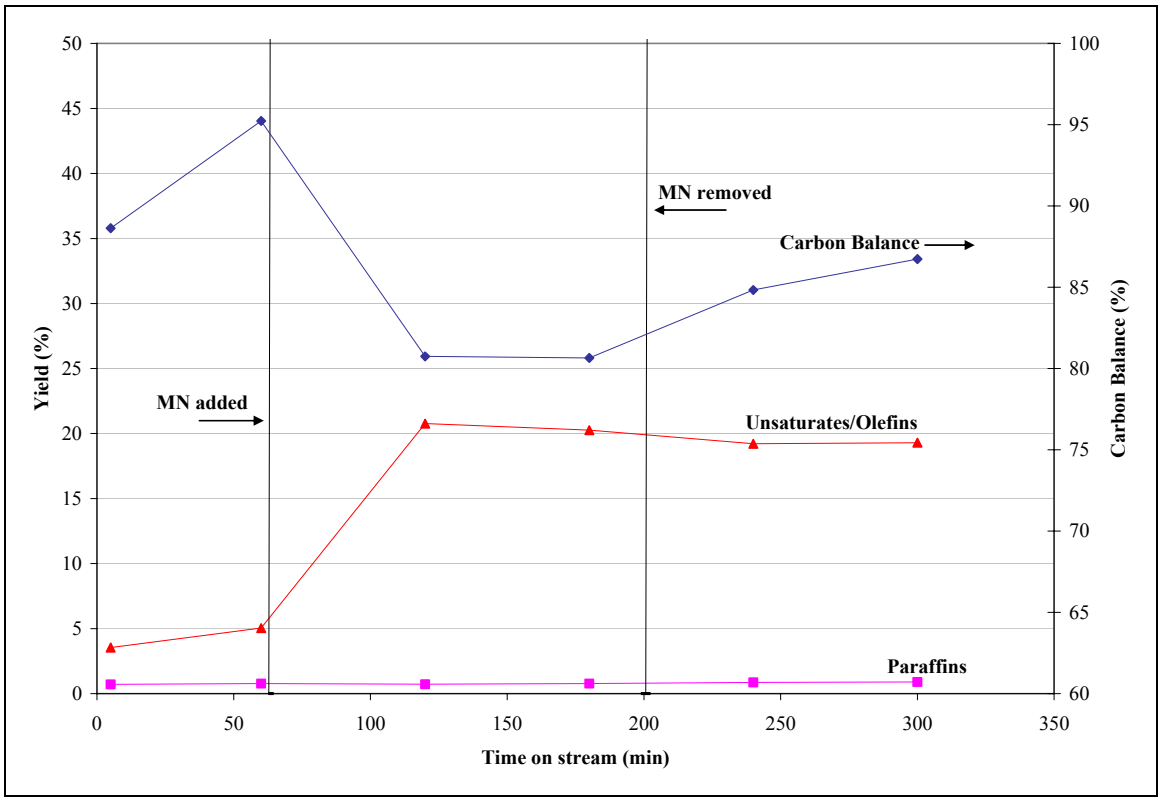

Figure 5.5 Paraffins, unsaturates yields and carbon balance for LZ during the 5-wt% MN experiment at an O/C=1.2, 0.23 MPa, 900°C and 50,000 scc/$g_{catalyst}$/h. Conversion (♦), Olefins (▲), Paraffins (■).

Table 5.4 Comparison of C_2-C_6 and benzene yields between Rh/γ-Al_2O_3 and LZ for CPOX of TD only (before MN was added) and after 2 hours of 5 wt% MN/TD mixture at O/C=1.2, 0.23 MPa, 900°C and 50,000 scc/$g_{catalyst}$/h.

	Rh/γ-Al_2O_3		**LZ**	
	TD only (before MN)	5 wt% MN	TD only (before MN)	5 wt-% MN
Ethane	0.1	0.8	0.6	0.8
Ethylene	0.1	13.5	1.0	14.7
Propylene	n.d.[a]	2.1	0.2	2.4
1,3-Butadiene	n.d.	1.5	n.d.	n.d.
1-Hexene	n.d.	1.0	n.d.	n.d.
Benzene	n.d.	3.8	0.2	3.1

[a]- n.d.- not detected

The decrease in H_2 yield during the 2 h MN is present for the LZ is consistent with the formation of steam, since a mass balance shows that the H/O atomic ratio during

this part of the experiment was 2.3 ±0.7. The reverse water gas shift reaction ($H_2 + CO_2 \rightarrow CO + H_2O$) might account for some of the H_2 consumption, as Figure **5.4** shows CO and CO_2 levels diverging at qualitatively similar rates. A regression analysis performed on the CO and CO_2 data over the 2 h during which MN is in the feed indicates the rate of formation of CO and disappearance of CO_2 are not equal. However, the rates do become equal, at ~1.0E-6 mole/min, after MN has been in the feed for 1 h. This may suggest that after the catalyst activity has significantly decreased, the reverse water gas shift may in fact be a likely mechanism for water formation in the system.

5.1.2.2 Removal of MN

The CPOX activity is unable to recover because the MN poisons the LZ surface and deactivates it as a catalyst. **Figure 5.4** shows that after switching back to TD only, H_2 and CO yields increase slightly for the LZ catalyst, but remain significantly lower compared to pre-MN values. The carbon balance also recovers, but does not return to pre-MN values. The high levels of olefins that remain after the MN has been removed (**Figure 5.5**) suggest this can be explained by the fact that the catalytic activity has been displaced by the gas-phase chemistry still occurring in the system [81, 88]. In addition, H and O balances show that the H/O ratio continues to be ~ 2.3 ±.7 throughout recovery, suggesting that steam formation is still occurring and that catalytic activity has been lost.

5.1.2.3 Carbon Formation

The addition of MN caused a greater amount carbon to be formed on the LZ surface than the CPOX of TD only, just as it did for the Rh/γ-Al_2O_3. However, **Table 5.5** reveals that the addition of MN resulted in 6.9 times more carbon on the LZ surface than

CPOX of TD only, compared to only 3 greater for the Rh/γ-Al_2O_3. This large amount of carbon formed is likely the reason for the deactivation of the catalyst as well as its inability to recover activity after the MN was removed. TPO results shown in **Figure 5.6** compare the carbon formed on the LZ after the CPOX of TD only and the 5 wt% MN/TD experiments. As discussed in Chapter 4, the peaks seen in the TD only profile indicate two different reactivities of the coke adsorbed on the surface. The low temperature peak (575°C) corresponds to a hydrogenated, or soft, form of coke, and the high temperature peak (763°C) can be attributed to a dehydrogenated form of coke [84]. Unfortunately, these peaks are indistinguishable in the MN profile. However, both profiles indicate the carbon is oxidized on the LZ over a similar temperature range, ~400-900°C, which suggests the carbon seen in the two profiles may be qualitatively similar, just significantly more of it after the MN experiment.

Table 5.5 Amount of carbon formed on LZ pyrochlore after CPOX of TD only and 5 wt% MN/TD respectively; 900°C, 50000 scc/$g_{catalyst}$/h. Results are compared to carbon formed on Rh/γ-Al_2O_3 after CPOX 5 wt% MN/TD experiment; 900°C, 50000 scc/$g_{catalyst}$/h.

Catalyst	Carbon ($g_{carbon}/g_{catalyst}$)
LZ (TD only)	0.30
LZ (After 5 wt% MN/TD)	2.06
Rh/γ-Al_2O_3 (After 5 wt% MN/TD)	0.80

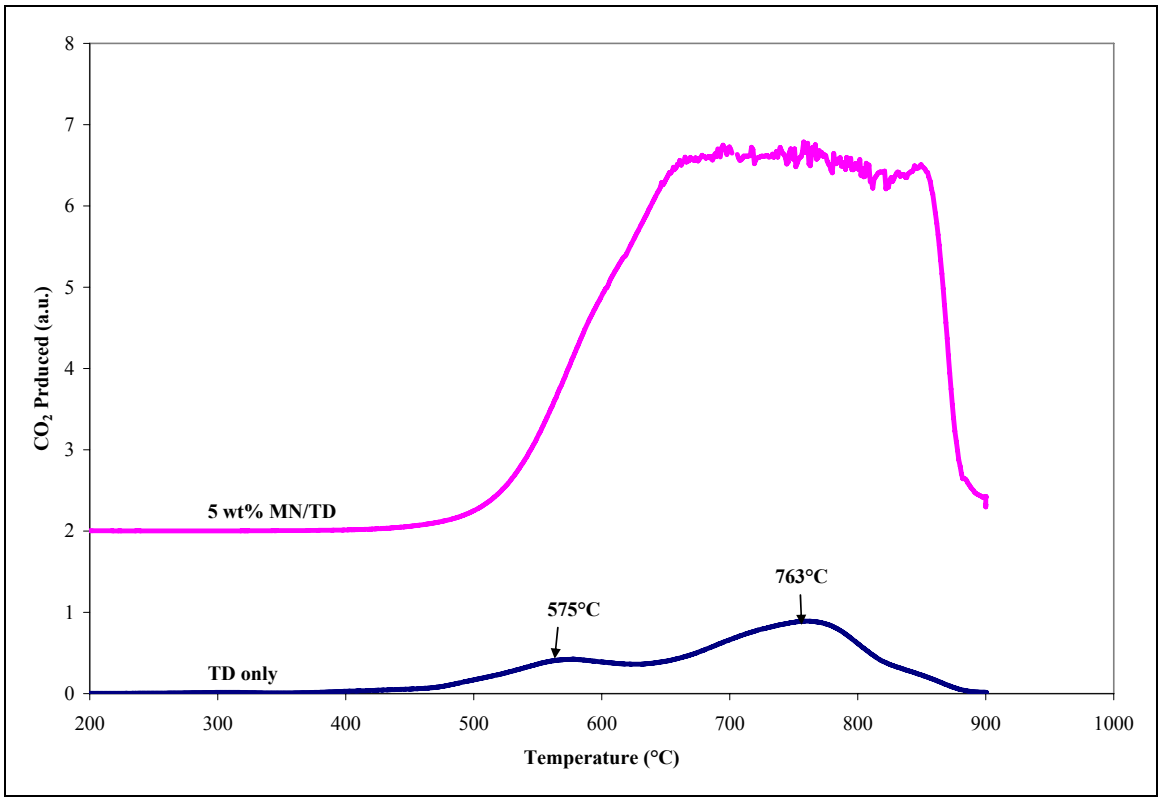

Figure 5.6 TPO profiles for LZ after CPOX of 5 wt% MN/ TD and TD only.

5.1.3 LRZ

5.1.3.1 Effect of MN on Synthesis Gas Yield

Figures 5.7 and 5.8 illustrate that the substitution of rhodium into the structure enhances the performance of both the metal and pyrochlore material in the presence of MN. After the catalyst is exposed to MN, the sites producing H_2 and CO are deactivated simultaneously at the same rate of 0.18% H_2 or CO/min with an H_2/CO ratio <1, while carbon balance remains at 100% during the 2 h. It is unclear over the time scale of this experiment whether the synthesis gas yields would eventually stabilize or continue to decline until the catalyst is completely deactivated. Still, this suggests that the rhodium metal undergoes a gradual deactivation, rather than an immediate deactivation as is the

case for Rh/γ-Al_2O_3 and LZ. It is also evident that dispersing the rhodium throughout the structure creates a more reactive pyrochlore surface which is able to decrease the rate of adsorption of MN and prevent subsequent deactivation of catalytic activity. This is consistent with the formation of fewer olefins (**Figure 5.8**) after 2 h of MN in the feed compared to the other catalysts, which indicates less gas phase chemistry is occurring in the system [81, 88]. This can also be seen in the C_2-C_6 product distribution in **Table 5.6**. High levels of ethylene, propylene and benzene are seen as products for Rh/γ-Al_2O_3 and LZ after they have lost significant activity due to MN, whereas there are quantitatively less of these for the LRZ.

As these gas-phase reactions are occurring, the decrease in H_2 yield for the LRZ, while MN is present, can be attributed to the formation of steam, because the mass balance shows unconverted H and O are in the correct ratio of 2/1 ±1.5.

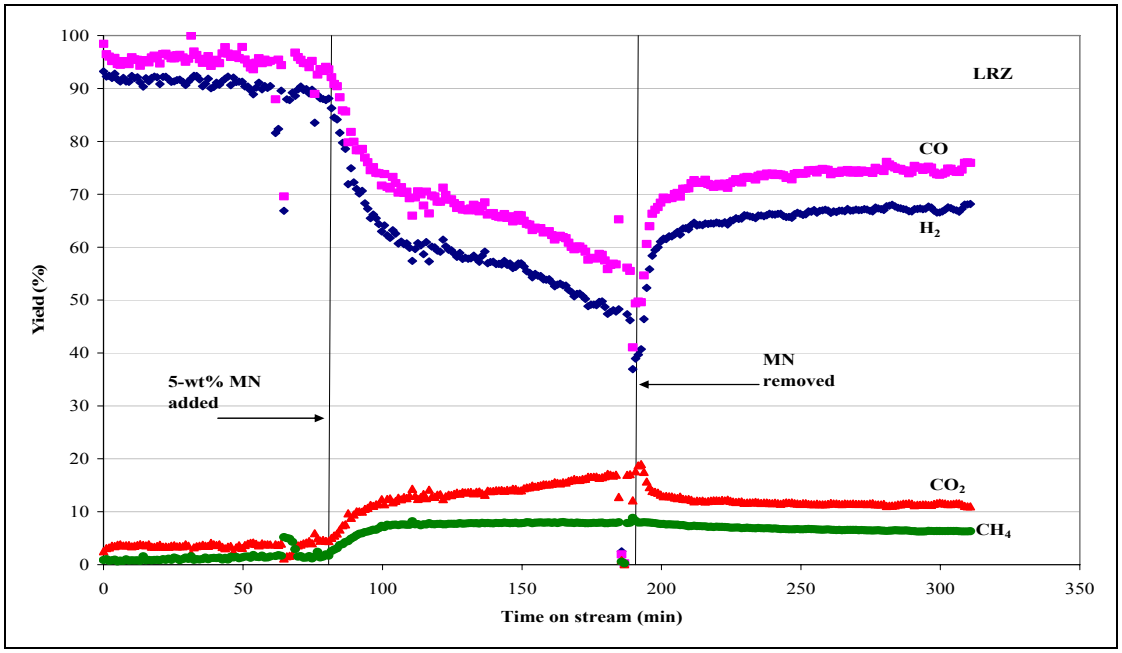

Figure 5.7 Step response plot for LRZ after the addition of 5-wt% MN at an O/C=1.2, 0.23 MPa, 900°C and 50,000 scc/$g_{catalyst}$/h. H_2 (♦), CO (■), CO_2 (▲), CH_4 (●).

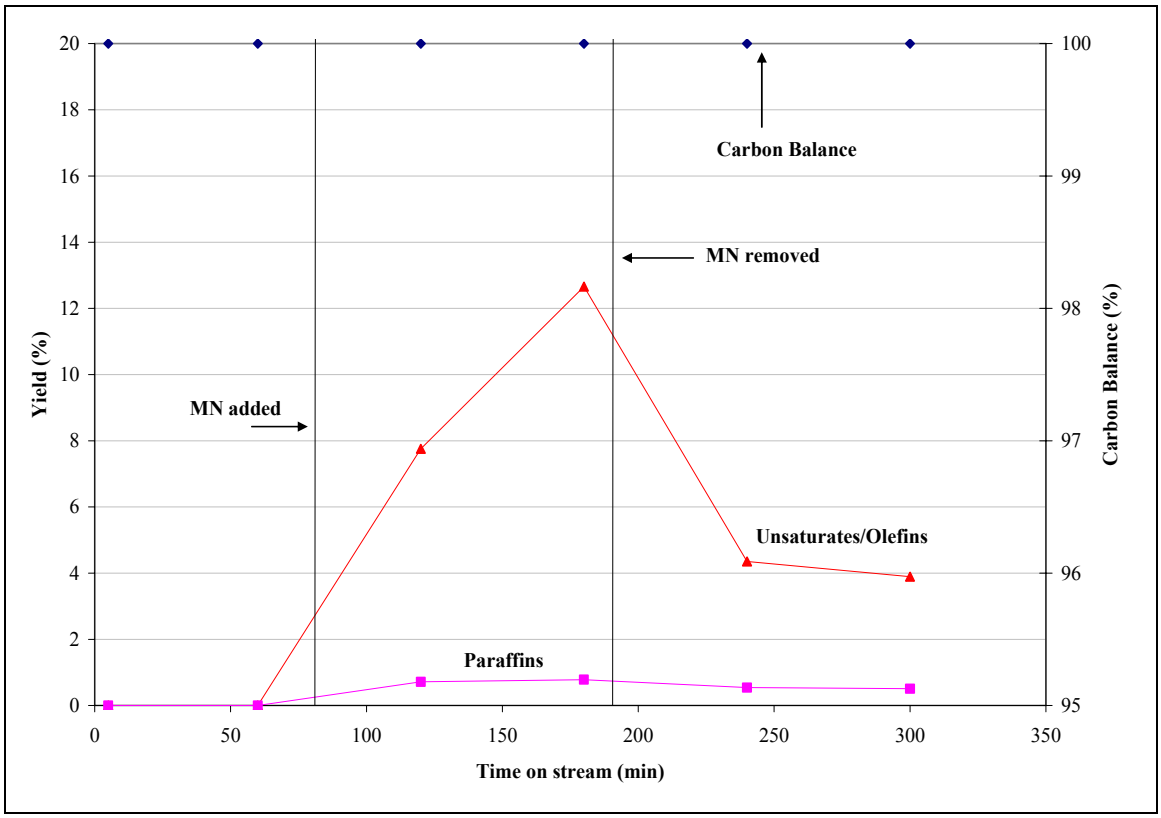

Figure 5.8 Paraffins, unsaturates yields and carbon balance for LRZ during the 5-wt% MN experiment at an O/C=1.2, 0.23 MPa, 900°C and 50,000 scc/$g_{catalyst}$/h. Conversion (♦), Olefins (▲), Paraffins (■).

Table 5.6 Comparison of C_2-C_6 and benzene yields between Rh/γ-Al_2O_3, LZ and LRZ for CPOX of TD only (before MN was added) and after 2 hours of 5 wt% MN/TD mixture at O/C=1.2, 0.23 MPa, 900°C and 50,000 scc/$g_{catalyst}$/h.

	Rh/γ-Al_2O_3		**LZ**		**LRZ**	
	TD only	5 wt% MN	TD only	5 wt-% MN	TD only	5 wt-% MN
Ethane	0.1	0.8	0.6	0.8	n.d.	0.8
Ethylene	0.1	13.5	1.0	14.7	n.d.	8.8
Propylene	n.d.[a]	2.1	0.2	2.4	n.d.	1.4
1,3-Butadiene	n.d.	1.5	n.d.	n.d.	n.d.	n.d.
1-Hexene	n.d.	1.0	n.d.	n.d.	n.d.	n.d.
Benzene	n.d.	3.8	0.2	3.1	n.d.	2.5

[a-] n.d.- not detected

5.1.3.2 Removal of MN

Once MN is removed from the feed, the LRZ immediately recovers 25% of the pre-MN synthesis gas activity and olefin yield drops to about 4%. However, over the course of the recovery, synthesis gas and olefin yields remain at these levels and show no indication that they will return fully to pre-MN values. The inability to fully recover activity is evidence that the MN acts as a poison to the LRZ catalyst, just as it did for the Rh/γ-Al_2O_3 and LZ. The substitution of Rh into the pyrochlore may slow the deactivation rate, but it appears that over a longer exposure time, LRZ may become inactive.

5.1.3.3 Carbon Formation

Table 5.7 shows LRZ has less total carbon adsorbed on the surface than the non-substituted LZ. However, interestingly, the LRZ has a higher amount of oxidizible carbon on the surface compared to the Rh/γ-Al_2O_3, but is more resistant to deactivation by the MN. This suggests that the active sites for the Rh/γ-Al_2O_3 (the metal), are favorable sites for carbon formation. The TPO profile for the Rh/γ-Al_2O_3 indicates an increase in carbon formed on the metal and metal-support interface after being exposed to MN. On the other hand, the gradual deactivation for LRZ indicates that there are no concentrations of active sites that can be poisoned immediately; rather the active sites (metal) are dispersed throughout the surface. As a result, the carbon forms more indiscriminately on the surface and gradually accumulates over time. This is likely the reason that the TPO profile for the LRZ qualitatively resembles the profile for LZ pyrochlore after reforming the TD only, as shown in **Figure 5.9**, and **4.6**. As these

profiles are similar, it appears the low temperature shoulder (~ 574°C) may be attributed to the low temperature carbon that adsorbs onto the LZ surface, as shown in **Figure 4.6**.

Table 5.7 Carbon deposited on LRZ and LZ as well as Rh/γ-Al_2O_3 after CPOX 5 wt-% MN/TD experiment; 900°C, 50000 scc/$g_{catalyst}$/h.

Catalyst	Carbon Accumulated ($g_{carbon}/g_{catalyst}$)
LRZ	1.20
LZ	2.06
Rh/γ-Al_2O_3	0.80

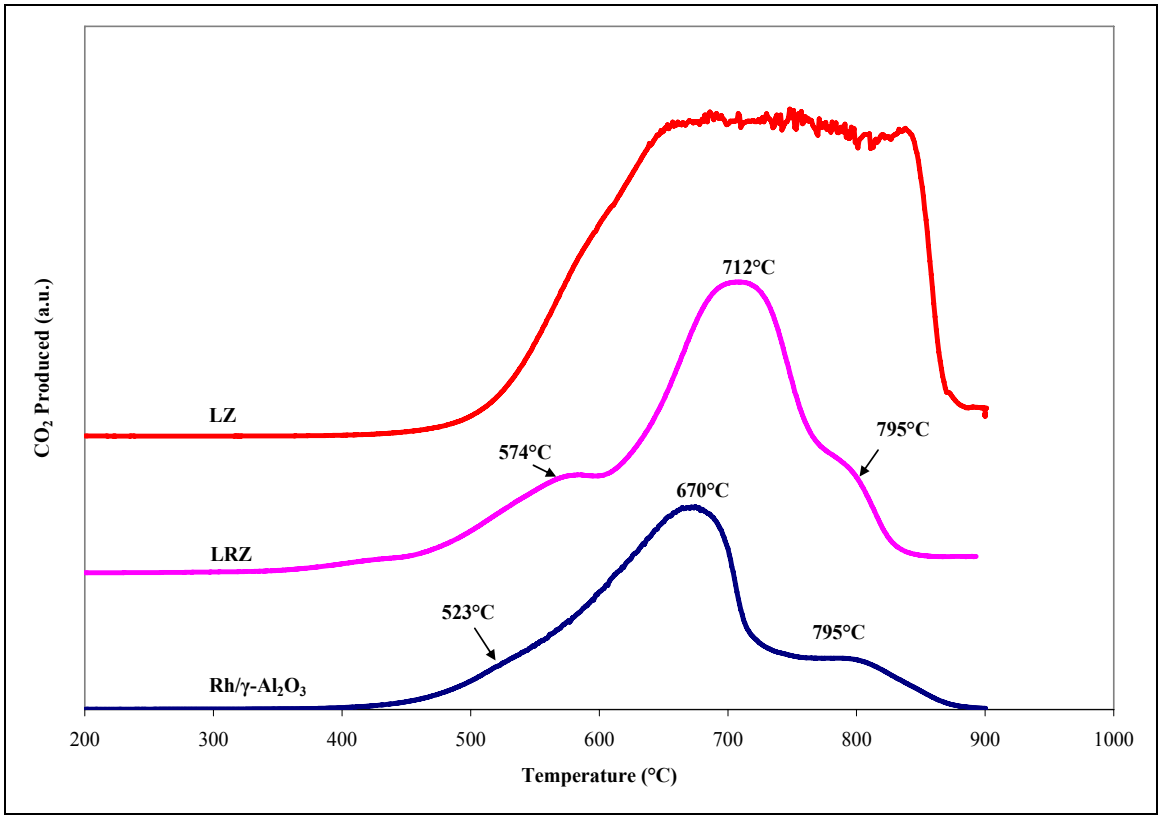

Figure 5.9 TPO profiles from LRZ, LZ and Rh/γ-Al_2O_3 after CPOX of 5 wt% MN/TD.

5.1.4 LSRZ

5.1.4.1 Effect of MN on Synthesis Gas Yield

Substitution of strontium drastically reduces the adverse effects of MN on catalytic activity. During the time MN is in the feed, shown in **Figure 5.10**, H_2 and CO drop modestly to stationary levels. Strontium addition leads to relatively little gas phase chemistry in the system, as only a small amount of olefins and paraffins are produced (**Figure 5.11**). **Table 5.8** shows that compared to the other catalysts, LSRZ has significantly less gas phase chemistry occurring after MN has been present in the feed for 2 h. The resistance to deactivation may be due to the presence of lattice oxygen ion conductivity in the bulk structure. It is likely the addition Sr^{2+} into the A-site of the pyrochlore creates oxygen vacancies in throughout the lattice [57, 60, 86]. At the high reaction temperature, lattice oxygen becomes mobile throughout the bulk material and the oxygen coordinated with the metal may be catalyzed to react with locally adsorbed MN. This would then destabilized the cyclic molecule and create a more reactive component on the surface. After the reaction, the oxygen vacancy near the metal is likely replenished by O_2 or H_2O from gas phase. Also, although there is very little gas phase chemistry occurring while the MN is present, steam formation can be assumed to be responsible for the drop in H_2 yield as the mass balance shows the atomic ratio of H/O to be 1.3/1 ±1.7.

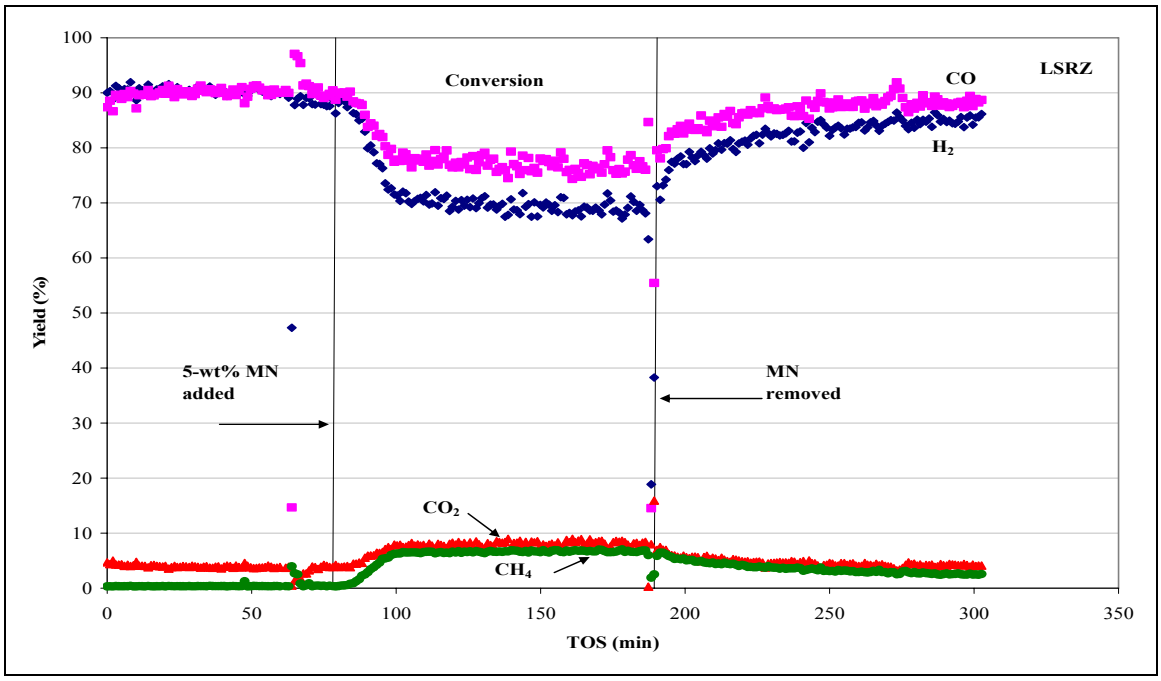

Figure 5.10 Step response plot for LSRZ after the addition of 5-wt% MN at an O/C=1.2, 0.23 MPa, 900°C and 50,000 scc/$g_{catalyst}$/h. H_2 (♦), CO (■), CO_2 (▲), CH_4 (●).

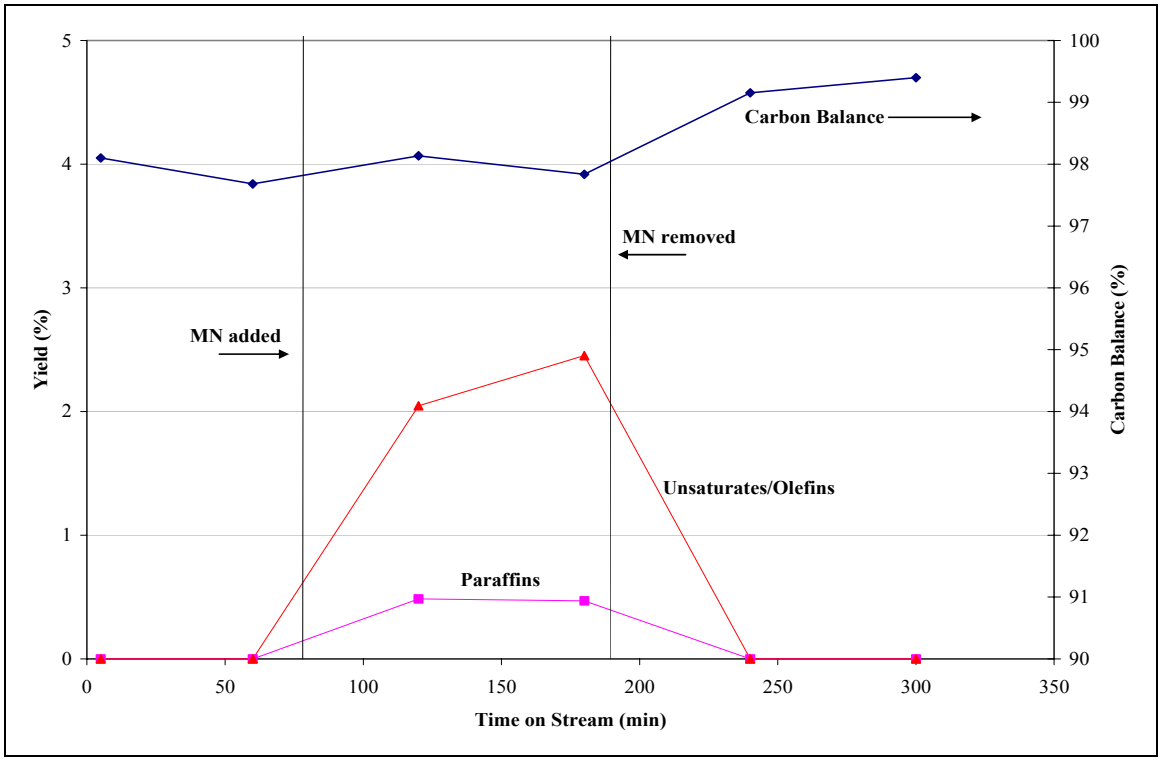

Figure 5.11 Paraffins, unsaturates yields and carbon balance for LSRZ during the 5-wt% MN experiment at an O/C=1.2, 0.23 MPa, 900°C and 50,000 scc/$g_{catalyst}$/h. Conversion (♦), Olefins (▲), Paraffins (■).

Table 5.8 Comparison of C_2-C_6 and benzene yields between Rh/γ-Al_2O_3 and pyrochlores for CPOX of TD only (before MN was added) and after 2 hours of 5 wt% MN/TD mixture at O/C=1.2, 0.23 MPa, 900°C and 50,000 scc/$g_{catalyst}$/h.

	Rh/γ-Al_2O_3		**LZ**		**LRZ**		**LSRZ**	
	TD only	5 wt% MN	TD only	5 wt-% MN	TD only	5 wt-% MN	TD only	5 wt-% MN
Ethane	0.1	0.8	0.6	0.8	n.d.	0.8	n.d.	0.5
Ethylene	0.1	13.5	1.0	14.7	n.d.	8.8	n.d.	1.6
Propylene	n.d.[a]	2.1	0.2	2.4	n.d.	1.4	n.d.	0.2
1,3-Butadiene	n.d.	1.5	n.d.	n.d.	n.d.	n.d.	n.d.	n.d.
1-Hexene	n.d.	1.0	n.d.	n.d.	n.d.	n.d.	n.d.	n.d.
Benzene	n.d.	3.8	0.2	3.1	n.d.	2.5	n.d.	0.8

a- n.d.- not detected

5.1.4.2 Removal of MN

After MN is removed, activity almost fully returns for the LSRZ. There is a slow recovery period, which may indicate there may be some residual MN on the surface. Also, as activity returns, olefin and paraffin yields drop to near zero (Figure 5.11). The ability to recover activity suggests MN acts as a kinetic inhibitor to the reforming reaction on the LSRZ surface, rather than a poison like the other three catalysts, at least over the time scale of these experiments.

5.1.4.3 Carbon Formation

The amount of carbon formed on the pyrochlores follows the trend LZ>LRZ>LSRZ (**Table 5.9**) because the successive substitution of Rh and Rh + Sr into the pyrochlore leads to a more reactive surface. As seen in Chapter 4 for the CPOX of TD only, substitution of Sr with Rh enhanced the pyrochlores' resistance to carbon formation. The mobilized lattice oxygen created by Sr substitution prevents the accumulation of MN on the active sites of the pyrochlore. However, the LSRZ surface is

not without carbon. The TPO profile in **Figure 5.12** shows the carbon is qualitatively similar to the LRZ. Both profiles have shoulders at 530°C and 795°C as well as a main peak around 670°C. However, the peaks are less defined for the LSRZ because there is less carbon adsorbed to the surface, and the total carbon formation is greatly reduced (**Table 5.9**).

Table 5.9 Carbon deposited on pyrochlores and Rh/γ-Al_2O_3 after CPOX 5 wt-% MN/TD experiment; 900°C, 50000 scc/$g_{catalyst}$/h.

Catalyst	Carbon Accumulated ($g_{carbon}/g_{catalyst}$)
LSRZ	0.67
LRZ	1.20
LZ	2.06
Rh/γ-Al_2O_3	0.80

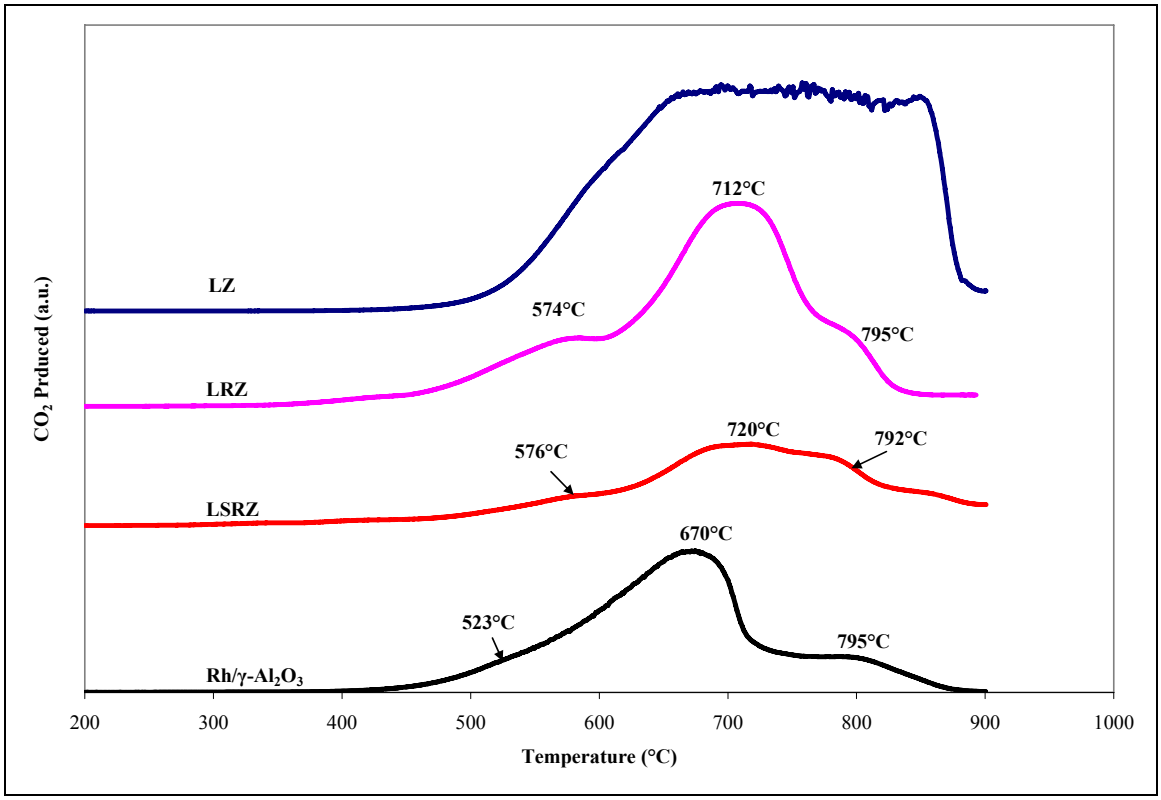

Figure 5.12 TPO profiles from LSRZ, LRZ, LZ and Rh/γ-Al_2O_3 after CPOX 5 wt% MN/TD.

Chapter 6. Results and Discussion: Effects of Sulfur

The concentration of sulfur varies in different fuels. It can be as low as 50 ppmw as it is in commercial diesel, or it can be as high as 3000 ppmw, as in some military fuels [17, 91]. Sulfur is usually present in the form of benzothiophenes. These compounds tend to be difficult to remove through the hydro-desulfurization process in refining because of the spatial hindrance of the two phenyl groups [92]. In the reforming of liquid fuels, sulfur has been seen to deactivate the metal catalysts [17, 42, 93, 94]. In this chapter 1000 ppmw dibenzothiophene (DBT), a well-known compound in diesel, will be used as a surrogate sulfur compound in TD to assess the sulfur tolerance of each catalyst.

The results, discussed below, show that high levels of sulfur act as a kinetic inhibitor to the CPOX reaction over each of the pyrochlores, and in doing so reduce the amount of carbon formed on the surface compared to MN. Also, the substitution of Rh into the structure decreases deactivation of active metals sites compared to supported Rh/γ-Al_2O_3. Finally, the addition of Sr and Rh to the pyrochlore shows the highest synthesis gas yields in the presence of sulfur and the lowest amount of carbon formed compared to the other 3 catalysts.

6.1 Reforming Results: 1000 ppmw Sulfur (as dibenzothiophene)

Similar to the MN experiment, the CPOX of TD was run for 1 h before sulfur was added. As shown **Table 6.1**, the H_2 and CO yields for the Rh catalysts Rh/γ-Al_2O_3, LRZ and LSRZ were again comparable to the equilibrium levels for the CPOX of TD only, which are presented in Table 4.1. Consistent with Sections 4.1.4 and 5.1.2, the unsubstituted pyrochlore LZ has the lowest synthesis gas yields. 1000 ppmw DBT was

added to the feed after 1 h. After 1 h, 1000 ppmw sulfur was added to the feed in the form of DBT. Like MN, the presence of sulfur decreased CPOX activity for each catalyst, but the effects on product yield and carbon formation varied.

Table 6.1 Synthesis gas yields for each catalyst during the CPOX of TD after 1 h time on stream at an O/C=1.2, 0.23 MPa, 900°C and 50,000 scc/$g_{catalyst}$/h.

	Rh/γ-Al_2O_3	LZ	LRZ	LSRZ
H_2 Yield (%)	81.0	69.0	90.0	89.0
CO Yield (%)	76.0	72.0	95.0	90.0

6.1.1 Rh/γ-Al_2O_3

6.1.1.1 Effect of DBT on Synthesis Gas Yield

The results of the addition of 1000 ppmw sulfur on product selectivity and conversion for Rh/γ-Al_2O_3 are shown in **Figures 6.1 and 6.2**. Over the two hours that sulfur was present, the deactivation was comparable to the effects of MN in Section 5.1.1.1- H_2 yield decreased continuously while CO dropped to a stationary level. Also, the C_2-C_6 product selectivity, presented in **Table 6.2**, shows the presence of sulfur caused an increase in olefin yield comparable to that observed due to the addition of MN. However, the carbon balance dropped about 10% in the presence of sulfur, in contrast to the 2% decrease due to the addition of MN, shown in Figure 5.2. Similar effects of sulfur have been reported during the CPOX of 1000 ppmw DBT/TD at an O/C of 1.2 and 850°C over Pt and carbide catalysts [42, 80].

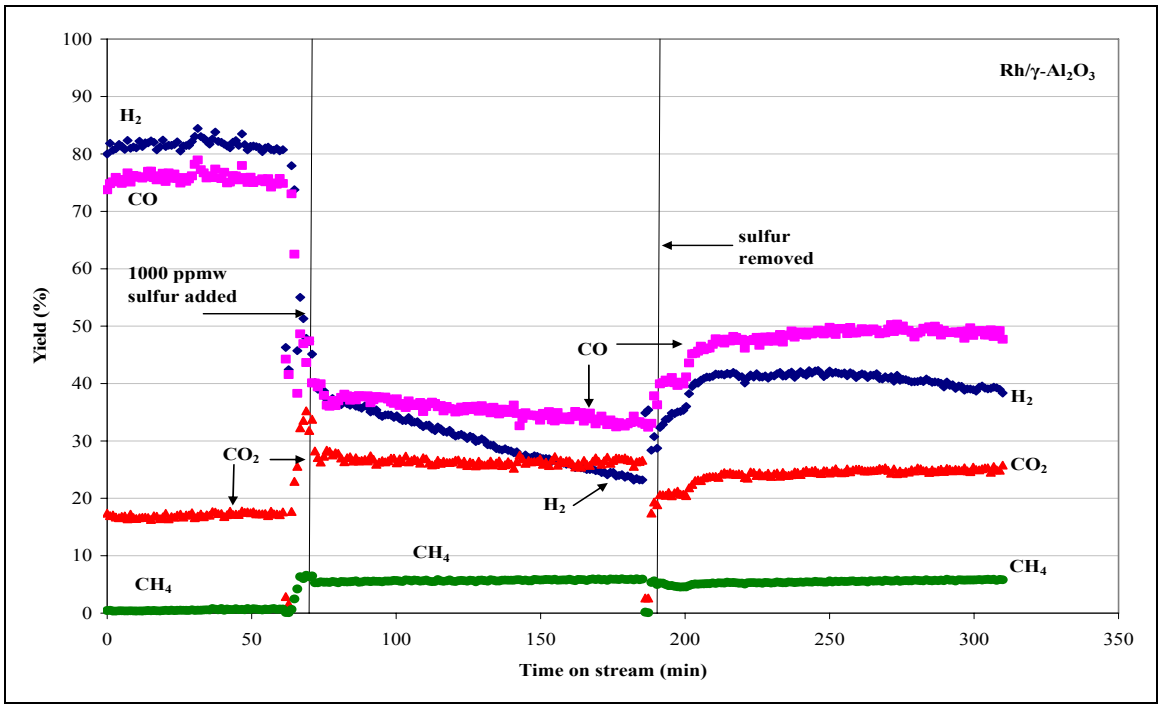

Figure 6.1 Step response plot for Rh/γ-Al_2O_3 after the addition of 1000 ppmw DBT at an O/C=1.2, 0.23 MPa, 900°C and 50,000 scc/$g_{catalyst}$/h. H_2 (♦), CO (■), CO_2 (▲), CH_4 (●).

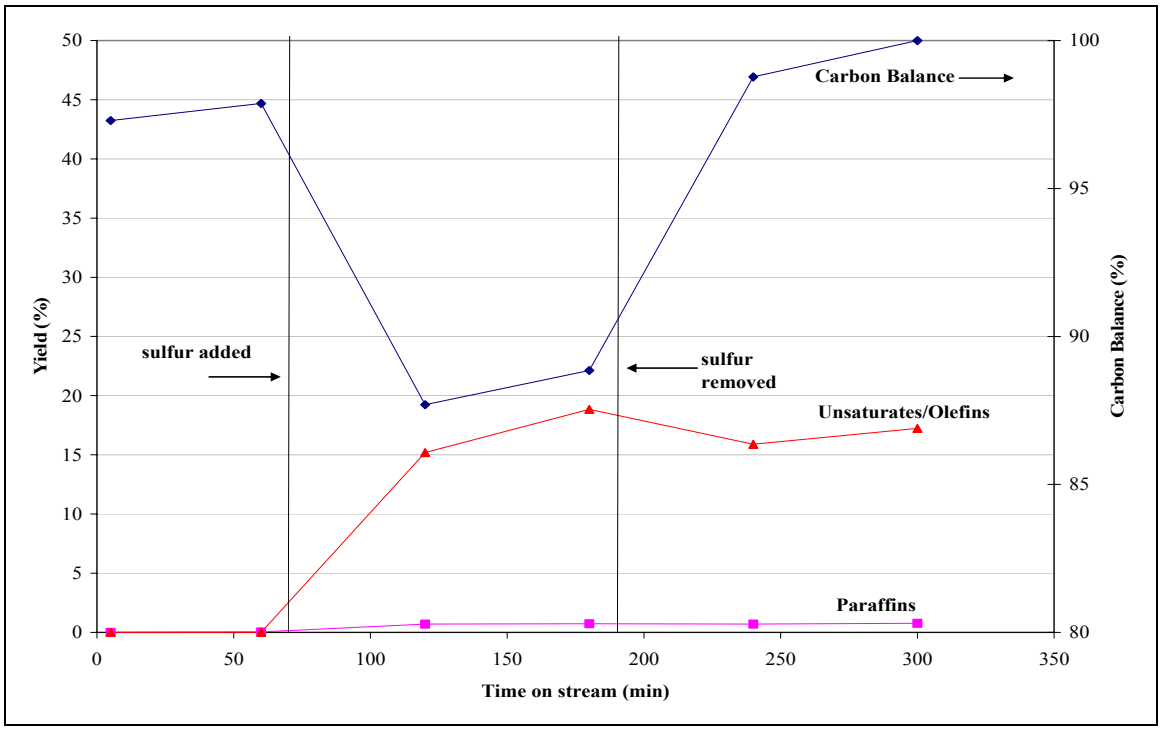

Figure 6.2 Paraffins, unsaturates yields and carbon balance for Rh/γ-Al_2O_3 during the 1000 ppmw DBT/TD experiment at an O/C=1.2, 0.23 MPa, 900°C and 50,000 scc/$g_{catalyst}$/h. Conversion (♦), Olefins (▲), Paraffins (■).

Table 6.2 Comparison of C_2-C_6 and benzene yields between blank reactor and Rh/γ-Al_2O_3 during CPOX of 5 wt% MN/TD and 1000 ppmw DBT/TD experiments. Rh/γ-Al_2O_3 yields produced after CPOX of TD only (before MN or DBT was added) and after 2 hours of 5 wt% MN or 1000 ppmw DBT in TD at O/C=1.2, 0.23 MPa, 900°C and 50,000 scc/$g_{catalyst}$/h.

	Blank	**Rh/γ-Al_2O_3**			
	TD only	TD only (before MN)	5 wt% MN	TD only (before DBT)	1000 ppmw DBT
Ethane	0.70	0.1	0.8	n.d.	0.7
Ethylene	16.30	0.1	13.5	n.d.	11.2
Propylene	17.0	n.d.	2.1	n.d.	2.3
1,3-Butadiene	1.0	n.d.	1.5	n.d.	1.20
1-Hexene	n.d.[a]	n.d.	1.0	n.d.	0.8
Benzene	3.90	n.d.	3.8	n.d.	3.4

[a] n.d.- not detected

The effects of sulfur (DBT) on the catalytic activity of Rh/γ-Al_2O_3 qualitatively and quantitatively resemble the effects of MN. One explanation is that DBT, like MN, blocks active sites and decreases the hydrocarbon reforming rate [23, 42]. Deactivation by DBT may be attributed to the electron-dense rhodium metal clusters forming strong bonds to the lone pair electrons on the sulfur molecules [42, 93, 94]. As metal sites are blocked by sulfur, the reactants can no longer reach the metal surface, similar to effects of 1-MN, and an increase in homogeneous reactions occurs in the system. However, the DBT molecules also have two phenyl groups which contain a stable aromatic structure that can adsorb strongly to active metal sites. These too, likely contribute to the deactivation of the metal along with the sulfur. Thus, as DBT has a similar effect on catalyst activity as MN, longer exposure to the DBT will continue to deactivate the catalyst until the reaction products resemble a blank reactor.

As DBT deactivates the catalyst, the continual decrease in H_2 yield can also likely be attributed to the formation of steam, because mass balances on unconverted H and O

molecules indicate an H/O ratio 2.1/1 ± 1.2 during the time DBT was present. This rate of H_2 consumption was comparable to that observed in the presence of MN. A regression analysis shows that the addition of 5 wt% MN to TD caused a 0.19% decrease in H_2/min, while 1000 ppmw DBT in TD resulted in a loss of 0.14% H_2/min. This suggests that MN and DBT deactivate the Rh/γ-Al_2O_3 catalyst at similar rates and possibly via the same mechanism.

6.1.1.2 Removal of DBT

After DBT is removed from the feed, the Rh/γ-Al_2O_3 is unable to recover to initial activity. Although the carbon balance returns to ~ 100% (pre-DBT value), H_2 and CO yields increase only 15% and 19% respectively once DBT is removed. They remain at these levels at an H_2/CO < 1 throughout 2-h recovery period. However, selectivity to olefins remains high during recovery, indicating gas-phase reactions are occurring and the catalyst has been, to some extent, deactivated. From this behavior is it concluded that the DBT also irreversibly poisons the catalytic activity of the Rh/γ-Al_2O_3.

6.1.1.3 Carbon Formation

The presence of sulfur appears to poison the activity of the catalyst through carbon formation on the active sites, rather than by poisoning the metal itself. **Table 6.3** shows DBT leads to 3.3 times the mass of carbon on the surface compared to CPOX of TD only, and about 1.1 times more than the CPOX of 5 wt% MN/TD. As was discussed in Section 5.1.1.3, the increase in carbon formation on active sites by MN was responsible for the lower synthesis gas yields and hence larger olefin yields formed during the recovery in TD only, as compared to pre-MN yields. Since the catalyst

suffered almost the same activity loss after the DBT was removed, the presence of high levels of sulfur appears to deactivate the catalyst through the same mechanism: carbon formation on active sites. However, the Rh/γ-Al_2O_3 catalyst showed a lower recovery after DBT was removed compared to MN, as the synthesis gas yields recovered at a lower H_2/CO ratio and olefin yields remained high at almost constant to levels seen in the presence of DBT. This suggests that the DBT leads to greater amount of carbon on the active sites.

The TPO profiles for these experiments are shown in **Figure 6.3**. Both DBT and MN lead to more carbon on the same area of the catalyst surface compared to CPOX of TD only. As discussed in Chapter 5 Section 5.1.1.3, the broad shoulder at 530°C and larger peak at 681°C indicate that the presence of DBT leads to more carbon accumulation on the Rh metal and Rh metal-support interface, respectively, than does CPOX of TD only [40, 42, 84, 85]. However, all profiles show a similar high temperature shoulder between 785°C and 810°C, which corresponds to carbon adsorbed onto the alumina support [40, 42, 84, 85].

Table 6.3 Amount of carbon formed on Rh/γ-Al_2O_3 after CPOX of TD only, 5 wt% MN/TD, and 1000 ppmw DBT/TD experiments; 900°C, 50000 scc/$g_{catalyst}$/h.

	Carbon ($g_{carbon}/g_{catalyst}$)
TD Only	0.27
5 wt% MN/TD	0.80
1000 ppmw DBT/TD	0.90

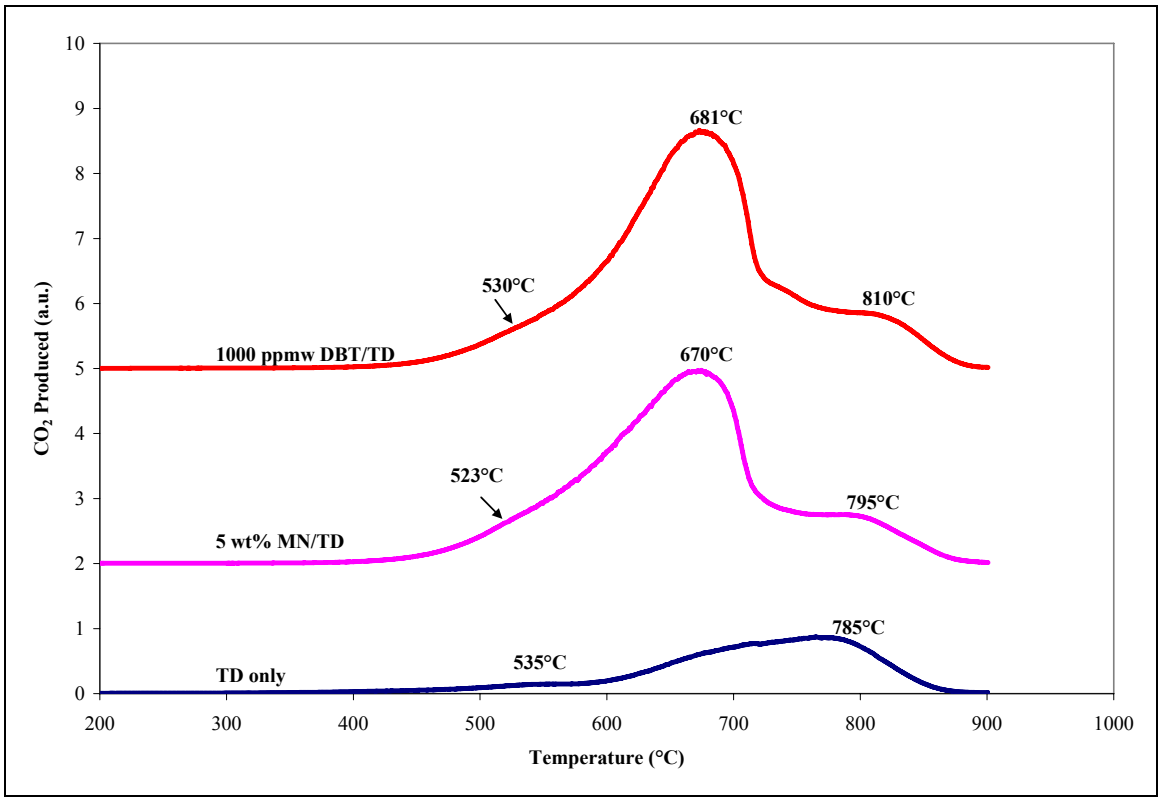

Figure 6.3 TPO profiles for Rh/γ-Al_2O_3 after CPOX of 1000 ppmw DBT/TD, 5-wt% MN/TD, and TD only.

6.1.2 LZ

6.1.2.1 Effect of DBT on Synthesis Gas Yield

The effects of sulfur on the CPOX activity and conversion of LZ are shown in **Figures 6.4 and 6.5**. After the introduction of DBT, the selectivity to synthesis gas decreases immediately. However, unlike the effects of MN, the carbon balance remains close to 100% and the H_2 and CO yields both drop ~45% to stationary levels. These levels decline slightly over the 2 h, but they remain at an H_2/CO ratio of ~ 1 while DBT is present. This suggests that sulfur acts as a kinetic inhibitor rather than a poison on the catalyst surface. Similar to the Rh, the sulfur adsorbs to the active sites on the LZ surface

which engage in synthesis gas production, thus decreasing the rate of reforming and selectivity of the catalyst. However, because there is no continuous decrease in H_2 yield in the presence of DBT, it appears that the effect of sulfur is not cumulative. The reason for this may be that sulfur has a weaker interaction with the LZ surface because it is unable to form a stable sulfide and irreversibly poison the active sites as it did on the $Rh/\gamma\text{-}Al_2O_3$.

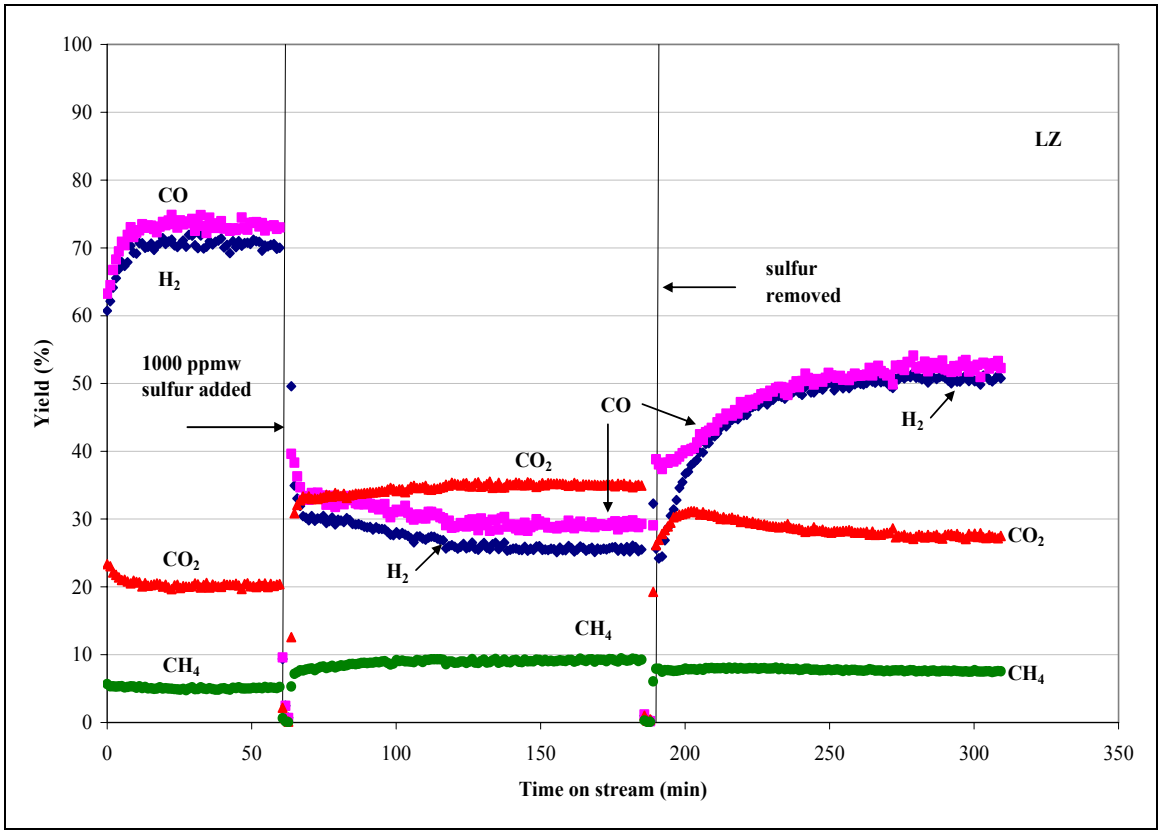

Figure 6.4 Step response plot for LZ after the addition of 1000 ppmw DBT at an O/C=1.2, 0.23 MPa, 900°C and 50,000 scc/$g_{catalyst}$/h. H_2 (♦), CO (■), CO_2 (▲), CH_4 (●).

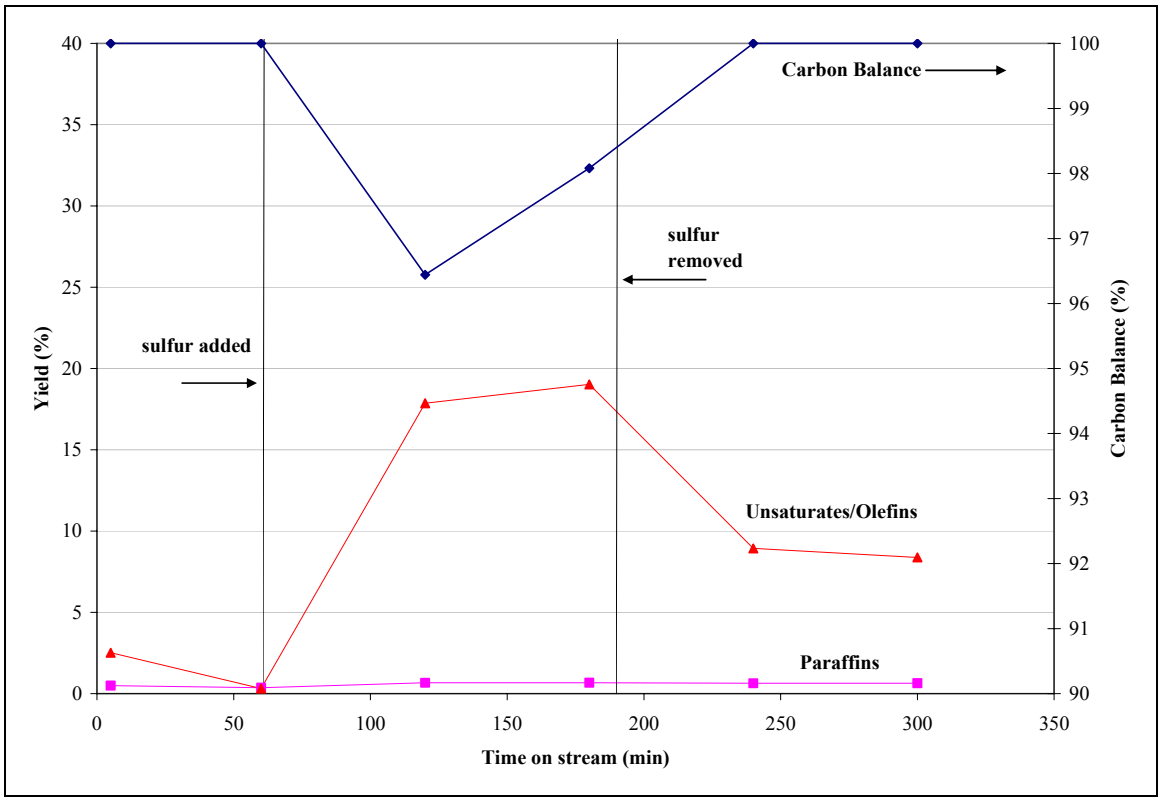

Figure 6.5 Paraffins, unsaturates yields and carbon balance for LZ during the 1000 ppmw DBT/TD experiment at an O/C=1.2, 0.23 MPa, 900°C and 50,000 scc/$g_{catalyst}$/h. Conversion (♦), Olefins (▲), Paraffins (■).

As the sulfur inhibits the reforming reactions at the catalyst surface, gas-phase reactions increase. This is evident by the high yields of olefins and CO_2 that are produced after DBT was introduced. As discussed in Section 5.1.1.1, steam formation is also associated with the increase in gas-phase chemistry, and can most likely be attributed to a significant decrease in the H_2 yield while DBT is present. Just as with the other data in the previous experiments, a calculation was made to determine if the unconverted H and O were in the correct ratio (2/1) to determine whether the formation of steam can exclusively explain the behavior. However, the H/O ratio was calculated to be ~5.3/1 ±2.2, which suggests the formation of steam alone cannot account for the missing H and O.

The selectivity to olefins after the 2 h exposure to DBT is shown in **Table 6.4**, and compared to those formed at the same time over LZ after exposure to MN and Rh/γ-Al_2O_3 after DBT. As seen previously, the LZ and the Rh/γ-Al_2O_3 were deactivated by MN and DBT respectively. However, in Table 6.4, all three experiments show qualitatively similar olefin yields. This shows that although the catalyst may not be deactivated, the sulfur inhibits the reaction rate to the extent that the gas-phase reactions occur at a similar rate to a deactivated catalyst.

Table 6.4 Comparison of C_2-C_6 and benzene yields produced over LZ during CPOX of TD only and after 2 h of 5 wt% MN/TD or 1000 ppmw DBT/TD present in feed. The yields are also compared to C_2-C_6 and benzene yields over Rh/γ-Al_2O_3 after 1000 ppmw DBT/TD experiment. Conditions for all experiments were O/C=1.2, 0.23 MPa, 900°C and 50,000 scc/$g_{catalyst}$/h.

	Rh/γ-Al_2O_3		**LZ**			
	TD only (before DBT)	1000 ppmw DBT	TD only (before MN)	5 wt% MN	TD only (before DBT)	1000 ppmw DBT
Ethane	n.d.[a]	0.7	0.6	0.8	0.4	0.7
Ethylene	n.d.	11.2	1.0	14.7	0.2	13.6
Propylene	n.d.	2.3	0.2	2.4	n.d.	1.8
1,3-Butadiene	n.d.	1.20	n.d.	n.d.	n.d.	n.d.
1-Hexene	n.d.	0.8	n.d.	n.d.	0.8	1.0
Benzene	n.d.	3.4	0.2	3.1	0.1	3.70

[a-] n.d.- not detected

6.1.2.2 Removal of DBT

Following the removal of sulfur, the activity for the LZ pyrochlore partially recovers when the feed is switched back to TD, which indicates that some effects of the DBT are reversible. This behavior differs from the behavior after the removal of MN, which saw almost no activity return (Figure 5.4). During recovery, carbon balance returns to 100% and H_2 and CO yields regain ~20% of their initial values. Olefin yields

also decrease, but remain at levels higher than pre-DBT values. This indicates that a portion of the active sites have been deactivated. Nevertheless, the pyrochlore showed the ability to recover more activity than the Rh, which suggests the sulfur is more weakly adsorbed the pyrochlore surface.

6.1.2.3 Carbon Formation

Table 6.5 shows the addition of DBT leads to 2.7 times less carbon on the LZ surface compared to MN, but still more carbon on the surface compared to CPOX of TD only (0.3 versus 0.8 $g_{carbon}/g_{catalyst}$). Interestingly, the addition of DBT results in almost the same amount of carbon as Rh/γ-Al_2O_3 for the same experiment (0.8 versus 0.9 $g_{carbon}/g_{catalyst}$). The lower quantity of carbon formed, compared to the much larger amount of carbon formed by MN, may be attributed to the reversible adsorption of sulfur on the active sites which are favorable for carbon formation. So, as sulfur consumes active sites, there are fewer sites available for carbon adsorption. Rostrup-Nielsen showed a similar effect using sulfur to passivate a Ni catalyst for steam reforming of methane [95]. He found that the addition of sulfur prevented coking by blocking the active sites [95].

Figure 6.5 presents the TPO profiles after each of the three experiments performed on the LZ. The addition of DBT produces less carbon on the LZ compared to MN. A TPO profile for the LZ exposed to DBT shows 3 peaks, which suggests that there are 3 sites on the surface that accumulate carbon. However, the specific nature of these sites is not certain. It is likely that carbon is also formed on these sites during the MN experiment; however the peaks are obscured by the greater amount of carbon present.

Table 6.5 Amount of carbon formed on LZ pyrochlore after CPOX of TD only, 5 wt% MN/TD and 1000 ppmw DBT/TD respectively; 900°C, 50000 scc/$g_{catalyst}$/h. Results are compared to carbon formed on Rh/γ-Al_2O_3 after 1000 ppmw DBT/TD experiment; 900°C, 50000 scc/$g_{catalyst}$/h.

Catalyst	Carbon ($g_{carbon}/g_{catalyst}$)
LZ (TD only)	0.30
LZ (After 5 wt% MN/TD)	2.06
LZ (After 1000 ppmw DBT/TD)	0.8
Rh/γ-Al_2O_3 (After1000 ppmw DBT/TD)	0.90

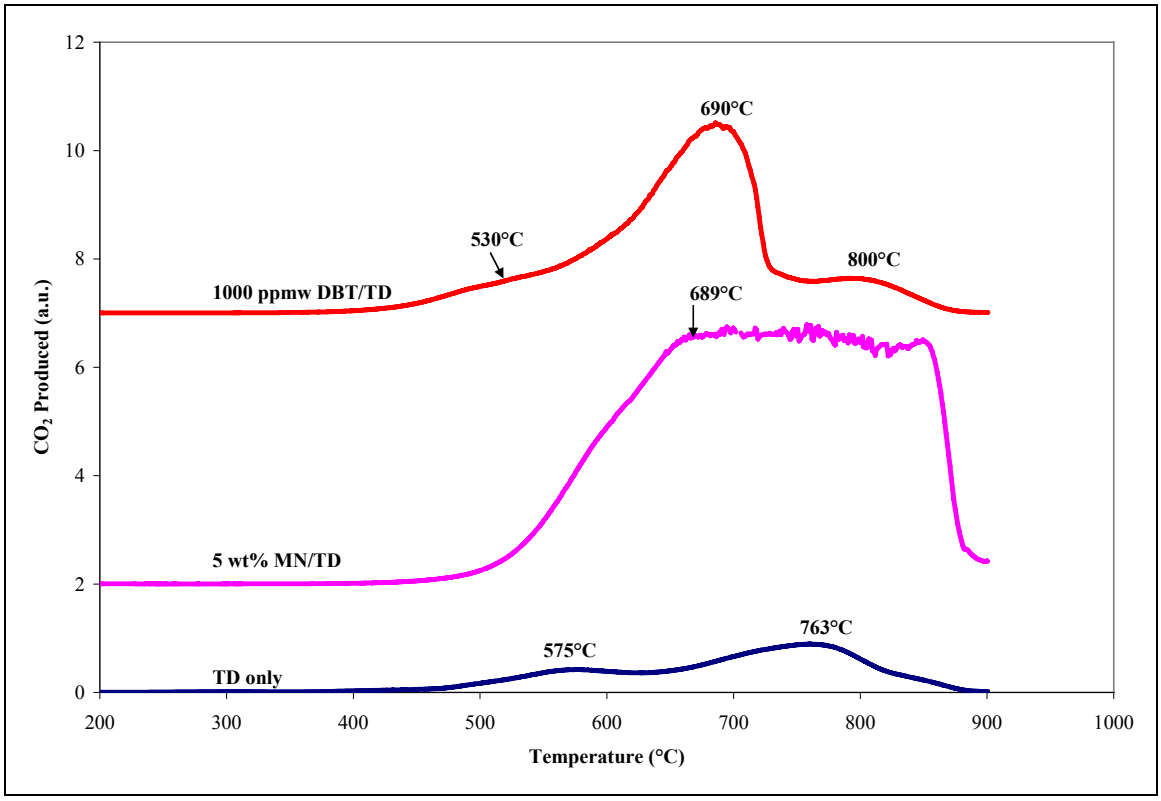

Figure 6.6 TPO profiles for LZ after CPOX of 1000 ppmw DBT/ TD, 5-wt% MN/TD and TD only.

6.1.3 LRZ

6.1.3.1 Effect of DBT on Synthesis Gas Yield

The substitution of Rh metal into the pyrochlore structure decreases the deactivation of the Rh metal by sulfur. The effects of 1000 ppmw DBT on the activity

and selectivity of LRZ, shown in **Figures 6.7 and 6.8**, are qualitatively similar to the addition of MN in Section 5.1.3.1. Over the 2-h period of time during which DBT is present in the feed, H_2 and CO yields both decrease continuously at the same rate as they did during MN experiment, 0.18% H_2 or CO/min, with an H_2/CO ratio < 1. Again it is uncertain, over the time scale of this experiment, whether sulfur will irreversibly poison the catalyst or only kinetically inhibit the reaction rate and the yields would eventually stabilize as they did for the LZ. Yet, despite this decline in activity, the carbon balance remains 100% throughout the 2 h. Olefin and CO_2 yields increase as the selectivity to synthesis gas declines, suggesting more gas-phase reactions are occurring in the system. **Table 6.4** shows that approximately the same amount of, and selectivity to, olefins is similar over LRZ either in the presence of MN or DBT, and is much less than those produced in the presence of DBT over LZ and Rh/γ-Al_2O_3.

Again, as the gas-phase chemistry increases, it is presumed that steam formation begins to consume some of the H_2 yield. A mass balance over H and O containing shows an H/O ratio of 1.8 ±0.4 over the time DBT is present, which is consistent with the formation of steam alone as a reaction product containing H and O.

The catalytic behavior seen for LRZ suggests incorporating rhodium into the structure decreases the rate of deactivation by sulfur. Distributing the metal throughout the structure likely decreases the bond strength between Rh metal and sulfur, which was assumed to deactivate the Rh metal on the Rh/γ-Al_2O_3. The deactivation of rhodium is not completely avoided, however, as the data shows that activity continues to decline with time over the length of this experiment.

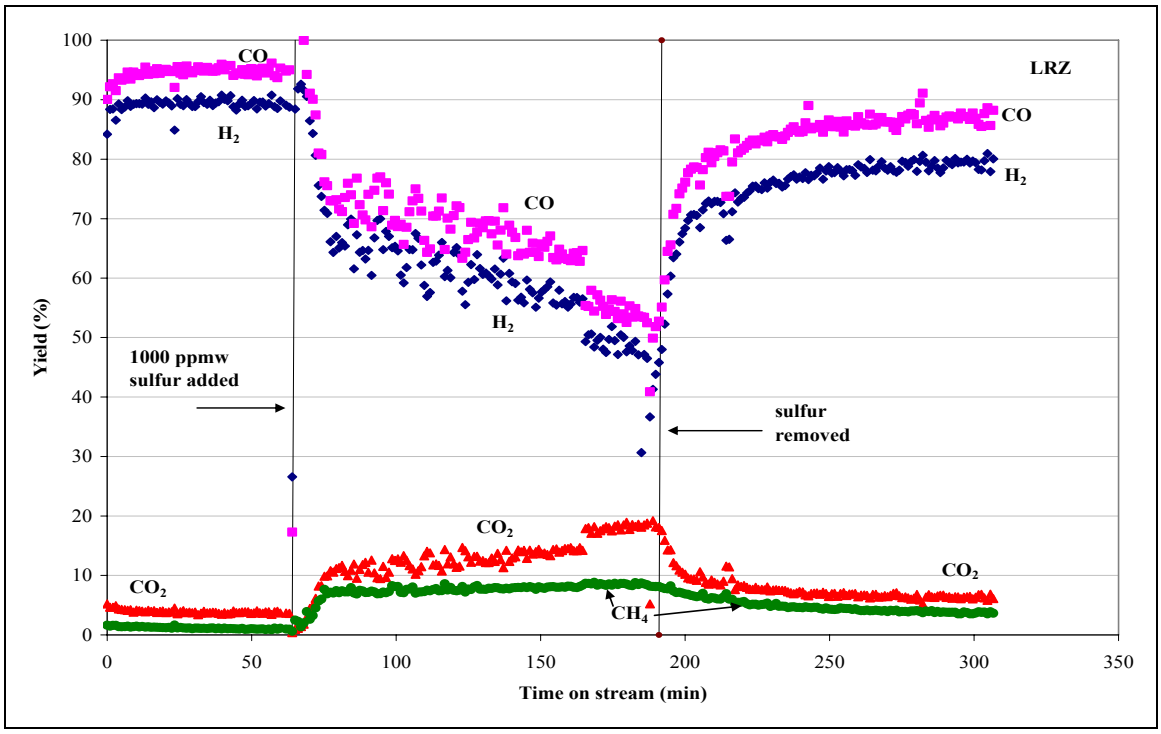

Figure 6.7 Step response plot for LRZ after the addition of 1000 ppmw DBT at an O/C=1.2, 0.23 MPa, 900°C and 50,000 scc/$g_{catalyst}$/h. H_2 (♦), CO (■), CO_2 (▲), CH_4 (●).

6.1.3.2 Removal of DBT

After the DBT is removed from the feed, synthesis gas yields recover to ~90% of their pre-DBT levels. The return of catalytic activity is coupled with a decrease in gas-phase reactions (that form olefins) to near pre-DBT yields, as seen in Figure 6.8. The recovery suggests that metal incorporation makes the active Rh sites less prone to irreversible poisoning by the sulfur. However, similar to the effects of MN, activity is unable to fully recover, which indicates that some of the active sites have been irreversibly poisoned. It is unclear though, as with the Rh/γ-Al_2O_3 or LZ, if the deactivation is due to sulfur or carbon formation.

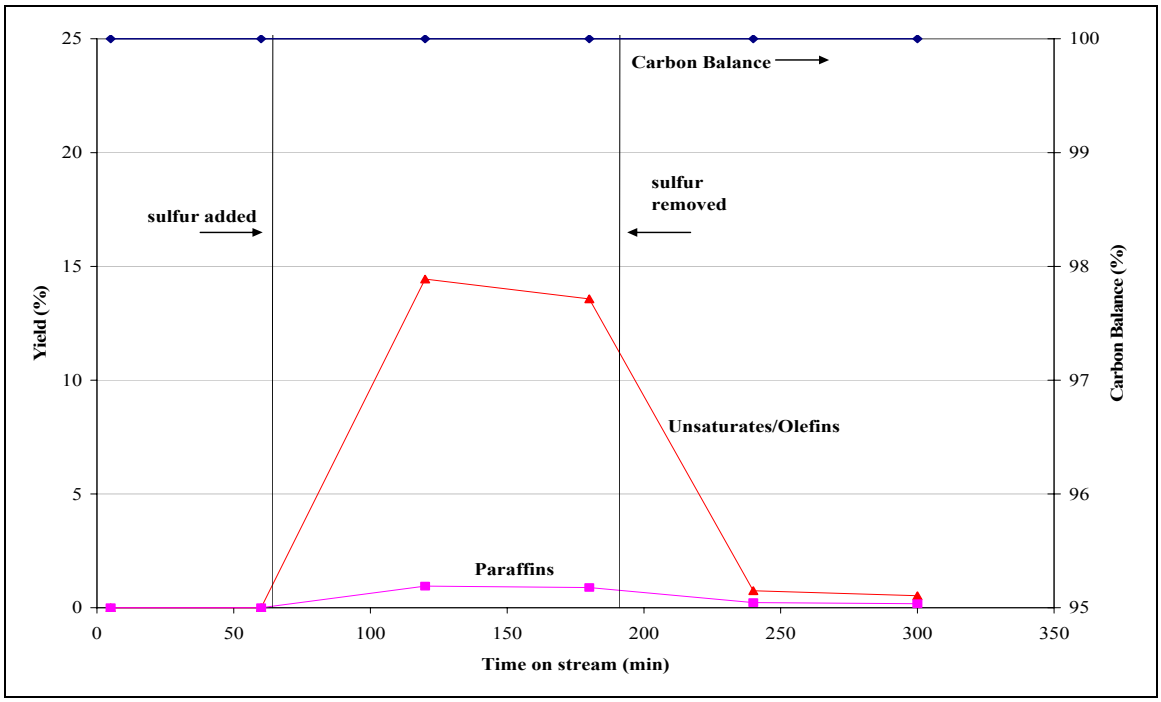

Figure 6.8 Paraffins, unsaturates yields and carbon balance for LRZ during the 1000 ppmw DBT/TD experiment at an O/C=1.2, 0.23 MPa, 900°C and 50,000 scc/$g_{catalyst}$/h. Conversion (♦), Olefins (▲), Paraffins (■).

Table 6.6 Comparison of C_2-C_6 and benzene yields produced over LRZ during CPOX of TD only (before MN or DBT was added) and after 2 h of 5 wt% MN/TD or 1000 ppmw DBT/TD present in feed. The yields are also compared to C_2-C_6 and benzene yields produced over Rh/γ-Al_2O_3 and LZ after 2 h 1000 ppmw DBT/TD experiment. Conditions for all experiments were O/C=1.2, 0.23 MPa, 900°C and 50,000 scc/$g_{catalyst}$/h.

	Rh/γ-Al_2O_3		**LZ**		**LRZ**			
	TD only (before DBT)	1000 ppmw DBT	TD only (before DBT)	1000 ppmw DBT	TD only (before MN)	5 wt% MN	TD only (before DBT)	1000 ppmw DBT
Ethane	n.d.[a]	0.7	0.4	0.7	n.d.	0.8	n.d.	0.9
Ethylene	n.d.	11.2	0.2	13.6	n.d.	8.8	n.d.	8.9
Propylene	n.d.	2.3	n.d.	1.8	n.d.	1.4	n.d.	1.3
1,3-Butadiene	n.d.	1.20	n.d.	n.d.	n.d.	n.d.	n.d.	n.d.
1-Hexene	n.d.	0.8	0.8	1.0	n.d.	n.d.	n.d.	n.d.
Benzene	n.d.	3.4	0.1	3.70	n.d.	2.5	n.d.	3.4

[a-] n.d.- not detected

6.1.3.3 Carbon Formation

The carbon accumulated on LRZ during the CPOX of 1000ppmw DBT/TD is shown in **Table 6.7** and is compared to that formed over LRZ as a result of MN, as well on Rh/γ-Al_2O_3 and LZ as a result of DBT. As can be seen, the presence of 1000ppmw sulfur results in less carbon over LRZ than 5 wt% MN (0.86 versus 1.20 $g_{carbon}/g_{catalyst}$). This can also likely be attributed to the sulfur poisoning/reversibly adsorbing to the active sites that also accumulate carbon. Yet, surprisingly, this value (0.86 $g_{carbon}/g_{catalyst}$) is comparable to the amount of carbon produced over Rh/γ-Al_2O_3 (0.90 $g_{carbon}/g_{catalyst}$) and LZ (0.80 $g_{carbon}/g_{catalyst}$), which both saw an instantaneous and significant decline in activity due to the DBT, and limited recovery. Despite the deactivation, the LRZ is able to recover most of its activity, which indicates that the carbon formed did not hinder recovery. This is further evidence that the distributed active metal sites are less susceptible to carbon formation and the carbon that is induced by the DBT must also form indiscriminately over the surface.

Due to this behavior of carbon adsorption, the carbon burned off after this experiment, **Figure 6.9**, is qualitatively identical to the carbon formed on LRZ after the MN experiment. In fact all four profiles shown in the figure are qualitatively similar. However, this is not surprising as the carbon burned off the LZ pyrochlore and Rh/γ-Al_2O_3 after the CPOX of TD only (Figure 4.6) showed similar reactivity. Still, the profile for LRZ shows low and high temperature shoulders at 546°C, and 787°C respectively, along with a larger peak at 696°C. Judging by temperature and shape of the peaks, it appears that they are all associated with the pyrochlore structure, since the reactivity of the adsorbed carbon is almost identical to the LZ.

Table 6.7 Amount of carbon formed on LRZ pyrochlore after 5 wt% MN/TD and 1000 ppmw DBT/TD respectively; 900°C, 50000 scc/$g_{catalyst}$/h. Results are compared to carbon formed on Rh/γ-Al_2O_3 and LZ after 1000 ppmw DBT/TD experiment; 900°C, 50000 scc/$g_{catalyst}$/h.

Catalyst	Carbon ($g_{carbon}/g_{catalyst}$)
LRZ (After 1000 ppmw DBT/TD)	0.86
LRZ (After 5 wt% MN/TD)	1.20
LZ (After 1000 ppmw DBT/TD)	0.8
Rh/γ-Al_2O_3 (After 1000 ppmw DBT/TD)	0.9

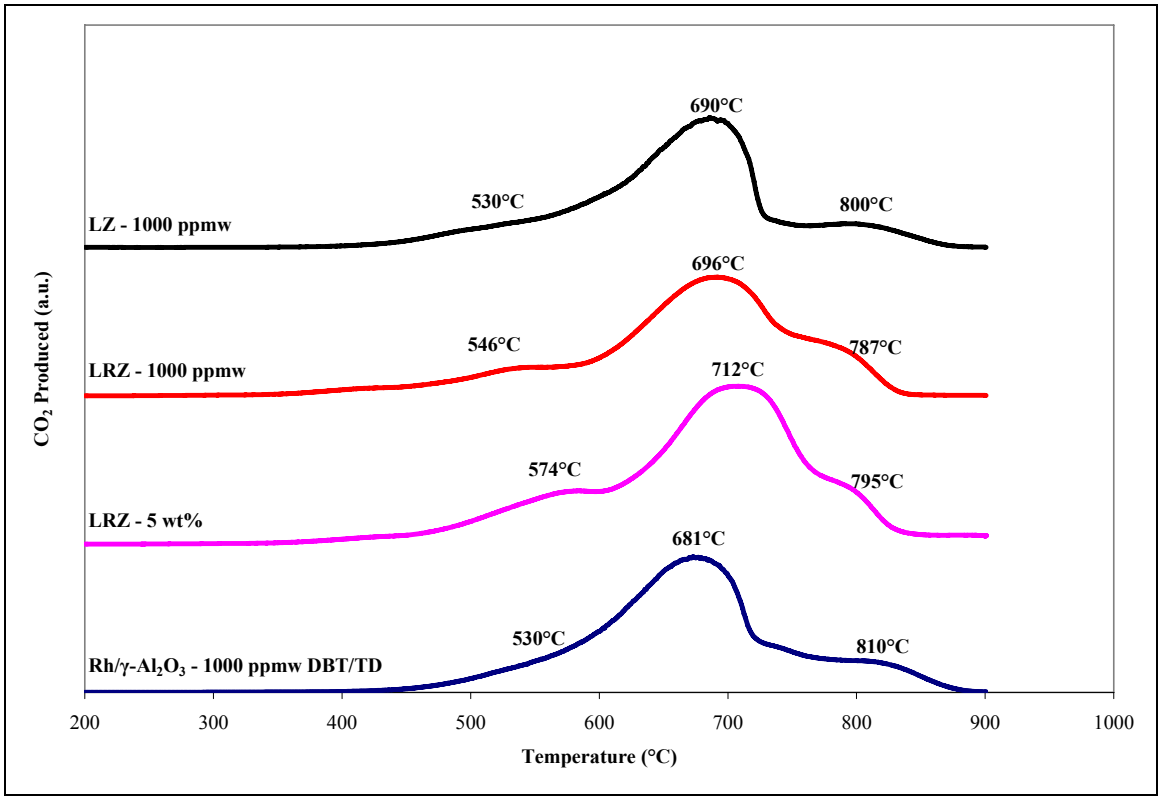

Figure 6.9 TPO profiles from LRZ after CPOX of 1000 ppmw DBT/TD and 5 wt% MN/TD. TPO profiles are compared to LZ and Rh/γ-Al_2O_3 after CPOX of 5 wt% MN + 1000 ppmw DBT/TD.

6.1.4 LSRZ

6.1.4.1 Effect of DBT on Synthesis Gas Yield

The substitution of Sr^{2+} into the pyrochlore structure stabilizes the reforming behavior in the presence of 1000 ppmw DBT. Like the previous experiments on the

Rh/γ-Al_2O_3 and LRZ catalysts, **Figure 6.10** and **Figure 6.11** show the effects of sulfur have qualitatively similar effects on LSRZ to presence of MN in Section 5.1.4. The H_2 and CO yields both drop to stationary levels and remain constant over the 2-h, while the carbon balance drops only slightly but remains > 94%. The change in selectivity is accompanied by an increase in olefins and CO_2. Compared to the effects of MN, the effects of sulfur on LSRZ resulted in about twice the olefin content, as seen in **Table 6.8**. But, compared to the other 3 catalysts, the extent of olefin production in the presence of DBT was significantly lower over the LSRZ, although all 3 catalysts have the same olefin selectivity.

Also, as seen before, steam formation is a likely product during the onset of gas-phase chemistry. The mass balance over H and O atoms over the 2 h DBT was present shows an H/O ratio of 1.1 ± 1.5. This again indicates that as the selectivity changes to gas-phase chemistry, steam is likely responsible for decrease in H_2 yield and is the only undetected product consisting of H and O.

Table 6.8 Comparison of C_2-C_6 and benzene yields produced over LSRZ during CPOX of TD only (before MN or DBT was added) and after 2 h of 5 wt% MN/TD or 1000 ppmw DBT/TD present in feed. The yields are also compared to C_2-C_6 and benzene yields produced over Rh/γ-Al_2O_3, LZ and LRZ after 2 h 1000 ppmw DBT/TD experiment. Conditions for all experiments were O/C=1.2, 0.23 MPa, 900°C and 50,000 scc/$g_{catalyst}$/h.

	Rh/γ-Al_2O_3		**LZ**		**LRZ**		**LSRZ**			
	TD only	1000 ppmw sulfur	TD only	1000 ppmw sulfur	TD only	1000 ppmw sulfur	TD only	5 wt% MN	TD only	1000 ppmw sulfur
Ethane	0.1	0.7	0.6	0.7	n.d.	0.9	n.d.	0.5	n.d.	0.7
Ethylene	0.1	11.0	1.0	13.6	n.d.	9.0	n.d.	1.6	n.d.	4.4
Propylene	n.d.	2.3	0.2	1.8	n.d.	1.3	n.d.	0.2	n.d.	0.5
1,3-Butadiene	n.d.	1.2	n.d.	n.d.	n.d.	n.d.	n.d.	n.d.	n.d.	n.d.
1-Hexene	n.d.	0.8	n.d.	0.9	n.d.	n.d.	n.d.	n.d.	n.d.	n.d.
Benzene	n.d.	3.4	0.2	3.7	n.d.	3.4	n.d.	0.8	n.d.	1.8

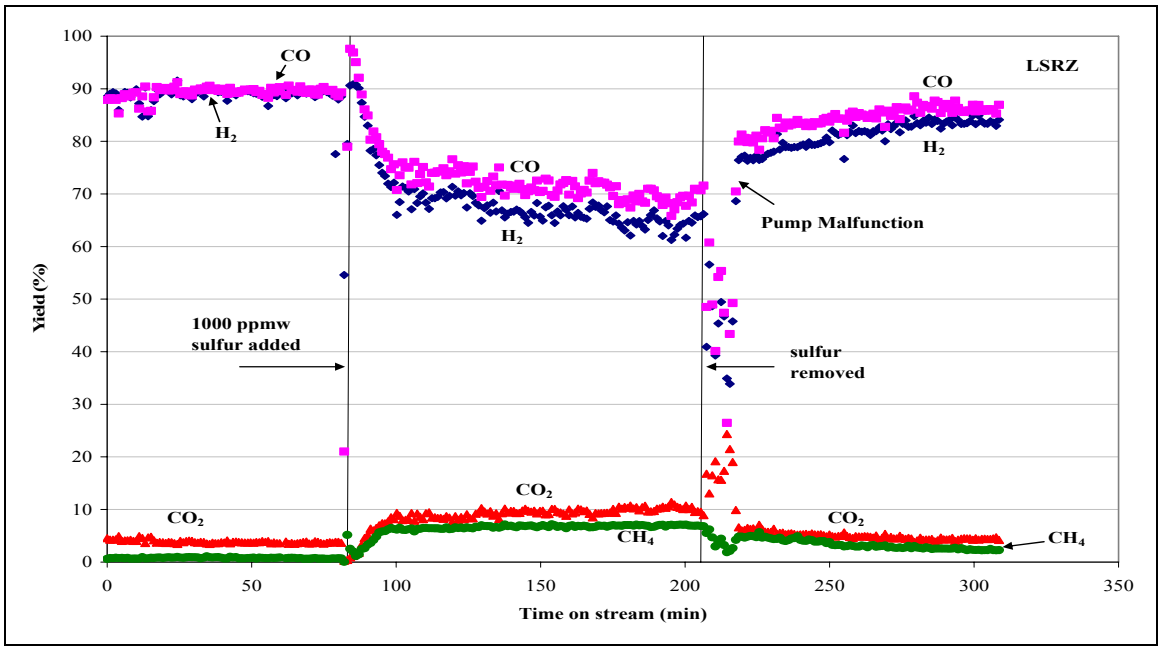

Figure 6.10 Step response plot for LSRZ after the addition of 1000 ppmw DBT at an O/C=1.2, 0.23 MPa, 900°C and 50,000 scc/$g_{catalyst}$/h. H_2 (♦), CO (■), CO_2 (▲), CH_4 (●).

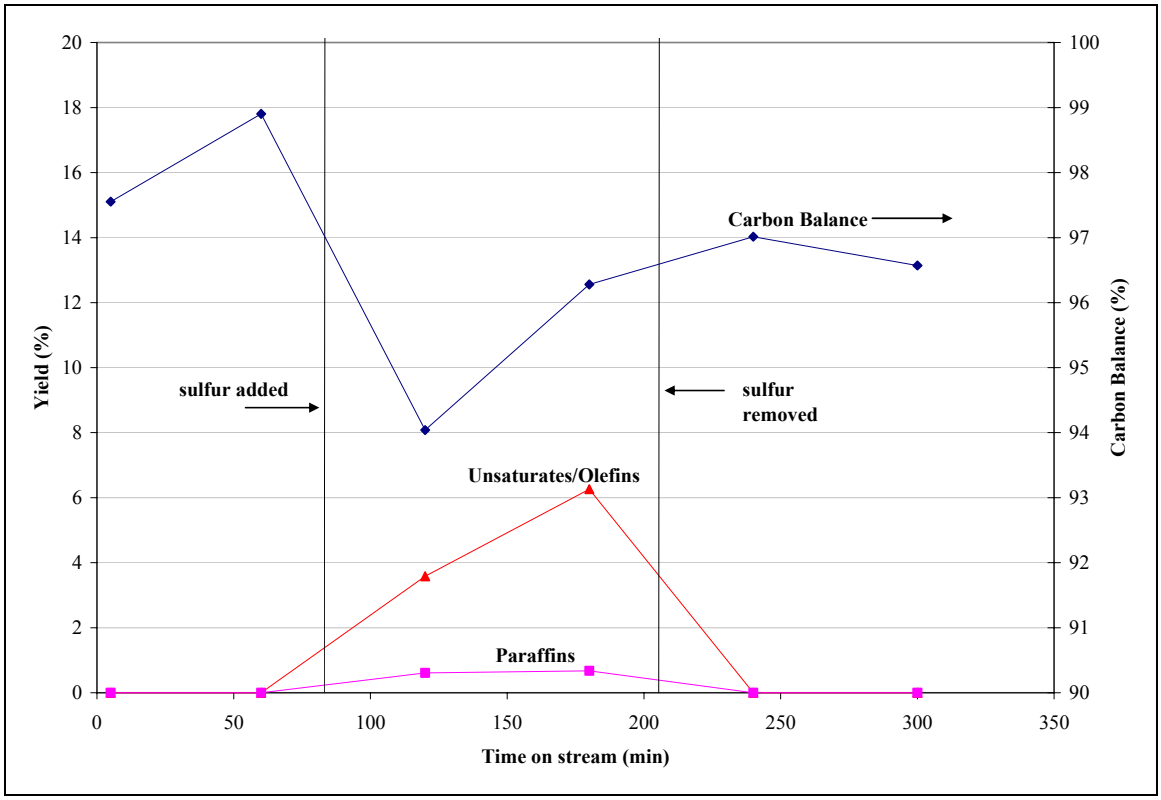

Figure 6.11 Paraffins, unsaturates yields and carbon balance for LSRZ during the CPOX 1000 ppmw DBT/TD at an O/C=1.2, 0.23 MPa, 900°C and 50,000 scc/$g_{catalyst}$/h. Conversion (♦), Olefins (▲), Paraffins (■).

This drop in synthesis gas yields to stationary levels suggests the sulfur kinetically inhibits the reforming reaction. However, the LSRZ catalyst shows lower olefin yields than LZ (which was also kinetically inhibited by DBT), possibly because mobile lattice oxygen may lower the rate of inhibition. As seen in Chapters 4 and 5, the substitution of Sr^{2+} for La^{3+} may create oxygen vacancies in the pyrochlore lattice which likely permit the oxygen anions in the structure to become mobile at the high reaction temperatures. It is likely the localized oxygen that is partially coordinated at the surface reacts with the adsorbed sulfur, as well as carbon formed due to the presence of sulfur, thus limiting the rate of consumption of active sites. Then the oxygen may be replenished by steam or O_2 in the feed. It is unclear if the adsorbed sulfur is converted to SO_2 or H_2S.

6.1.4.2 Removal of DBT

After the feed is switched back to TD, synthesis gas yields, olefin yields and conversion all return close to pre-DBT levels, within ~1 h. The ability to recover initial activity shows that, although sulfur decreases the reforming rate on the surface, it appears that the oxygen-ion conductivity prevents irreversible poisoning of the active sites. Thus, similar to MN, the DBT appears to act as a kinetic inhibitor over the time scale of the experiment.

6.1.4.3 Carbon Formation

The addition of Sr and Rh to the pyrochlore significantly decreases the tendency for carbon formation due to sulfur. Similar to the LZ and LRZ, **Table 6.9** shows the amount of carbon formed on LSRZ in the presence of DBT is almost 2.2 times less compared to that formed over during the MN experiment. Like sections 6.1.3.3 and

6.1.2.3, this can also likely be attributed to the sulfur reversibly adsorbing to the active sites that also accumulate carbon. This amount of carbon is also significantly lower compared to the carbon produced over the other 3 catalysts in the presence of DBT (0.3 versus 0.8-0.9 $g_{carbon}/g_{catalyst}$). This is to be expected, as LSRZ demonstrated the lowest carbon formation in Chapters 4 and 5. The result can be attributed to the reaction between adsorbed carbon and mobile lattice oxygen that results from the substitution of Sr^{2+} into the A-site that was discussed earlier in Section 4.2.5.

Table 6.9 Amount of carbon formed on LSRZ pyrochlore after 5 wt% MN/TD and 1000 ppmw DBT/TD respectively; 900°C, 50000 scc/$g_{catalyst}$/h. Results are compared to carbon formed on Rh/γ-Al_2O_3, LZ and LRZ after 1000 ppmw DBT/TD experiment; 900°C, 50000 scc/$g_{catalyst}$/h.

Catalyst	Carbon ($g_{carbon}/g_{catalyst}$)
LSRZ (After 1000 ppmw DBT/TD)	0.3
LSRZ (After 5 wt% MN/TD)	0.67
LRZ (After 1000 ppmw DBT/TD)	0.86
LZ (After 1000 ppmw DBT/TD)	0.8
Rh/γ-Al_2O_3 (After 1000 ppmw DBT/TD)	0.9

The reactivity of the carbon formed on LSRZ during the CPOX of 1000 ppmw DBT/TD is shown in **Figure 6.12**. In general, the carbon adsorbed onto the LSRZ is similar in reactivity to the LZ and LRZ, as the profile shows the high temperature pyrochlore peak at 688°C and subsequent shoulder at 797°C. However, the presence of sulfur appears to inhibit the formation of the more reactive carbon that was oxidized at 576°C from the MN profile.

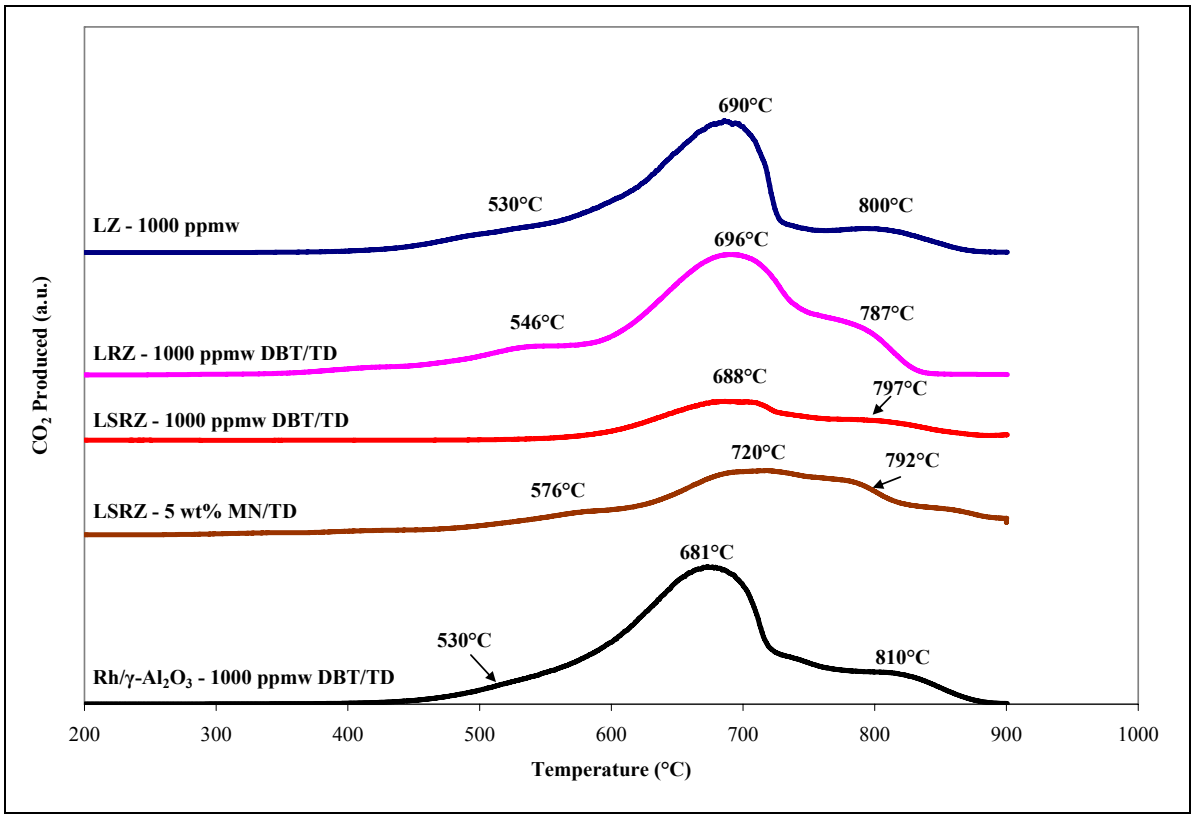

Figure 6.12 TPO profiles from LSRZ after CPOX of 1000 ppmw DBT/TD and 5 wt% MN/TD. TPO profiles are compared to LRZ, LZ and Rh/γ-Al_2O_3 after CPOX of 5 wt% MN + 1000 ppmw DBT/TD.

Chapter 7. Results and Discussion: Effects of Polynuclear Aromatics and Sulfur

The previous two chapters investigated the individual effects of polyaromatics and high levels sulfur on the synthesis gas yield for four catalysts. However, logistic fuels are a mixture of various paraffins, aromatics, and organosulfur compounds and in reforming these fuels the catalysts would be exposed to the compounds together. Therefore, this chapter will examine the CPOX of a simulated diesel fuel mixture consisting of 5 wt-% MN and 1000 ppmw sulfur in TD.

Similar to Chapters 5 and 6, the results indicate that the substitution of Rh into the pyrochlore structure avoids the instantaneous deactivation and carbon formation that occurs on the supported Rh/γ-Al_2O_3 from the MN and DBT together. Then, additional substitution of Sr with Rh is able to limit the effects of MN and DBT to a kinetic inhibition and maintain steady CPOX yields over 2-h with minimal carbon formation.

7.1 Reforming Results: 5 wt-% MN and 1000 ppmw Sulfur

As in Chapters 5 and 6, the CPOX of TD only was performed to establish a baseline for initial catalytic activity. The results shown in **Table 7.1** are consistent with the results reported earlier. Each Rh catalyst produces H_2 and CO yields close to equilibrium values (see Table 4.1), and the unsubstituted pyrochlore shows the lowest yields. After 1-h, 5 wt% MN and 1000ppmw DBT are both added to the feed. As expected, the combination of MN and DBT adversely affect the H_2 and CO yields as well as the amount of carbon formed for each catalyst. However, the extent of these effects varied for each catalyst.

Table 7.1 Synthesis gas yields for each catalyst during the CPOX of TD after 1 h time on stream at an O/C=1.2, 0.23 MPa, 900°C and 50,000 scc/$g_{catalyst}$/h.

	$Rh/\gamma\text{-}Al_2O_3$	LZ	LRZ	LSRZ
H_2 Yield (%)	85.0	69.0	86.0	84.0
CO Yield (%)	79.0	71.0	87.0	84.0

7.1.1 $Rh/\gamma\text{-}Al_2O_3$

7.1.1.1 Effect of MN and DBT on Synthesis Gas Yield

The effects of the addition of 5 wt% MN and 1000 ppmw DBT on the catalytic activity and conversion of $Rh/\gamma\text{-}Al_2O_3$ are presented in **Figure 7.1** and **7.2**. As can be seen, the presence of MN and DBT together decreases the catalyst yields in a manner consistent with the addition of either MN or DBT alone in Sections 5.1.1.1, and 6.1.1.1. While both contaminants are in the feed, the H_2 yield decreases continuously, as the CO yield stabilizes. The decrease in synthesis gas yields is then accompanied by an increase in CO_2 and olefins as reaction products. The distribution of olefin products is consistent for each of the experiments over the $Rh/\gamma\text{-}Al_2O_3$, as shown in **Table 7.2**. The carbon balance also drops over the 2-h, but remains > 94%.

The decrease in synthesis gas yields can be attributed to the combined effects of MN and DBT adsorbing to the active sites of Rh catalyst and reducing surface chemistry as discussed in Sections 5.1.1.1 and 6.1.1.1. Interestingly, however, the combined effects are only as detrimental to catalyst activity as the individual contaminants themselves. For example, the quantity of olefins produced (Figure 7.2) is quantitatively similar to those produced in the presence of MN only (Figure 5.2). Also, the rate of decrease in the H_2 yield during this experiment is faster compared to DBT, but slower than MN. A regression analysis shows that in the presence of DBT and MN, H_2 yield decreases at a

rate of 0.16%/min. Over the same time period, 2-h, the H_2 yield decreases at a rate of 0.19%/min due to MN only and 0.14%/min as a result of DBT. This may be explained by the fact that sulfur and MN both compete for the same sites, and in doing so deactivate the catalyst at a similar rate.

As discussed earlier in Sections 5.1.1.1 and 6.1.1.1, steam formation becomes favorable as the reactions in the gas-phase increase and may be responsible for the continuous drop in H_2 yield. A calculation was again made to verify if the un-reacted H and O atoms were in the correct ratio, 2/1, to show an increase in steam formation while the contaminants are in the feed. However, the mass balance showed atomic H/O ratio was 4.2/1 ±1.5, which indicates steam is likely not the only product containing H and O atoms.

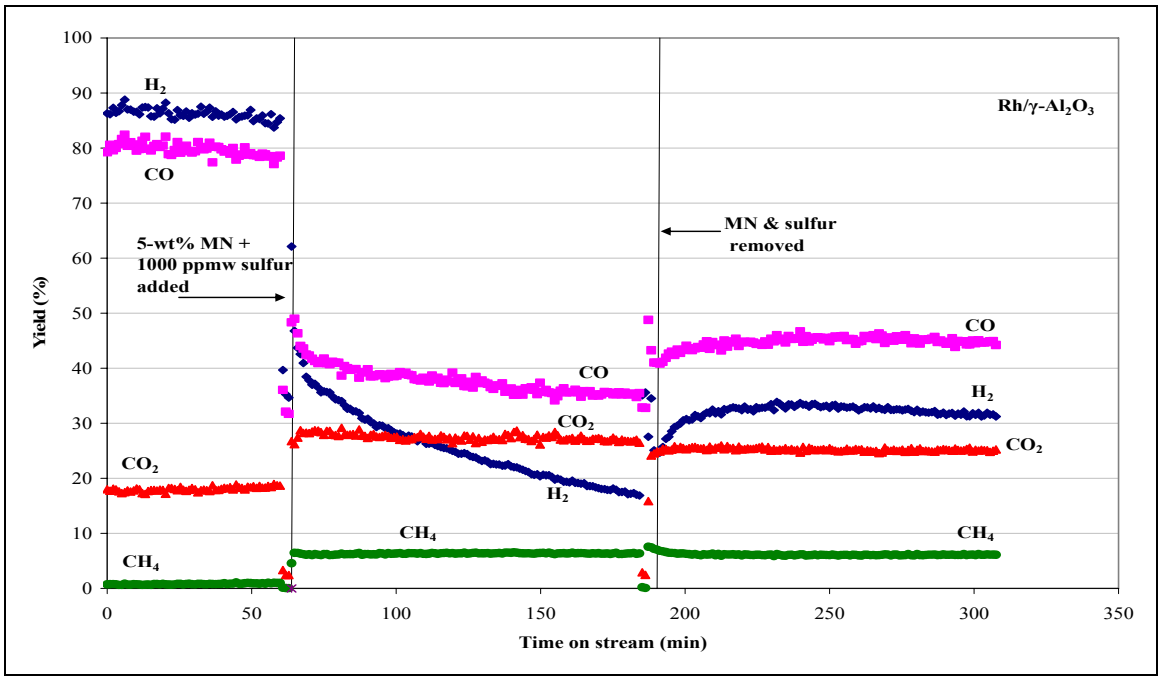

Figure 7.1 Step response plot for Rh/γ-Al_2O_3 after the addition of 5 wt% MN + 1000 ppmw DBT at an O/C=1.2, 0.23 MPa, 900°C and 50,000 scc/$g_{catalyst}$/h. H_2 (♦), CO (■), CO_2 (▲), CH_4 (●).

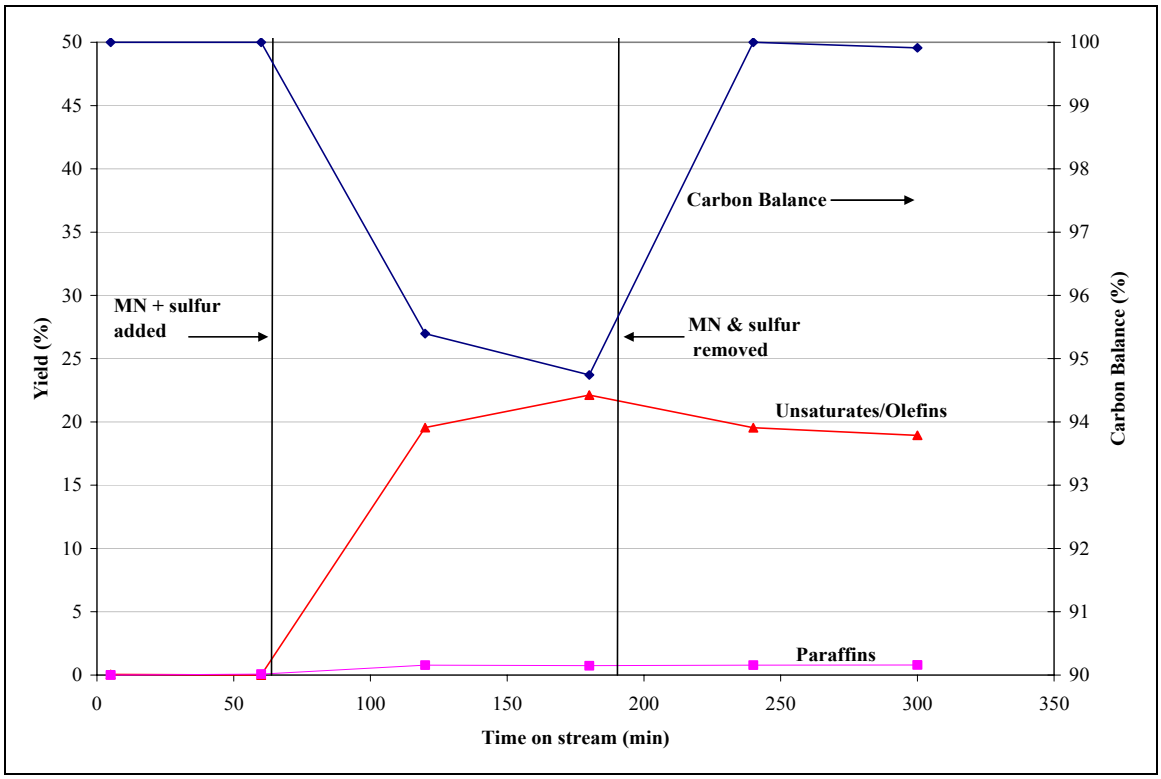

Figure 7.2 Paraffins, unsaturates yields and conversion for Rh/γ-Al_2O_3 during the CPOX of 5wt% MN + 1000 ppmw DBT in TD experiment at an O/C=1.2, 0.23 MPa, 900°C and 50,000 scc/$g_{catalyst}$/h. Conversion (♦), Olefins (▲), Paraffins (■).

Table 7.2 Comparison of C_2-C_6 and benzene yields formed between blank reactor and Rh/γ-Al_2O_3. Rh/γ-Al_2O_3 yields were produced after CPOX of TD only (before MN, DBT or both were added) and after 2 hours of 5 wt% MN, 1000 ppmw DBT or both in TD at O/C=1.2, 0.23 MPa, 900°C and 50,000 scc/$g_{catalyst}$/h.

	Blank	**Rh/γ-Al_2O_3**					
	TD only	TD only (before MN)	5 wt% MN	TD only (before DBT)	1000 ppmw DBT	TD only (before MN & DBT)	5 wt% MN & 1000 ppmw DBT
Ethane	0.70	0.1	0.8	n.d.	0.7	0.10	0.7
Ethylene	16.30	0.1	13.5	n.d.	11.2	n.d.	13.2
Propylene	17.0	n.d.	2.1	n.d.	2.3	n.d.	2.9
1,3-Butadiene	1.0	n.d.	1.5	n.d.	1.20	n.d.	1.7
1-Hexene	n.d.[a]	n.d.	1.0	n.d.	0.8	n.d.	0.8
Benzene	3.90	n.d.	3.8	n.d.	3.4	n.d.	3.4

[a-] n.d..- not detected

7.1.1.2 Removal of MN and DBT

As expected, once the feed is switched back to TD only, catalytic activity is unable to return to initial levels for the Rh/γ-Al_2O_3. The carbon balance returns to 100%, but the H_2 and CO yields remain much lower compared to initial values. They are also produced at an H_2/CO ratio of <<1 compared to a ratio that was >1 before MN and DBT were introduced. Olefin and CO_2 yields remain high during the 2-h recovery period, indicating the surface chemistry of the catalyst has been deactivated and most of the reactions are occurring the gas-phase. As seen in Sections 5.1.1 and 6.1.1, it is likely the deactivation is a result of the coverage of active sites by carbon.

7.1.1.3 Carbon Formation

The presence of MN and DBT together produces the greatest amount of carbon on the surface of the Rh/γ-Al_2O_3 compared to the other experiments (**Table 7.3**). Similar to the Sections 5.1.1.3 and 6.1.1.3, it is likely the accumulation of carbon on the active sites is responsible for the inability to recover activity. During recovery in the CPOX of TD only (Figure 7.1 and 7.2), the catalyst produces the lowest H_2/CO yield and consequently highest olefin yields compared to the recovery time during the other 2 experiments. This is indicative that the MN and DBT together leads to a greater amount of carbon on the active metal sites.

Figure 7.3 shows that the reactivity of the adsorbed carbon is consistent with the previous CPOX experiments involving only MN and DBT in Sections 5.1.1.3 and 6.1.1.3 respectively. Like these previous experiments, the resulting TPO profile shows a broad low temperature shoulder at ~524°C which is then overlapped by a large peak at ~692°C

indicating more carbon has accumulated on the Rh metal and metal-support interface than during the CPOX of TD only. These peaks also appear to be larger compared to those for DBT and MN experiments, which further proves more carbon is formed on the active metal sites may be responsible for the lower catalytic activity after the contaminates were removed. Then all profiles have roughly the same high temperature peak between 785-810°C which is associated with the carbon deposited on the alumina support.

Table 7.3 Amount of carbon formed on Rh/γ-Al_2O_3 after CPOX of TD only, 5 wt% MN/TD, 1000 ppmw DBT/TD and 5 wt% MN +1000 ppmw DBT/TD experiments; 900°C, 50000 scc/$g_{catalyst}$/h.

	Carbon ($g_{carbon}/g_{catalyst}$)
TD Only	0.27
5 wt% MN/TD	0.80
1000 ppmw DBT/TD	0.90
5 wt% MN +1000 ppmw DBT/TD	1.10

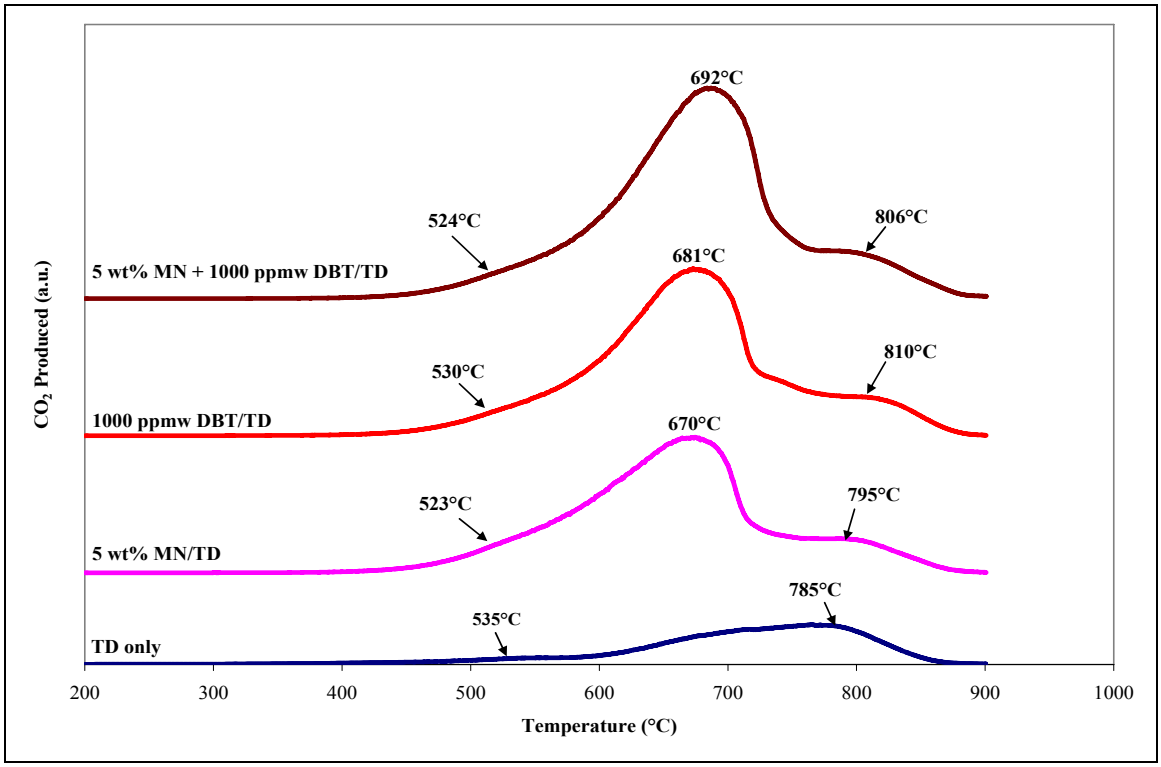

Figure 7.3 TPO profiles for Rh/γ-Al_2O_3 after CPOX of 5 wt% MN + 1000 ppmw DBT/ TD, 1000 ppmw DBT/TD, 5-wt% MN/TD and TD only.

7.1.2 LZ

7.1.2.1 Effect of MN and DBT on Synthesis Gas Yield

The effects of the surrogate diesel fuel mixture on the activity and selectivity of the un-doped pyrochlore (LZ) are shown in **Figures 7.4** and **7.5**. After the mixture of MN and DBT is introduced, the catalyst is deactivated immediately. There is a significant drop in the carbon balance (~13% drop shown in Figure 7.5) and the H_2 and CO yields decrease to levels seen during the CPOX of TD only in the blank reactor in Figure 4.2. Again, as the catalyst activity is deactivated, gas-phase chemistry (olefins) increases in the system. While the reactions are taking place in the gas-phase, **Table 7.4** shows that over the 2-h period, the higher order hydrocarbon reaction products are consistent with the previous experiments.

The effects on activity and selectivity of the LZ catalyst during this experiment are qualitatively similar to the CPOX of 5 wt% MN/TD only, which indicates the MN is mainly responsible for the deactivation. However, unlike Section 6.1.1.1, the presence of sulfur is unable to inhibit the active sites and block carbon formation. Rather, the presence of MN appears to be overwhelming at the surface and actually appears to have a faster rate of carbon formation in the presence of sulfur, as deactivation occurs much more quickly in the presence of both than just MN.

Similar to the previous experiments, the formation of high olefin yields indicates steam is likely occurring in place of the H_2. The mass balance was able to account for steam formation as the ratio of unaccounted for H and O atoms produced a ratio of 2.3/1 ±0.68 while both MN and DBT were present.

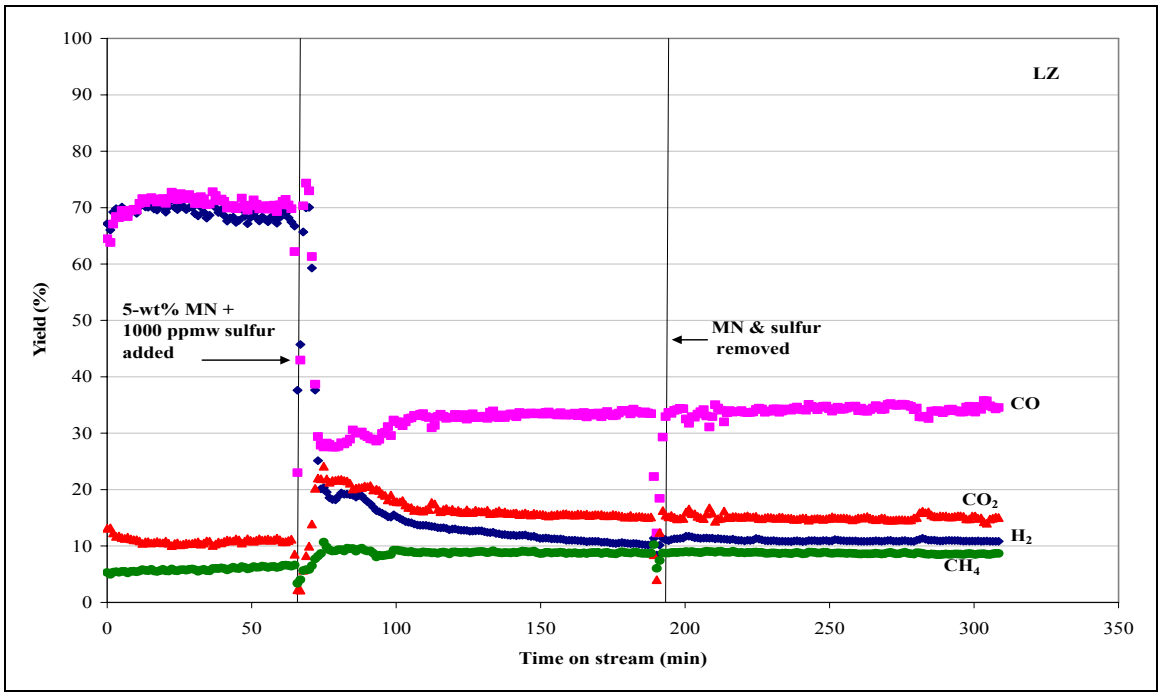

Figure 7.4 Step response plot for LZ after the addition of 5 wt% MN + 1000 ppmw DBT at an O/C=1.2, 0.23 MPa, 900°C and 50,000 scc/$g_{catalyst}$/h. H_2 (♦), CO (■), CO_2 (▲), CH_4 (●).

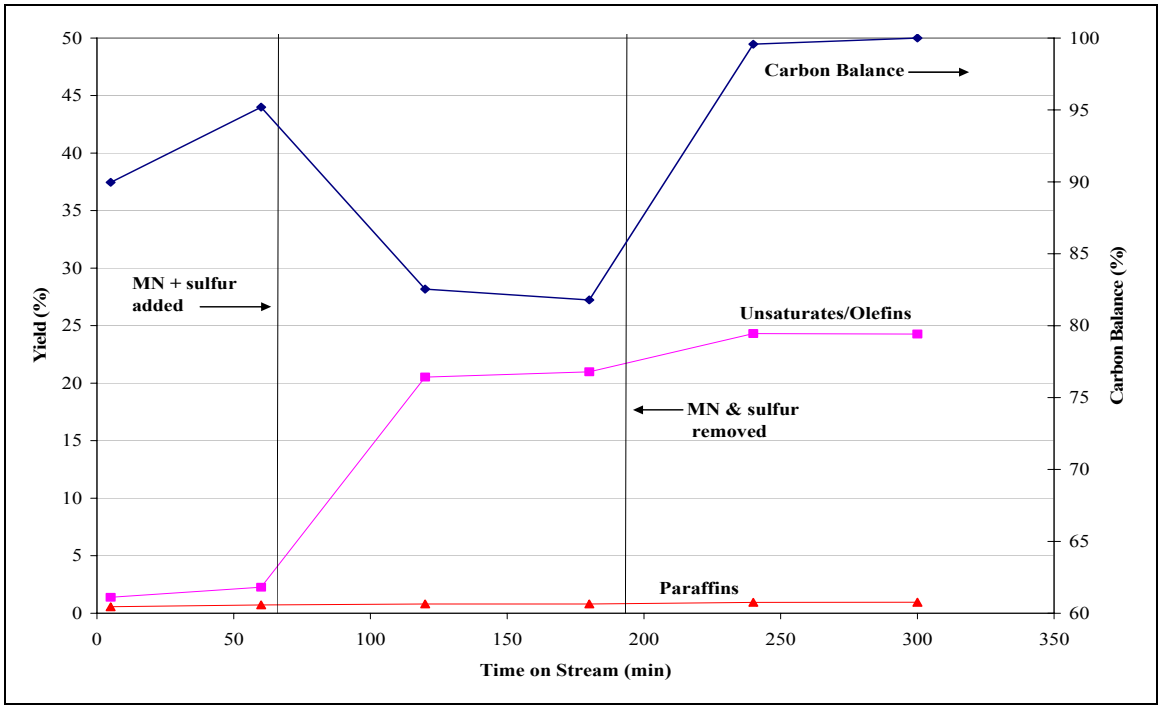

Figure 7.5 Paraffins, unsaturates yields and carbon balance for LZ during the CPOX of 5wt% MN + 1000 ppmw DBT in TD experiment at an O/C=1.2, 0.23 MPa, 900°C and 50,000 scc/$g_{catalyst}$/h. Conversion (♦), Olefins (▲), Paraffins (■).

Table 7.4 Comparison of C_2-C_6 and benzene yields produced over LZ during CPOX of TD only (before MN, DBT or both were added) and after 2 h of 5 wt% MN, 1000 ppmw DBT, and 5 wt% MN + 1000 ppmw DBT in the feed. The yields are also compared to C_2-C_6 and benzene yields over Rh/γ-Al_2O_3 after 5 wt% MN + 1000 ppmw DBT/TD experiment. Conditions for all experiments were O/C=1.2, 0.23 MPa, 900°C and 50,000 scc/$g_{catalyst}$/h.

	Rh/γ-Al_2O_3		**LZ**					
	TD only (before MN & DBT)	5 wt% MN & 1000 ppmw DBT	TD only (before MN)	5 wt% MN	TD only (before DBT)	1000 ppmw DBT	TD only (before MN & DBT)	5 wt% MN & 1000 ppmw DBT
Ethane	0.10	0.7	0.6	0.8	0.4	0.7	0.7	0.8
Ethylene	n.d.[a]	13.2	1.0	14.7	0.2	13.6	1.7	15.3
Propylene	n.d.	2.9	0.2	2.4	n.d.	1.8	0.1	2.4
1,3-Butadiene	n.d.	1.7	n.d.	n.d.	n.d.	n.d.	n.d.	n.d.
1-Hexene	n.d.	0.8	n.d.	n.d.	0.8	1.0	n.d.	n.d.
Benzene	n.d.	3.4	0.2	3.1	0.1	3.70	0.4	3.3

[a-] n.d..- not detected

7.1.2.2 Removal of MN and DBT

After removing the MN and DBT from the feed LZ is unable to recover any activity, indicating the catalytic activity has been irreversibly deactivated. Throughout recovery, the H_2 and CO yields remain at levels which resemble those produced in the blank reactor. The carbon balance is able to recover to 100%, and in doing so olefin yields surprisingly increase past levels seen while both MN and DBT were present. As this happens, the H/O ratio drops from ~2/1 to roughly 1.1-1.3, possibly indicating less oxidation of H_2 is occurring in the gas-phase and more pyrolysis.

7.1.2.3 Carbon Formation

The presence of MN and DBT deactivates the catalyst through excessive carbon formation on the active sites. From **Table 7.5**, it is observed that there is 7.1 times more carbon formed during this experiment compared to the CPOX of TD only, and 2.7 times greater than the CPOX of 1000 ppmw DBT/TD, in which the LZ only lost partial activity. The amount of carbon is roughly equivalent to that formed after the CPOX of 5 wt% MN/TD, (1.03 times greater), which saw the same effects on synthesis gas activity in Section 5.1.2.1. However, there is no catalytic activity recovery after the MN and DBT are removed, compared to the slight recovery after the MN was removed shown in Figure 5.4, suggesting that the combination of DBT and MNs lead to more carbon on the active sites than MN alone.

The reactivity of the carbon adsorbed to the surface of the LZ pyrochlore after the MN and DBT are removed is expressed in **Figure 7.6**, and compared to the other experiments over the LZ. Each profile shows carbon being oxidized over the temperature range of 400-900°C, indicating the reactivity of the carbon is qualitatively similar. However, like the MN profile, a large broad peak is observed over this range because of the large accumulation of carbon on the surface. The carbon appears to be forming on the three sites that are shown in the DBT profile, but there is such a high coverage of carbon that the peaks are indistinguishable.

Table 7.5 Amount of carbon formed on LZ pyrochlore after CPOX of TD only, 5 wt% MN/TD, 1000 ppmw DBT/TD, and 5 wt% MN + 1000 ppmw DBT/TD; 900°C, 50,000 scc/g_{cat}/h. Results are compared to carbon formed on Rh/γ-Al_2O_3 after 5 wt% MN + 1000 ppmw DBT/TD experiment; 900°C, 50,000 scc/$g_{catalyst}$/h.

Catalyst	Carbon ($g_{carbon}/g_{catalyst}$)
LZ (TD only)	0.30
LZ (After 5 wt% MN/TD)	2.06
LZ (After 1000 ppmw DBT/TD)	0.80
LZ (After 5 wt% MN + 1000 ppmw DBT/TD)	2.13
Rh/γ-Al_2O_3 (After 5 wt% MN +1000 ppmw DBT/TD)	1.10

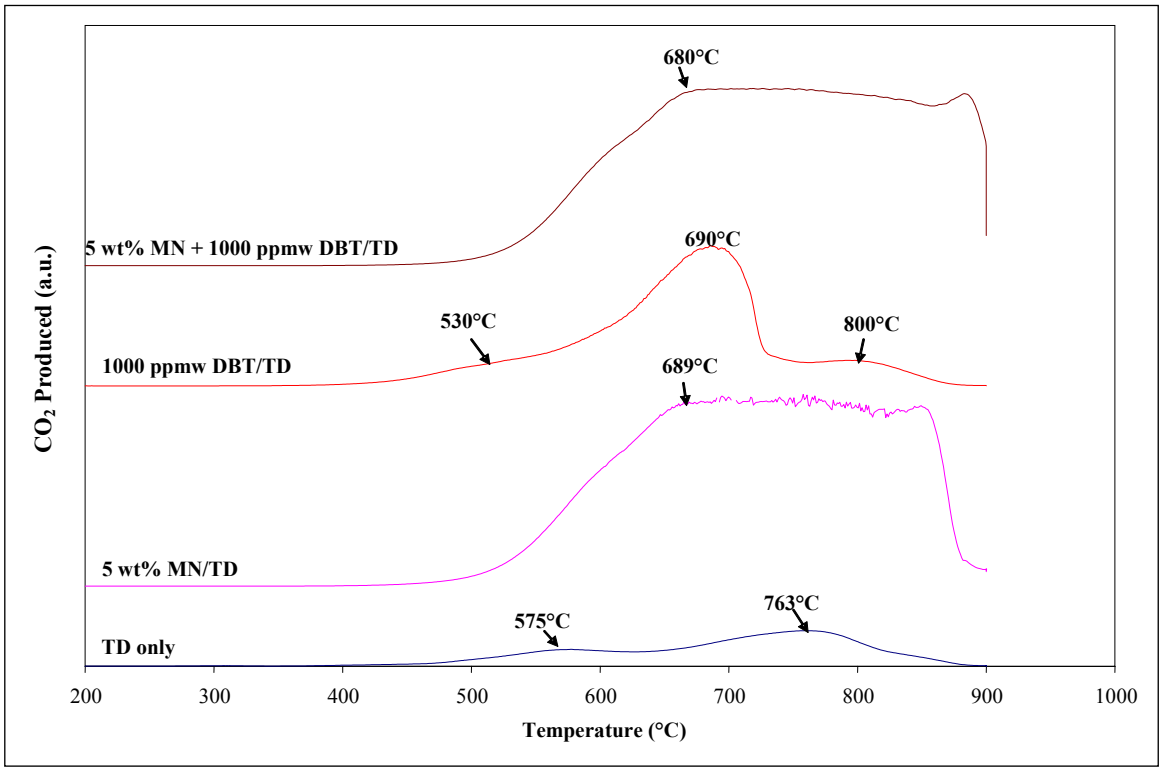

Figure 7.6 TPO profiles for LZ after CPOX of 5 wt% MN + 1000 ppmw DBT/ TD, 1000 ppmw DBT/TD, 5-wt% MN/TD and TD only.

7.1.3 LRZ

7.1.3.1 Effect of MN and DBT on Synthesis Gas Yield

In the presence of MN and DBT together, the LRZ catalyst shows a greater resistance to deactivation compared to the LZ and Rh/γ-Al_2O_3. The step response plots detailing the effects of 5 wt% MN + 1000 ppmw DBT together on activity and conversion of LRZ are shown in **Figures 7.7** and **7.8**. While MN and DBT are in the feed, the LRZ has a loss of activity that is qualitatively similar to the effects of MN only and DBT only: the H_2 and CO yields drop together at an H_2/CO ratio equal to that which they were produced during CPOX of TD only. Again, it is unclear after this experiment, whether the yields will continue to decline until the catalyst is deactivated, or eventually level off. Still, gradual decline in the catalytic activity suggests that, although MN and DBT are present together, they do not immediately adsorb to the active sites (Rh metal) as they did for the Rh and LZ, and deactivate the catalyst. This is further evidence that substituting the metal into the structure creates well-dispersed active metal sites which are more resistant to deactivation by sulfur and carbon.

However, together, the MN and DBT have a more adverse effect on catalytic activity compared to MN or DBT alone. H_2 and CO yields drop at a faster rate, 0.27% H_2 or CO/ min, during this experiment, compared to 0.18%/min drop in the presence of either MN or DBT only. Then, consequently, Figure 7.8 shows there is a greater amount of gas-phase reactions that occur in the system compared to Figure 5.8 for MN or Figure 6.8 for DBT only as well. As shown in **Table 7.6**, the selectivity of the olefins produced is qualitatively similar to the other experiments: the formation of ethylene, propylene and benzene dominate as higher order reaction products compared to CPOX of TD only

before the contaminants were added. Also, the carbon balance drops to about 92%, which indicates the LRZ is unable to convert the all the fuel to detectible products as it did in the presence of MN only (Figure 5.8) and DBT only (Figure 6.8).

As there is an increase in gas-phase reactions in the system, it is likely steam formation begins to occur and can be attributed to, at least partially, the decrease in H_2. The mass balance over H and O containing species indicates they may be in the correct ratio to confirm steam is the only reaction product containing H and O, as the atomic H/O ratio was 1.7/1 ±1.0 while the MN and DBT were present.

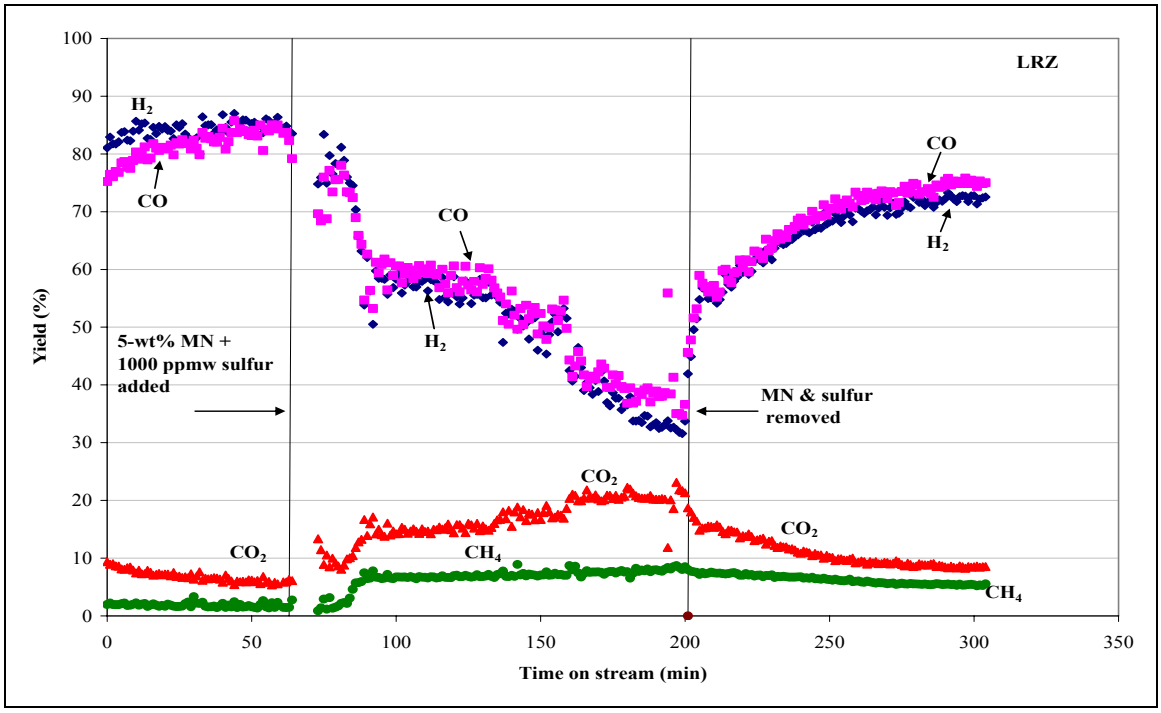

Figure 7.7 Step response plot for LZ after the addition of 5 wt% MN + 1000 ppmw DBT at an O/C=1.2, 0.23 MPa, 900°C and 50,000 scc/$g_{catalyst}$/h. H_2 (♦), CO (■), CO_2 (▲), CH_4 (●).

7.1.3.2 Removal of MN and DBT

Once the MN and DBT are removed from the feed, activity begins to return for the LRZ catalyst. There is a gradual return of H_2 and CO yields to roughly 87% and 85% of their initial values, respectively. Also during this time, olefin yields decrease back to pre-contaminate levels and the carbon balance returns slightly to 94%. The lack of the ability to recover initial activity shows that some of the active sites have been irreversibly poisoned. However, the substituted Rh metal is able to recover to a higher activity after MN and DBT are removed, compared to the supported Rh/γ-Al_2O_3. This further indicates the distribution of Rh throughout the pyrochlore structure is able to decrease the irreversible deactivation of the metal cause by the contaminants.

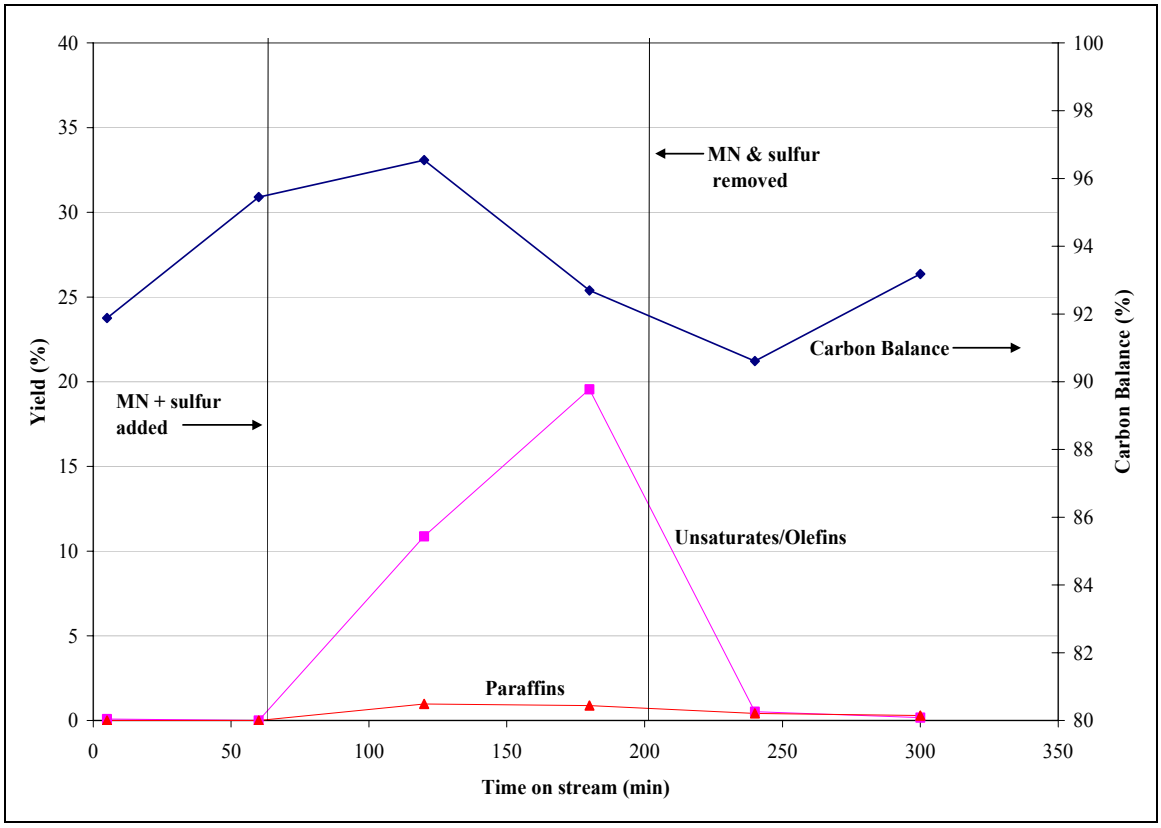

Figure 7.8 Paraffins, unsaturates yields and carbon balance for LZ during the CPOX of 5wt% MN + 1000 ppmw DBT in TD experiment at an O/C=1.2, 0.23 MPa, 900°C and 50,000 scc/$g_{catalyst}$/h. Conversion (♦), Olefins (▲), Paraffins (■).

Table 7.6 Comparison of C_2-C_6 and benzene yields produced over LRZ during CPOX of TD only (before MN, DBT or both were added) and after 2 h of 5 wt% MN, 1000 ppmw DBT, and 5 wt% MN + 1000 ppmw DBT in the feed. The yields are also compared to C_2-C_6 and benzene yields over Rh/γ-Al_2O_3 and LZ after 5 wt% MN + 1000 ppmw DBT/TD experiment. Conditions for all experiments were O/C=1.2, 0.23 MPa, 900°C and 50,000 scc/$g_{catalyst}$/h.

	Rh/γ-Al_2O_3		**LZ**		**LRZ**					
	TD only (before MN & DBT)	5 wt% MN & 1000 ppmw DBT	TD only (before MN & DBT)	5 wt% MN & 1000 ppmw DBT	TD only (before MN)	5 wt% MN	TD only (before DBT)	1000 ppmw DBT	TD only (before MN & DBT)	5 wt% MN & 1000 ppmw DBT
Ethane	0.10	0.7	0.7	0.8	n.d.	0.8	n.d.	0.9	n.d.	0.9
Ethylene	n.d.[a]	13.2	1.7	15.3	n.d.	8.8	n.d.	8.9	n.d.	13.8
Propylene	n.d.	2.9	0.1	2.4	n.d.	1.4	n.d.	1.3	n.d.	2.2
1,3-Butadiene	n.d.	1.7	n.d.	n.d.	n.d.	n.d.	n.d.	n.d.	n.d.	0.8
1-Hexene	n.d.	0.8	n.d.	n.d.	n.d.	n.d.	n.d.	n.d.	n.d.	n.d.
Benzene	n.d.	3.4	0.4	3.3	n.d.	2.5	n.d.	3.4	n.d.	2.8

[a]-n.d.- not detected

7.1.3.3 Carbon Formation

The amount of carbon formed on the LRZ after the CPOX of 5 wt% MN + 1000 ppmw DBT/TD is presented in **Table 7.7**. The results are compared to carbon formed over LRZ after CPOX of 5 wt%/TD and 1000 ppmw DBT/TD, as well as on Rh/γ-Al_2O_3 and LZ after CPOX of 5 wt% MN + 1000 ppmw DBT/TD.

The presence MN and DBT together produce less carbon over LRZ compared to CPOX of 5 wt% MN/TD (1.06 versus 1.20 $g_{carbon}/g_{catalyst}$), but more than after the CPOX of 1000 ppmw DBT/TD (1.06 versus 0.86 $g_{carbon}/g_{catalyst}$). A possible explanation for this has been discussed previously in Section 6.1.3.3; the sulfur molecules may adsorb to the active sites and "shield" them from carbon deposition. However, the shielding effects of sulfur appear to become minimized in the presence of MN.

Less carbon is formed over the LRZ compared to LZ (2.1 times less), after the same experiment. This is to be expected, as the substitution of Rh decreases the rate of carbon formation of MN on the pyrochlore surface, which severely deactivates the un-substituted LZ in Sections 5.1.2.3 and 7.1.2.3. Also, the LRZ has essentially the same amount of carbon formed on its surface compared to the Rh/γ-Al_2O_3 (1.06 versus 1.10 $g_{carbon}/g_{catalyst}$). However, the substituted Rh in LRZ was able to produce higher synthesis gas yields once the feed was switched back to TD only (Figure 7.7). As indicated in Sections 5.1.3.3 and 6.1.3.3, the ability to recover activity suggests the carbon forms gradually over the pyrochlore surface and not explicitly on the Rh metal sites.

TPO profiles for each of these experiments are presented in **Figure 7.9**. As can be seen, the Rh/γ-Al_2O_3 shows more carbon adsorbed to the Rh metal and metal-support interface due to the MN and DBT. However, the LRZ profile does not have peaks

associated with Rh metal. Instead, the profile shows a slight shoulder at 550°C and large peak at 714°C which are consistent to the profiles for LRZ after MN and DBT experiments. These peaks have been attributed to carbon adsorbed on the pyrochlore. Unlike the other experiments the presence of DBT and MN together decrease the formation of the lower reactive carbon that is burns off between 787-795°C.

Table 7.7 Amount of carbon formed on LRZ pyrochlore after CPOX of TD only, 5 wt% MN/TD, 1000 ppmw DBT/TD, and 5 wt% MN + 1000 ppmw DBT/TD; 900°C, 50,000 scc/g_{cat}/h. Results are compared to carbon formed on Rh/γ-Al_2O_3 and LZ after 5 wt% MN + 1000 ppmw DBT/TD experiment; 900°C, 50,000 scc/$g_{catalyst}$/h.

Catalyst	Carbon ($g_{carbon}/g_{catalyst}$)
LRZ (After 5 wt% MN + 1000 ppmw DBT/TD)	1.06
LRZ (After 1000 ppmw DBT/TD)	0.86
LRZ (After 5 wt% MN/TD)	1.20
LZ (After 5 wt% MN + 1000 ppmw DBT/TD)	2.13
Rh/γ-Al_2O_3 (After 5 wt% MN +1000 ppmw DBT/TD)	1.10

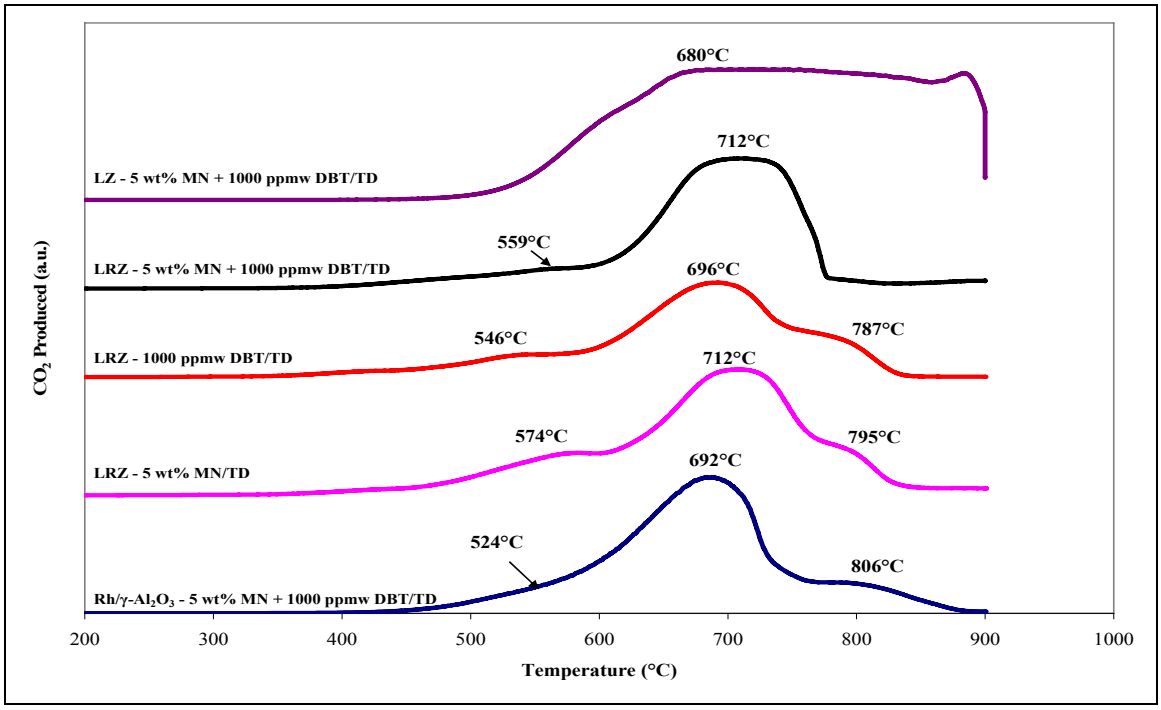

Figure 7.9 TPO profiles from LRZ after CPOX of 5 wt% MN + 1000 ppmw DBT/TD, 1000 ppmw DBT/TD, 5 wt% MN/TD and compared to TPO profiles of LZ and Rh/γ-Al_2O_3 after CPOX of 5 wt% MN + 1000 ppmw DBT/TD.

7.1.4 LSRZ

7.1.4.1 Effect of MN and DBT on Synthesis Gas Yield

The substitution of Sr into the structure prevents the deactivation of the Rh sites in the pyrochlore and minimizes the effects of the contaminants. As shown in **Figures 7.10** and **7.11**, the H_2 and CO yields drop 24% and 13% respectively, but remain steady while MN and DBT are present. As before, the reduction in synthesis gas yields is followed by an increase in gas-phase reaction products (Figure 7.11), with selectivity similar to the other three catalysts (**Table 7.8**). However, similar to sections 5.1.4.1 and 6.1.4.1, the yield of these gas-phase reaction products that are formed in the presence of MN and DBT are far less over the LSRZ compared to these catalysts. As discussed in these sections, this behavior is likely directly related to the mobilized lattice oxygen anions in the pyrochlore structure that oxidize the adsorbed sulfur and MN into favorable products.

However, similar to the Rh/γ-Al_2O_3, the combined effects of MN and DBT on the catalytic activity of the LSRZ are not additive, but rather comparable to both contaminants individually. DBT alone (Section 6.1.4.1) had the most detrimental effect on catalyst activity, leading to roughly 24% and 20% decrease in H_2 and CO yields, respectively, and also produced the highest amounts of olefins over LSRZ. The effects of MN (Section 5.1.4.1) were slightly less adverse, as H_2 and CO yields dropped 20% and 15% respectively, and less olefins were produced (2.4% during CPOX of 5 wt% MN/TD compared to ~6% during the CPOX of 1000 ppmw DBT/TD). Combining the contaminants together results in a 23% drop in H_2 yield and 16% drop in CO, with slightly greater than 4.5% olefin yield. As MN and DBT compete for adsorption onto

active sites, these results suggest they may have equal rates of adsorption onto the LSRZ surface.

As discussed in sections 5.1.4.1 and 6.1.4.1, the selectivity change toward gas-phase reaction products indicates steam is likely forming. A calculation was made to determine whether the unreacted H and O atoms are in the correct amount to attribute the imbalance in these species to steam. The mass balance over the H and O atoms shows a ratio of 24.6/1 ±19.1. As there is a large discrepancy in this value, the analysis cannot exclude the fact that there may be other reaction products which may also account for missing H and O. Still, as homogeneous chemistry is occurring, it is likely steam formation is occurring as well.

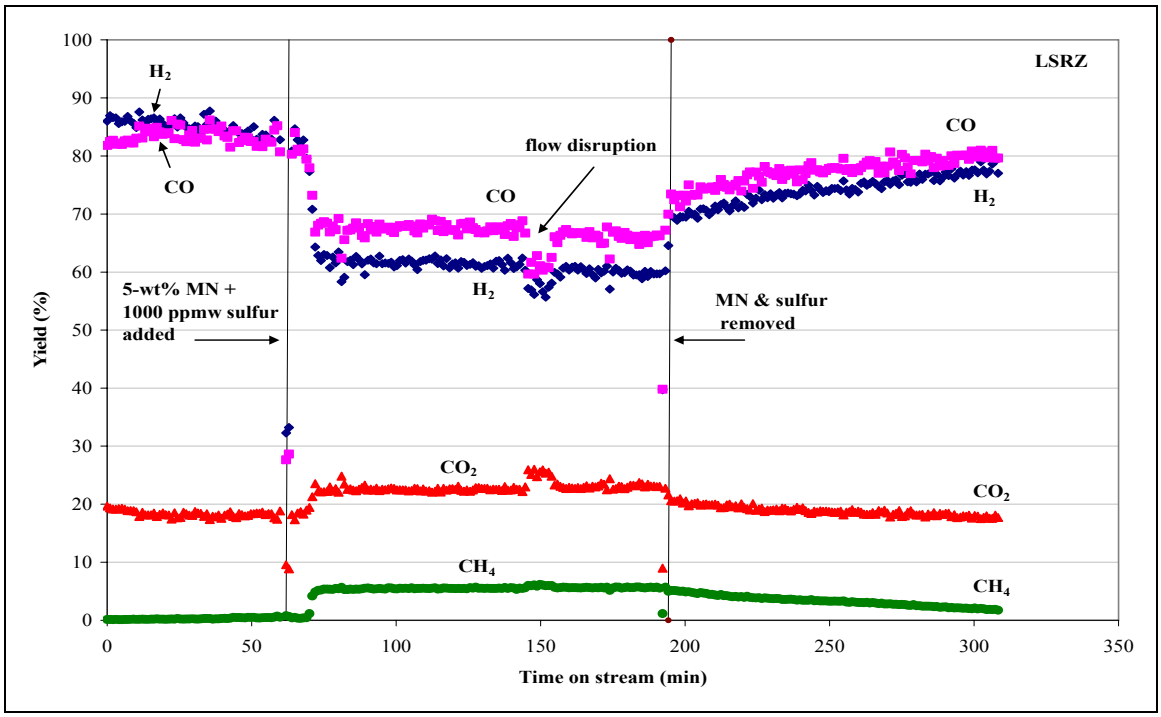

Figure 7.10 Step response plot for LSRZ after the addition of 5 wt% MN + 1000 ppmw DBT at an O/C=1.2, 0.23 MPa, 900°C and 50,000 scc/$g_{catalyst}$/h. H_2 (♦), CO (■), CO_2 (▲), CH_4 (●).

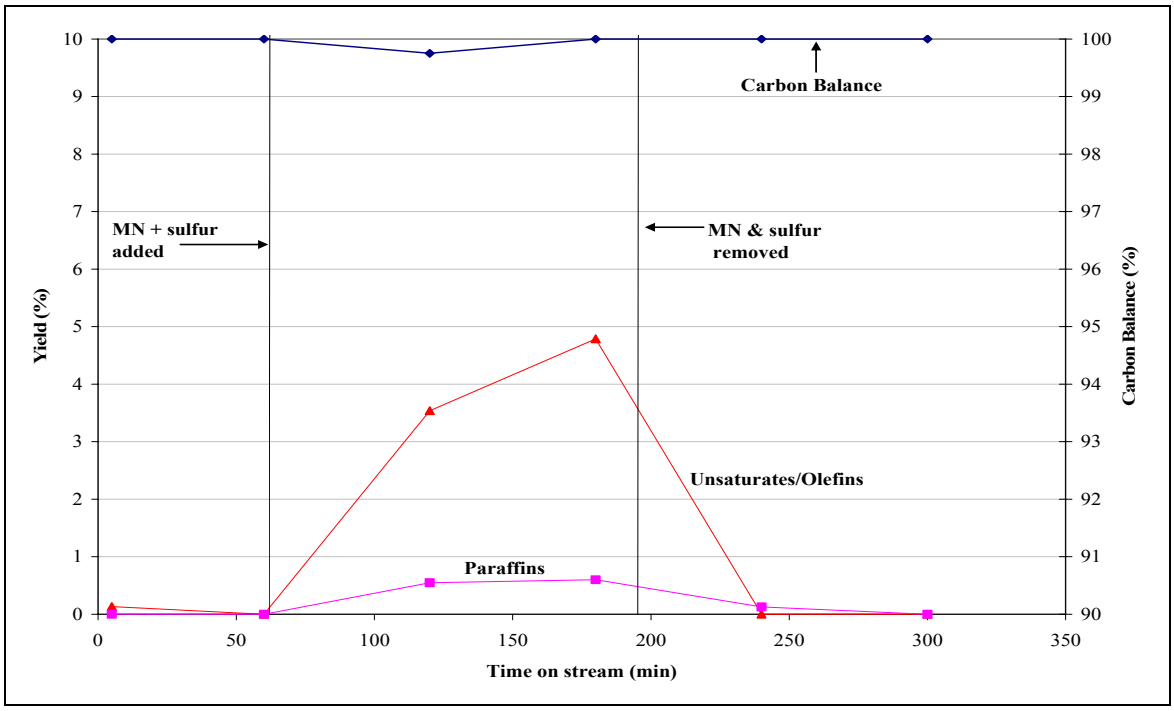

Figure 7.11 Paraffins, unsaturates yields and carbon balance for LSRZ during the CPOX of 5wt% MN + 1000 ppmw DBT in TD experiment at an O/C=1.2, 0.23 MPa, 900°C and 50,000 scc/$g_{catalyst}$/h. Conversion (♦), Olefins (▲), Paraffins (■).

7.1.4.2 Removal of MN and DBT

Once the DBT and MN are removed from the feed, the H_2 and CO yields are able to return to initial levels. Then as the catalyst's activity recovers, gas-phase reactions are virtually non-existent as olefin yields return to non-detectible levels and the CO_2 yield decreases to its initial value. Thus, the ability of the catalyst to regain activity to initial levels indicates that the substitution of Sr is able to reduce the effects of both contaminants on the active site such that they are reversible, at least over the time scale of the experiment.

Table 7.8 Comparison of C_2-C_6 and benzene yields produced over LSRZ during CPOX of TD only (before MN, DBT or both were added) and after 2 h of 5 wt% MN, 1000 ppmw DBT, and 5 wt% MN + 1000 ppmw DBT in the feed. The yields are also compared to C_2-C_6 and benzene yields over Rh/γ-Al_2O_3, LZ and LRZ after 5 wt% MN + 1000 ppmw DBT/TD experiment. Conditions for all experiments were O/C=1.2, 0.23 MPa, 900°C and 50,000 scc/$g_{catalyst}$/h.

	Rh/Al_2O_3		**LZ**		**LRZ**		**LSRZ**					
	TD only	MN + 1000 ppmw S	TD only	MN + 1000 ppmw S	TD only	MN + 1000 ppmw S	TD only	5 wt% MN	TD only	1000 ppmw sulfur	TD only	MN + 1000 ppmw S
Ethane	0.1	0.7	0.6	0.8	n.d.	0.9	n.d.	0.5	n.d.	0.7	n.d.	0.6
Ethylene	0.1	13.2	1.0	15.3	n.d.	13.8	n.d.	1.6	n.d.	4.4	n.d.	2.7
Propylene	n.d.[a]	2.9	0.2	2.4	n.d.	2.2	n.d.	0.2	n.d.	0.5	n.d.	0.2
1,3-Butadiene	n.d.	1.7	n.d.	n.d.	n.d.	0.8	n.d.	n.d.	n.d.	n.d.	n.d.	n.d.
1-Hexene	n.d.	0.8	n.d.	n.d.	n.d.	n.d.	n.d.	n.d.	n.d.	n.d.	n.d.	n.d.
Benzene	n.d.	3.4	0.2	3.3	n.d.	2.8	n.d.	0.8	n.d.	1.8	n.d.	1.9

[a-] n.d..- not detected

7.1.4.3 Carbon Formation

Table 7.9 presents the quantity of carbon formed on the LSRZ catalyst after the CPOX of 5 wt% MN + 1000 ppmw DBT/TD. This result is compared to the carbon formed over the LSRZ after CPOX of 5 wt% MN/TD and 1000 ppmw DBT/TD, as well as that formed over Rh/γ-Al_2O_3, LZ and LRZ after 5 wt% MN + 1000 ppmw DBT/TD.

The LSRZ has a lower amount of carbon formed on the surface compared to the MN experiment, but greater than DBT experiment. A similar result was reported in Section 7.1.3.3, and the same explanation is likely true for the LSRZ: the sulfur adsorbs to the surface and occupies the active sites which also form carbon. Then, compared to the other 3 catalysts, the addition of Sr into the pyrochlore structure reduces the amount of carbon formed on the surface (0.39 $g_{carbon}/g_{catalyst}$ versus 1.06-2.10 $g_{carbon}/g_{catalyst}$). Again, this is to be expected because the oxygen ion conductivity of the material at the high reaction temperatures decreases the carbon formation induced by contaminants through the method stated in Section 4.1.2.

The reactivity of the adsorbed carbon is presented in the following TPO profile in **Figure 7.12**. It can be seen that the carbon accumulated on the LSRZ after MN and DBT experiment is much lower compared to the LRZ and LZ pyrochlores and Rh/γ-Al_2O_3. The reactivity of this carbon is qualitatively similar to that burned off LSRZ after DBT and MN experiments. The profile shows a broad peak at 657°C followed by a high temperature shoulder at 794°C. These peaks were attributed to the pyrochlore in section 6.1.4.3. Similar to the profile pertaining to the carbon burned off LSRZ after 1000 ppmw DBT/TD, the presence of sulfur appears to inhibit the accumulation of the more reactive carbon that forms on LSRZ during the MN experiment (576°C)

Table 7.9 Amount of carbon formed on LSRZ pyrochlore after CPOX of TD only, 5 wt% MN/TD, 1000 ppmw DBT/TD, and 5 wt% MN + 1000 ppmw DBT/TD; 900°C, 50,000 scc/g_{cat}/h. Results are compared to carbon formed on Rh/γ-Al_2O_3, LZ and LRZ after 5 wt% MN + 1000 ppmw DBT/TD experiment; 900°C, 50,000 scc/g_{cat}/h.

Catalyst	Carbon ($g_{carbon}/g_{catalyst}$)
LSRZ (After 5 wt% MN + 1000 ppmw DBT/TD)	0.39
LSRZ (After 1000 ppmw DBT/TD)	0.3
LSRZ (After 5 wt% MN/TD)	0.67
LRZ (After 5 wt% MN + 1000 ppmw DBT/TD)	1.06
LZ (After 5 wt% MN + 1000 ppmw DBT/TD)	2.13
Rh/γ-Al_2O_3 (After 5 wt% MN +1000 ppmw DBT/TD)	1.10

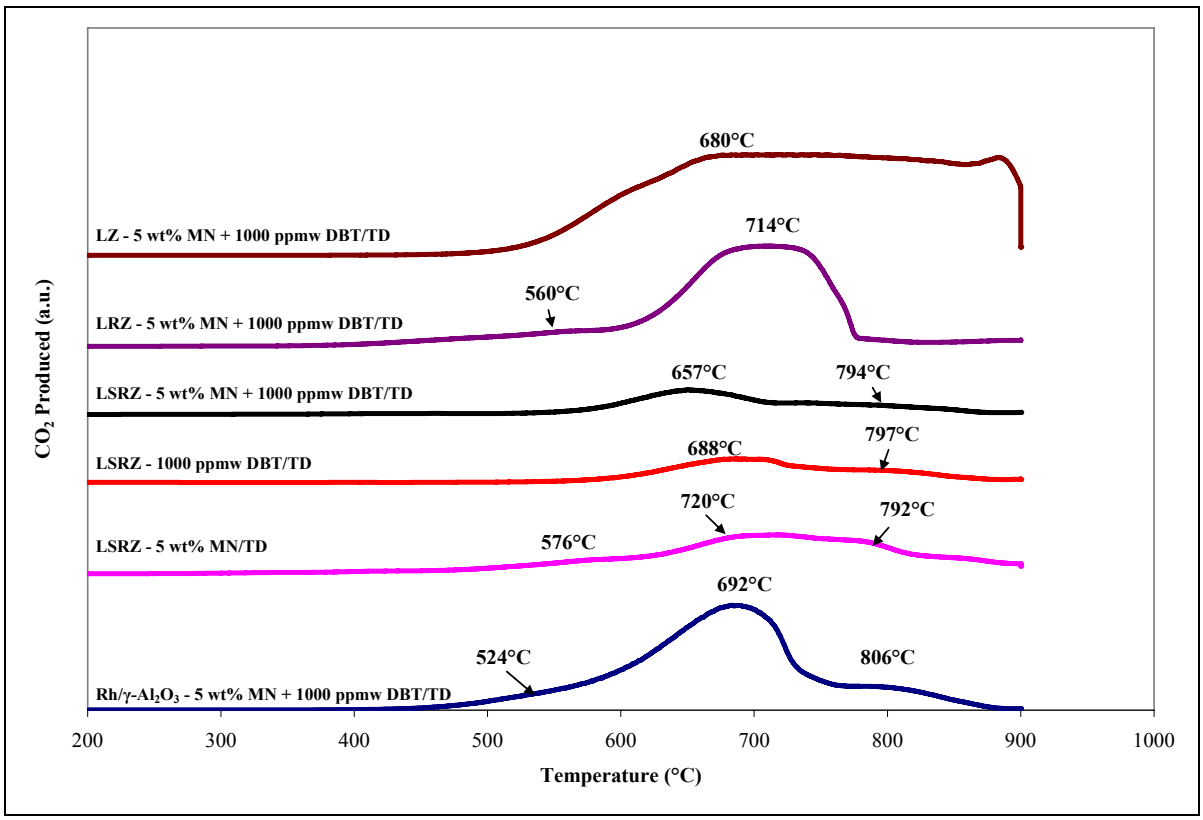

Figure 7.12 TPO profiles from LSRZ after CPOX of 5 wt% MN + 1000 ppmw DBT/TD, 1000 ppmw DBT/TD, 5 wt% MN/TD and compared to TPO profiles of LRZ, LZ and Rh/γ-Al_2O_3 after CPOX of 5 wt% MN + 1000 ppmw DBT/TD.

7.1.5 Post CPOX X-ray

After TPO of the final CPOX studies, each of the pyrochlores was examined by XRD to elucidate the phase stability of the unsubstituted and substituted pyrochlores at the high reactions temperatures seen during CPOX of the fuel (which were carried out at a nominal 900°C furnace setting, but likely reached several hundred degrees higher due to the heat of reaction) as well as the chemical stability in the redox conditions in the bed.

Results show the pyrochlore phase is a stable. **Figure 7.13** presents the diffraction patterns for each of the 3 pyrochlores used during the CPOX studies. The profiles for spent LZ and LRZ show the single phase pyrochlore structure that is identical to the fresh catalyst (Figure 3.1) as well as to profiles seen in the literature [65, 73]. However, the pattern for spent LSRZ is not consistent with the fresh material. The diffractogram shows the prevailing pyrochlore peaks are more intense and the perovskite peaks pertaining to $SrZrO_3$ are much lower. Main peaks corresponding to perovskite phase in Figure 3.1 at 31°, 45°, and 55° are only slightly visible in Figure 7.13. This is likely due to the saturation of the structure with oxygen during the TPO, which makes the defects less visible. It appears during initial calcination there is insufficient oxygen available from the natural convective air currents in the furnace to fully saturate the pyrochlore, so the defect perovskite phase is more apparent. However, during the TPO, after the carbon is burned off, the catalyst is essentially recalcined at 900°C, but exposed to a greater concentration of O_2. As a result, the matrial was able to uptake more O_2 into the structure-which produced a more saturated pyrochlore structure with less visible defects.

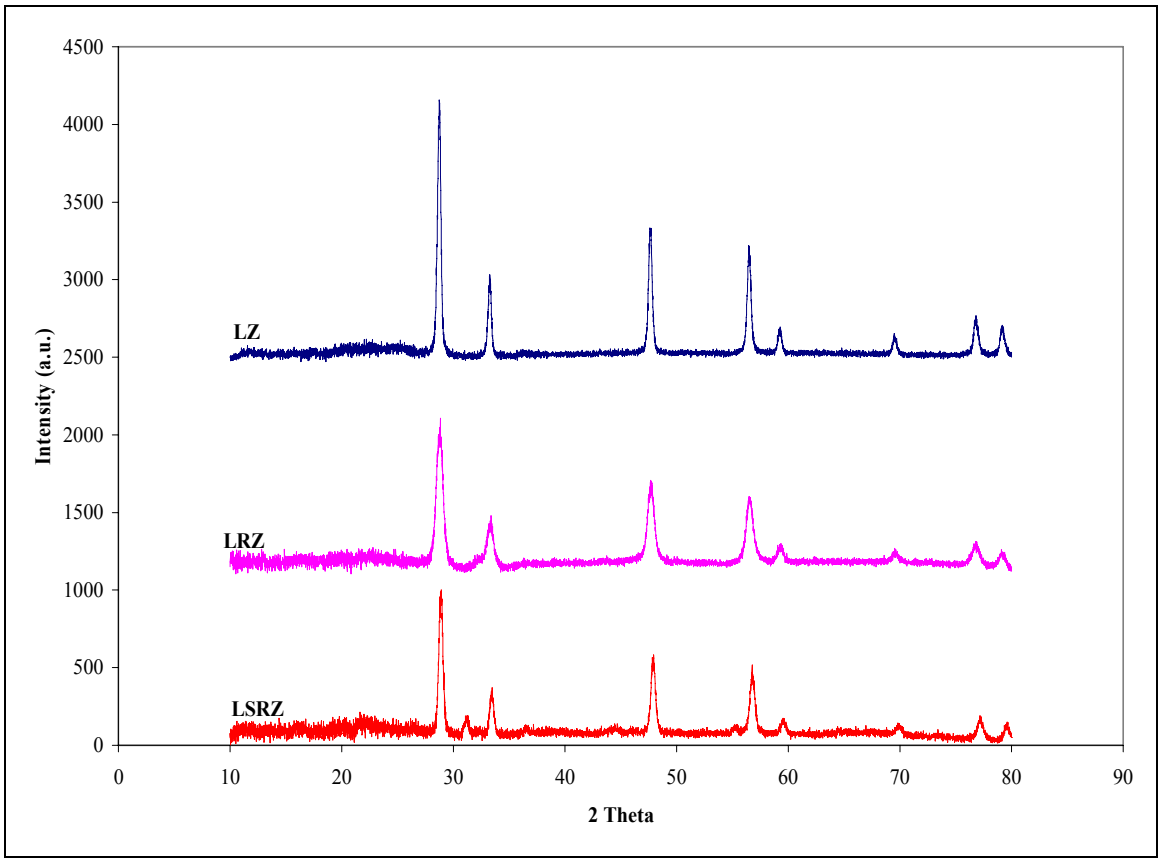

Figure 7.13 Diffraction patterns for LZ, LRZ and LSRZ after the four CPOX reactions and subsequent TPO's.

Chapter 8. Conclusions and Recommendations

The CPOX of logistic fuels can be used to provide a synthesis gas (H_2 and CO) fuel stream for fuel cells, such as high temperature SOFC. Unfortunately these fuels, depending on the feedstock, can have high levels of sulfur and aromatics which can deactivate the fuel reformer. Rhodium metal has been determined to be the most active CPOX catalyst, exhibiting high H_2 and CO yields with minimum carbon formation. However, the traditional supported metal catalyst design appears to be prone to deactivation by sulfur and carbon because these species poison metal clusters. Studies have shown that poisoning is linked to metal cluster size, with the larger clusters more prone to deactivation [39, 54, 55].

Therefore decreasing metal cluster size by substituting active metal into the structure of a stable crystal may create a well-dispersed active metal that is less susceptible to deactivation by sulfur and carbon. A lanthanum zirconate (LZ) $La_2Zr_2O_7$ pyrochlore was thought to be of interest for CPOX because it has shown to be chemically stable as a thermal barrier coating for gas turbines [63-66]. It has also shown the mechanical stability to withstand substitution (or doping) of lower valence state elements into the structure [65].

In this study, an LZ pyrochlore was substituted with 2 wt% Rh into the B-site for Zr with the intention to distribute the metal throughout the structure to create and maintain a well dispersed active metal for CPOX of liquid fuels. Further substitution of La^{3+} with Sr^{2+} was intended to create oxygen vacancies in the structure which can lead to lattice oxygen mobility at the high reaction temperatures of CPOX and possibly help reduce carbon formation.

Before CPOX studies, the structure of the pyrochlores were examined by several characterization techniques to understand physical and surface properties of the materials and their possible link to activity. In addition the fixed bed reactor used for CPOX studies was characterized for external and internal mass transport limitations that may affect reaction rate. Finally CPOX studies were performed using surrogate logistic fuel compounds chosen to represent diesel fuel mixtures. The studies included: CPOX of TD only to examine activity, CPOX of 5 wt% MN/TD to determine effects of aromatics, CPOX of 1000 ppmw DBT/TD to determine effects of organosulfur compounds, and finally CPOX of 5 wt% MN + 1000 pppmw DBT/TD to examine the effects of a simulated diesel fuel mixture. The results were compared to a commercial $Rh/\gamma\text{-}Al_2O_3$ catalyst

8.1 Conclusions: Catalyst Characterization

8.1.1 ICP

- Each of the pyrochlore catalysts was synthesized by the Pechini Method. ICP results confirmed that in each case the actual composition of La, Zr and Sr were greater than theoretical values for each respective pyrochlore. However, rhodium metal was found to be only 22-29% of theoretical values for the LRZ and LSRZ.

8.1.2 X-Ray Diffraction

- X-Ray analysis was able to prove LZ and LRZ had a single phase pyrochlore structure, as their x-ray patterns were consistent with those

found in the database as well as literature. However, the substitution of Sr created a defect perovskite phase in the LSRZ pyrochlore. The peaks indicated the defects are the result of the formation of $SrZrO_3$ perovksite.

8.1.3 BET Surface Area

- BET analysis showed the pyrochlores have a surface area on the order of 10 m^2/g_{cat}, compared to a much larger surface area of 100 m^2/g_{cat} for the $Rh/\gamma\text{-}Al_2O_3$. Consequently the low surface area values translates to a larger pore size for the pyrochlores, as they show an average pore size 1.6-2.2 times greater than the $Rh/\gamma\text{-}Al_2O_3$.

8.1.4 Temperature Programmed Reduction (TPR)

- TPR results over $Rh/\gamma\text{-}Al_2O_3$ showed two peaks, 136°C and 260°C, corresponding to the reduction of Rh metal. Each peak was attributed to the reduction of a RhO_x specie on the surface. Reduction of LZ pyrochlore showed a single high temperature reduction peak (527°C) which was attributed to reduction of pyrochlore. LRZ and LSRZ reduction profiles had high temperature reduction peaks, but also showed a small low temperature reduction peaks ~ 274-280°C. This peak was attributed to the reduction of partially coordinated Rh atoms at the surface of the pyrochlore. The reduction temperature for Rh in the pyrochlore structure was reduced at a higher temperature than the $Rh/\gamma\text{-}Al_2O_3$ due to the different interactions with neighboring atoms for each material.

8.1.5 Metal Dispersion

- Pulse chemisorption of H_2 was used to determine the percentage of exposed metal. The LRZ and LSRZ pyrochlores each showed a low dispersion, ~ 4 and 9% respectively compared to 77% dispersion of Rh/γ-Al_2O_3. Low dispersion values for the pyrochlores indicated the metal was distributed within the structure.

8.1.6 SEM and Microanalysis

- SEM images validated the pore size of the pyrochlores, showing microscale pore sizes between 25-50μm. However the resolution of the equipment was unable to verify, whether the Rh was substituted. Further examination of the surface using EDX was able show the Pechini Method produced a well mixed material because uniform elemental detection patterns of the surface were obtained for each catalyst during a point X-Ray analysis on two different particles of the same material.

8.1.7 External Transport Limitations

- By maintaining the same WHSV (ratio of flow rate/catalyst weight), but increasing the linear fluid velocity, it was determined that external mass transport limitations were nonexistent at the flow rates and catalyst weight used for the CPOX studies. At low flows, diffusion resistances in the boundary layer surrounding the catalyst affects transport of gas to surface.

However at higher flows, the diffusional resistances were reduced and the catalyst showed 100% conversion of fuel.

8.1.8 Internal Transport Limitations

- Thiele modulus was calculated based on assumptions of worst case scenario for intraparticle mass transport limitations. A powerlaw rate expression for ATR was assumed, but was modified for POX by assuming zero order for H_2O. As there were no kinetic paramerters for Rh, those for Pd were used because they would result in the highest reaction rate. After assumptions, the thiele modulus was calculated to be much less than 1, which indicated internal mass transport resistances did not exist.

8.2 Conclusions: CPOX Studies

8.2.1 CPOX of TD Only

- The substitution of Rh metal into the pyrochlore was shown to be active for the CPOX of n-tetradecane (TD) into synthesis gas. LRZ and LSRZ along with $Rh/\gamma\text{-}Al_2O_3$ were able to produce H_2 and CO yields close to equilibrium values for 5-h. Surprisingly the unsupported pyrochlore (LZ) was active for CPOX of TD as well, but less active compared to other 3 catalysts. CPOX of TD was also conducted in the absence of a catalyst (blank reactor). In the blank reactor, H_2 yields were low, while CO, CO_2 and olefins (mainly ethylene and propylene) were produced in large quantities.

8.2.2 Carbon Formed After CPOX of TD Only

- The amount of carbon, or "coke" formed on each catalyst after the CPOX of TD was quantitatively similar for each catalyst, with the exception of LSRZ, suggesting that the substitution of Sr led to oxygen ion mobility in the material, which was responsible for the reduction in carbon formation.

8.2.3 Effects of Polynuclear Aromatics

- Effects of the addition of 5 wt% 1-methylnaphthalene (MN) to TD resulted in a drop in synthesis gas yields for each catalyst. The reduction in activity was caused by a reactivity difference between MN and TD molecules at the catalyst surface. Activity loss was greatest for Rh/γ-Al_2O_3 and LZ, which were almost instantaneously deactivated in the presence of MN. LRZ and LSRZ showed a greater resistance to MN. Substitution of the Rh into the structure was able to slow deactivation by MN, as the LRZ showed a gradual deactivation of catalyst activity while MN was present. However, the addition of Sr was able to stabilize the reforming yields in the presence of MN, which resulted in a kinetic inhibition of catalyst activity.

8.2.4 Carbon Formed Due to Polynuclear Aromatics

- After MN was removed from the feed each catalyst recovered, at least partially, its original activity. Rh/γ-Al_2O_3 and LZ had the least amount of recovery due to the larger amount of carbon on the active sites. LRZ was

able to recover more activity that Rh/γ-Al_2O_3, which indicated less carbon accumulated on the Rh metal. However, the LRZ did have some activity loss due to poisoning of active sites. LSRZ was able to recover most of its initial activity, because of the lower amount of carbon on the surface.

8.2.5 Effects of Sulfur (as dibenzothiophene)

- Effects of the addition of 1000 ppmw dibenzothiophene (DBT) to TD resulted in a similar effect on catalyst activity as MN. The loss of activity was attributed to the decrease in the reaction rate by sulfur adsorbing to the active sites. Rh/γ-Al_2O_3 again suffered an instantaneous deactivation by the DBT; however, the effect of DBT on LZ was only a kinetic inhibition of the synthesis gas products. The substituted Rh in LRZ was less susceptible to deactivation by the sulfur compared to Rh/γ-Al_2O_3. Rather than an immediate deactivation, the LRZ had a gradual activity loss similar to the effects of MN. Further substitution with Sr was able to stabilize the synthesis gas yields and reduce the effects of DBT to a kinetic inhibition of reaction products. However the inhibition was much less compared to LZ.

8.2.6 Carbon Formed Due to Sulfur

- After DBT was removed activity was at least partially recovered for each catalyst. The Rh/γ-Al_2O_3 showed the least amount of recovery because of the larger amounts of carbon on active metal. However, each pyrochlore recovered more activity compared to after MN was removed because less

carbon was produced due to sulfur. The lower amount of carbon formed was attributed to the reversible adsorption of sulfur to the active sites of the pyrochlore, which also form carbon. LRZ was again able to recover more activity compared to the Rh/γ-Al_2O_3 which further indicated less carbon formed on the active sites. LSRZ recovered to almost initial activity because the oxygen ion conductivity was able to reduce the deactivation of catalyst by carbon by sulfur.

8.2.7 The Combined Effects of Polynuclear Aromatics and Sulfur

- Effects of the addition of 5 wt% MN and 1000 ppmw DBT to TD on catalyst activity were similar to the individual components. Rh/γ-Al_2O_3 and LZ were again instantly deactivated by the contaminants. However, again the substitution of Rh into the pyrochlore reduced the deactivation of the contaminants. LRZ showed a gradual deactivation of active sites similar to that of MN and DBT alone; however, the deactivation rate was faster in the presence of both contaminants. Substitution of Sr prevented deactivation of Rh by the contaminants. MN and DBT caused a drop in catalyst activity over LSRZ, but the yields remained constant over the time period they were present.

8.2.8 Carbon Formed Due to Polynuclear Aromatics and Sulfur

- Each catalyst recovered activity after the MN and DBT were removed. Rh/γ-Al_2O_3 and LZ again showed the least amount of recovery due to the larger accumulation of carbon on the active sites. Like before, the

substitution of Rh into the structure reduced the effects of MN and DBT that deactivated the Rh/γ-Al_2O_3. LRZ recovered a larger amount of activity compared to Rh/γ-Al_2O_3 because less carbon accumulated on the active sites. LSRZ recovered to almost initial activity, because the oxygen ion-conductivity minimized carbon formation on the Rh sites.

8.2.9 Post CPOX X-Ray Analysis

- After CPOX studies each pyrochlore was examined by X-ray to determine the phase stability of the material. Both the LZ and LRZ pyrochlores showed X-ray patterns similar to the fresh material. The diffraction pattern for LSRZ showed mainly peaks associated with the pyrochlores. The defect $SrZrO_3$ perovskite phase was less visible because of the up-take of oxygen into the structure during the high temperatures of the TPO.

8.3 Recommendations

It has been seen in this study that the LZ pyrochlore can be substituted with Rh and Sr to create a catalyst that is highly active for the CPOX of TD and resistant to deactivation by carbon and sulfur. However, there are some issues that will be discussed here that may be useful in further evaluating the material.

8.3.1 Optimize the Rh Metal Loading in the Pyrochlore Structure

Rationale: As seen from the metal dispersion results (Section 3.5), there is only a small percentage of the Rh exposed (~10 % of the 2 wt% for LSRZ). This leaves about 90% of the active metal embedded in the structure that is wasted. The high cost of Rh requires an

optimal Rh metal loading to minimize material costs and waste of metal. To do this, a series of LSRZ catalyst can be synthesized with various levels of Rh substitution. Substitution levels can range from 0 wt% to 2 wt%. Each catalyst can then be subjected to similar experiments: the 1st being CPOX of TD, using the conditions in this experiment (O/C=1.2, 900°C, and a WHSV 50,000 scc/$g_{catalyst}$/h) to test for activity. This experiment can be followed by the CPOX of 5 wt% MN + 1000 ppmw DBT/TD (at same conditions (O/C=1.2, 900°C, and a WHSV 50,000 scc/$g_{catalyst}$/h). The optimal loading would be the lowest substitution level of Rh that is able to resist deactivation by contaminants.

8.3.2 CPOX of Diesel Fuel

Rationale: Once the metal loading is optimized, the catalyst can be screened for the CPOX of a commercial diesel fuel. The experiment can have the similar procedure as the experiments described in this study: start with the CPOX of TD for 1 h to establish an initial activity baseline, then switch to diesel fuel for 2 h to examine effects on activity and selectivity. After 2 h the feed can be switched back to TD to examine the activity recovery. Should the catalyst maintain stable activity over the 2 h in the presence of the diesel fuel, it can be exposed to diesel for a longer duration.

References

[1] G. Hoogers (Ed.), Fuel Cell Technology Handbook, CRC Press LLC, Boca Raton, 2003.

[2] J. Larminie, A. Dicks, Fuel Cell Systems Explained 2ed., John Wiley and Sons, West Sussex, 2003.

[3] E.I.A. (EIA), Annual Energy Review, in: D.o. Energy (Ed.), Washington DC, 2005.

[4] C. Song, Catalysis Today 77 (2002) 17.

[5] B. Wiens, The Future of Fuel cells http://www.benwiens.com/energy4.html, 2002.

[6] D. Hart, G. Hormandinger, Journal of Power Sources 71 (1998) 348.

[7] A.B. Stambouli, E. Traversa, Renewable and Sustainable Energy Reviews 6 (2002) 433.

[8] M. Pehnt, Life Cycle Assessment of Fuel Cells and Relevant Fuel Chains, Hyforum The International Hydrogen Energy Forum, Munich, 2000.

[9] S. Ahmed, M. Krumpelt, International Journal of Hydrogen Energy 26 (2001) 291.

[10] L. F. Brown, International Journal of Hydrogen Energy 26 (2001) 381.

[11] S. Ahmed, R. Kumar, M. Krumpelt, Fuel Cells Bulletin 2 (Sept. 1999) 4.

[12] J.P. Trembly, A.I. Marquez, T.R. Ohrn, D.J. Bayless, Journal of Power Sources 158 (2006) 263.

[13] A.I. Marquez, T.R. Ohrn, J.P. Trembly, D.C. Ingram, D.J. Bayless, Journal of Power Sources In Press (2006).

[14] C.-J. Brodrick, T.E. Lipman, M. Farshchi, N.P. Lutsey, H.A. Dwyer, D. Sperling, I.I.I.S.W. Gouse, D.B. Harris, J.F.G. King, Transportation Research Part D: Transport and Environment 7 (2002) 303.

[15] S. Jain, H.-Y. Chen, J. Schwank, Journal of Power Sources 160 (2006) 474.

[16] D.K. Ross, Vacuum 80 (2006) 1084.

[17] D. Shekhawat, D.A. Berry, T.H. Gardner, J.J. Spivey, in: J.J. Spivey, K.M. Dooley (Eds.), Catalysis, The Royal Society of Chemistry, Cambridge, 2006, pp. 184-253.

[18] S. Ahmed, M. Krumpelt, R. Kumar, S.H.D. Lee, J.D. Carter, R. Vlilkenhoener, C. Marshall, Catalytic Partial Oxidation Reforming of Hydrocarbon Fuels, Fuel Cell Seminar, Palm Springs, CA, 1998.

[19] J. Winslow, Fischer-Tropsch Technology, CTL Seminar, NETL Morgantown, WV, 2006.

[20] I. Aartun, H.J. Venvik, A. Holmen, P. Pfeifer, O. Gorke, K. Schubert, Catalysis Today 110 (2005) 98.

[21] I. Kang, J. Bae, Journal of Power Sources 159 (2006) 1283.

[22] I. Kang, J. Bae, G. Bae, Journal of Power Sources 163 (2006) 538.

[23] A. Qi, S. Wang, C. Ni, D. Wu, International Journal of Hydrogen Energy In Press, Corrected Proof.

[24] H.H. Ibrahim, R.O. Idem, Chemical Engineering Science 61 (2006) 5912.

[25] K. Ahmed, K. Foger, Thermodynamic Analysis of Diesel Reforming Options for SOFC Systems, Electrochemical Society, Paris, Spring 2003.

[26] A. Lindermeir, S. Kah, S. Kavurucu, M. Muhlner, Applied Catalysis B: Environmental 70 (2007) 488.

[27] I. Report by Aurthur D. Little, Conceptual Design of POX/SOFC 5 kW net System, for Department of Energy (NETL), Cambridge, MA, 2001.

[28] L.D. Schmidt, E.J. Klein, C.A. Leclerc, J.J. Krummenacher, K.N. West, Chemical Engineering Science 58 (2003) 1037.

[29] Y. Jamal, M.L. Wyszynski, International Journal of Hydrogen Energy 19 (1994) 557.

[30] R.P. O'Connor, E.J. KLein, L.D. Schmidt, Catalysis Letters 70 (2000) 99.

[31] L. Bromberg, D.R. Cohn, A. Rabinovich, J. Heywood, International Journal of Hydrogen Energy 26 (2001) 1115.

[32] E. Galloni, M. Minutillo, International Journal of Hydrogen Energy In Press, Corrected Proof.

[33] A. Tsolakis, S.E. Golunski, Chemical Engineering Journal 117 (2006) 131.

[34] A. Abu-Jrai, A. Tsolakis, International Journal of Hydrogen Energy In Press, Corrected Proof.

[35] C. Song, C.S. Hsu, I. Mochida, Chemistry of Diesel Fuels, Taylor and Francis, New York, 2000.

[36] T. Aicher, L. Griesser, Journal of Power Sources 165 (2007) 210.

[37] C. Song, S. Eser, H.H. Schobert, P.G. Hatcher, Energy and Fuels 7 (1993) 234.

[38] E. Ranzi, M. Dente, A. Goldaniga, G. Bozzano, T. Faravelli, Progress in Energy and Combustion Science 27 (2001) 99.

[39] J. Barbier, in: B. Delmon, G.F. Froment (Eds.), Catalyst Deactivation, Elsevier Science, Amsterdam, 1987.

[40] A. Shamsi, J.P. Baltrus, J.J. Spivey, Applied Catalysis A: General 293 (2005) 145.

[41] P.K. Cheekatamarla, W.J. Thomson, Applied Catalysis A: General 287 (2005) 176.

[42] D. Shekhawat, T.H. Gardner, D.A. Berry, M. Salazar, D.J. Haynes, J.J. Spivey, Applied Catalysis A: General 311 (2006) 8.

[43] R. Subramanian, G.J. Panuccio, J.J. Krummenacher, I.C. Lee, L.D. Schmidt, Chemical Engineering Science 59 (2004) 5501.

[44] J.J. Krummenacher, K.N. West, L.D. Schmidt, Journal of Catalysis 215 (2003) 332.

[45] A. Roine, HSC Chemistry 4.0 ed., Outokumpu Research Oy, Pori, Finland, 1999.

[46] J. Lawrence, M. Boltze, Journal of Power Sources 154 (2006) 479.

[47] J.J. Krummenacher, L.D. Schmidt, Journal of Catalysis 222 (2004) 429.

[48] K.A. Williams, L.D. Schmidt, Applied Catalysis A: General 299 (2006) 30.

[49] M. Ferrandon, T. Krause, Applied Catalysis A: General 311 (2006) 135.

[50] D.A. Hickman, E.A. Haupfear, L.D. Schmidt, Catalysis Letters 17 (1993) 223.

[51] A. Beretta, P. Forzatti, Chemical Engineering Journal 99 (2004) 219.

[52] G.J. Panuccio, B.J. Dreyer, L.D. Schmidt, AIChE Journal 53 (2007) 187.

[53] P.M. Torniainen, X. Chu, L.D. Schmidt, Journal of Catalysis 146 (1994) 1.

[54] J. Barbier, G. Corro, P. Marecot, J.P. Bournonville, J.P. Frank, Reaction Kinetics Catalysis Letters 28 (1985) 245.

[55] J. Barbier, P. Marecot, Journal of Catalysis 102 (1986) 21.

[56] T.H. Gardner, D. Shekhawat, D.A. Berry, M.W. Smith, M. Salazar, E.L. Kugler, Submitted to Applied Catalysis A: General (2006).

[57] D.-J. Liu, M. Krumpelt, International Journal of Applied Ceramic Technology 2 (2005) 301.

[58] A. Qi, S. Wang, G. Fu, C. Ni, D. Wu, Applied Catalysis A: General 281 (2005) 233.

[59] P.J. Wilde, C.R.A. Catlow, Solid State Ionics 112 (1998) 173.

[60] P. Erri, P. Dinka, A. Varma, Chemical Engineering Science 61 (2006) 5328.

[61] M.A. Subramanian, G. Aravamudan, G.V.S. Rao, Progress in Solid State Chemistry 15 (1983) 55.

[62] S.J. Skinner, J.A. Kilner, Materials Today 6 (2003).

[63] D. Sedmidubsky, O. Benes, R.J.M. Konings, The Journal of Chemical Thermodynamics 37 (2005) 1098.

[64] R. Vasses, X. Cao, F. Tietz, D. Basu, D. Stover, Journal of American Ceramic Society 83 (2000) 2023.

[65] H. Zhou, D. Yi, Z. Yu, L. Xiao, Journal of Alloys and Compounds In Press, Corrected Proof.

[66] H. Dai, X. Zhong, J. Li, Y. Zhang, J. Meng, X. Cao, Materials Science and Engineering: A 433 (2006) 1.

[67] F. Tietz, A. Schmidt, M. Zahid, Journal of Solid State Chemistry 177 (2004) 745.

[68] M.P. Pechini, Method of preparing lead and alkaline earth titanates and niobates and coating method using the same to form a capacitor, United States, 1963.

[69] A. Majid, J. Tunney, S. Argue, D. Wang, M. Post, J. Margeson, Journal of Alloys and Compounds 398 (2005) 48.

[70] F.J. Lepe, J. Fernandez-Urban, L. Mestres, M.L. Martinez-Sarrion, Journal of Power Sources 151 (2005) 74.

[71] M.E. Davis, R.J. Davis, Fundamentals of Chemical Reaction Engineering, McGraw-Hill Co., New York, 2003.

[72] M. Ojeda, M. Lopez Granados, S. Rojas, P. Terreros, J.L.G. Fierro, Journal of Molecular Catalysis A: Chemical 202 (2003) 179.

[73] K. Koteswara Rao, T. Banu, M. Vithal, G.Y.S.K. Swamy, K. Ravi Kumar, Materials Letters 54 (2002) 205.

[74] F. Willy Poulsen, N. van der Puil, Solid State Ionics 53-56 (1992) 777.

[75] P.A. Webb, C. Orr, Analytical Methods in Fine Particle Technology, Micromeritics Instrument Corporation, Norcross, GA, 1997.

[76] C.-P. Hwang, C.-T. Yeh, Q. Zhu, Catalysis Today 51 (1999) 93.

[77] Z.-r. Li, Y.-l. Fu, M. Jiang, Applied Catalysis A: General 187 (1999) 187.

[78] W.-Z. Weng, X.-Q. Pei, J.-M. Li, C.-R. Luo, Y. Liu, H.-Q. Lin, C.-J. Huang, H.-L. Wan, Catalysis Today 117 (2006) 53.

[79] C. Wong, R.W. McCabe, Journal of Catalysis 107 (1987) 535.

[80] D.J. Haynes, D.A. Berry, D. Shekhawat, T.H. Gardner, J.J. Spivey, Submitted to Applied Catalysis A: General (2006).

[81] A. Beretta, E. Ranzi, P. Forzatti, Chemical Engineering Science 56 (2001) 779.

[82] N.J. Degenstein, R. Subramanian, L.D. Schmidt, Applied Catalysis A: General 305 (2006) 146.

[83] M. Guisnet, P. Magnoux, Applied Catalysis A: General 212 (2001) 83.

[84] J. Barbier, Applied Catalysis 23 (1986) 225.

[85] J. Barbier, in: B. Delmon, G.F. Froment (Eds.), Catalyst Deactivation, Amsterdam, 1987.

[86] R.M. Navarro, M.C. Alvarez-Galvan, J.A. Villoria, I.D. Gonzalez-Jimenez, F. Rosa, J.L.G. Fierro, Applied Catalysis B: Environmental In Press, Corrected Proof.

[87] J.P.Kopasz, D. Applegate, L. Miller, S. Ahmed, M.Krumpelt, Effects of Fuel Composition on Fuel Processing, The Annual National Laboratory R&D Meeting of the DOE Fuel Cells for Transportation Program, Denver, 2002.

[88] M.C. Huff, I.P. Androulakis, J.H. Sinfelt, S.C. Reyes, Journal of Catalysis 191 (2000) 46.

[89] G.J. Panuccio, K.A. Williams, L.D. Schmidt, Chemical Engineering Science 61 (2006) 4207.

[90] N. Martin, M. Viniegra, E. Lima, G. Espinosa, Industrial & Engineering Chemistry Research 43 (2004) 1206.

[91] L.F. Brown, International Journal of Hydrogen Energy 26 (2001) 381.

[92] D.-J. Liu, M. Krumpelt, H.-T. Chien, S.H. Sheen, Catalysts and Fuel Mixing for Diesel Reformer in Fuel Cell Auxiliary Power Unit, Fuel Cell Seminar, San Antonio, TX, 2004.

[93] Y. Deng, T.G. Nevell, R.J. Ewen, C.L. Honeyboume, M.G. Jones, Applied Catalysis A: General, 101 (1993) 51.

[94] J.M. Jones, V.A. Dupont, R. Brydson, D.J. Fullerton, N.S. Nasri, A.B. Ross, A.V.K. Westwood, Catalysis Today 81 (2003) 589.

[95] J.R. Rostrup-Nielsen, Journal of Catalysis 85 (1984) 31.

Appendix A. Extra SEM Images

LRZ

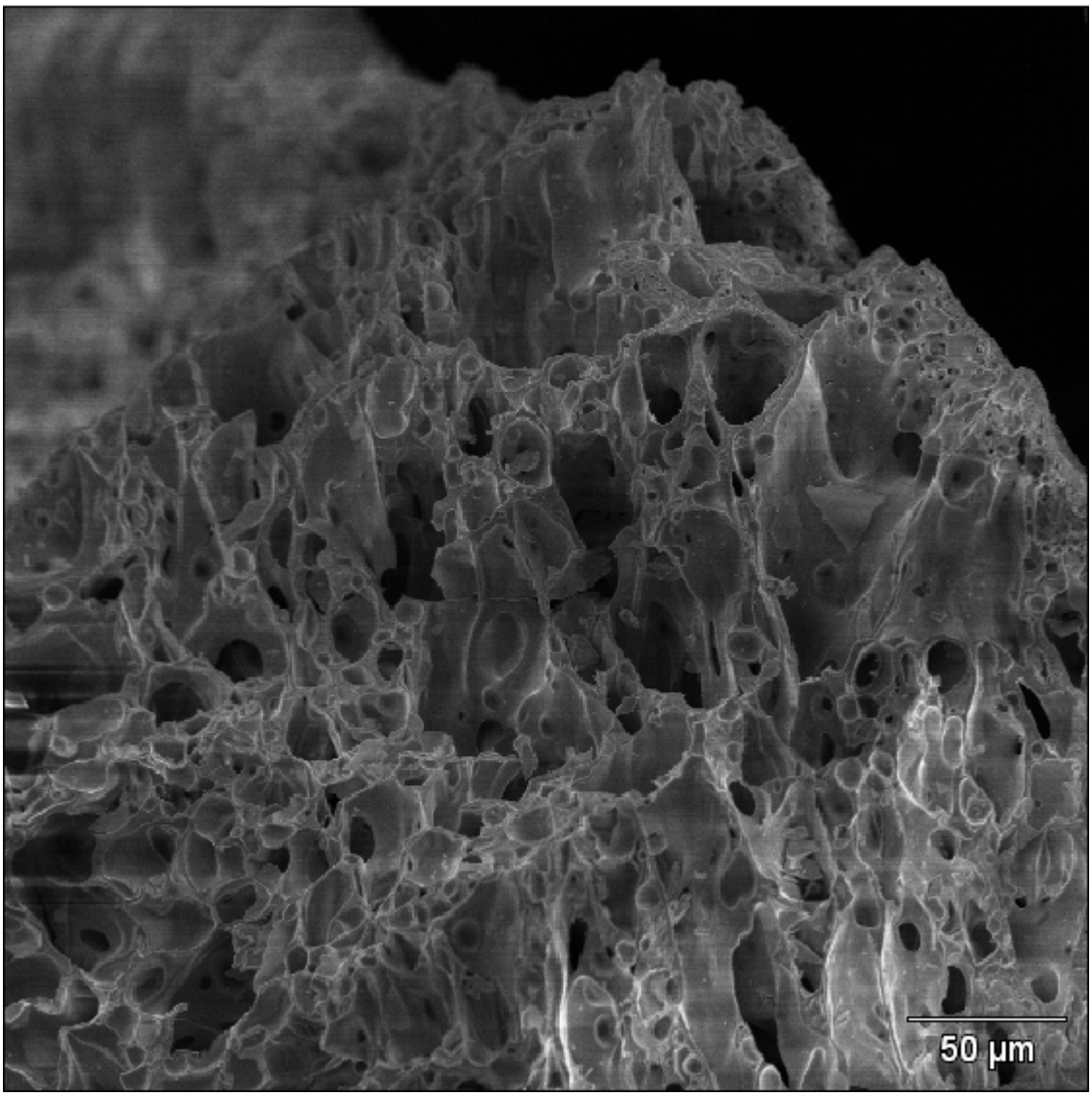

Accelerating Voltage: 10.0 kV Magnification: 350

Low magnification image of LRZ surface.

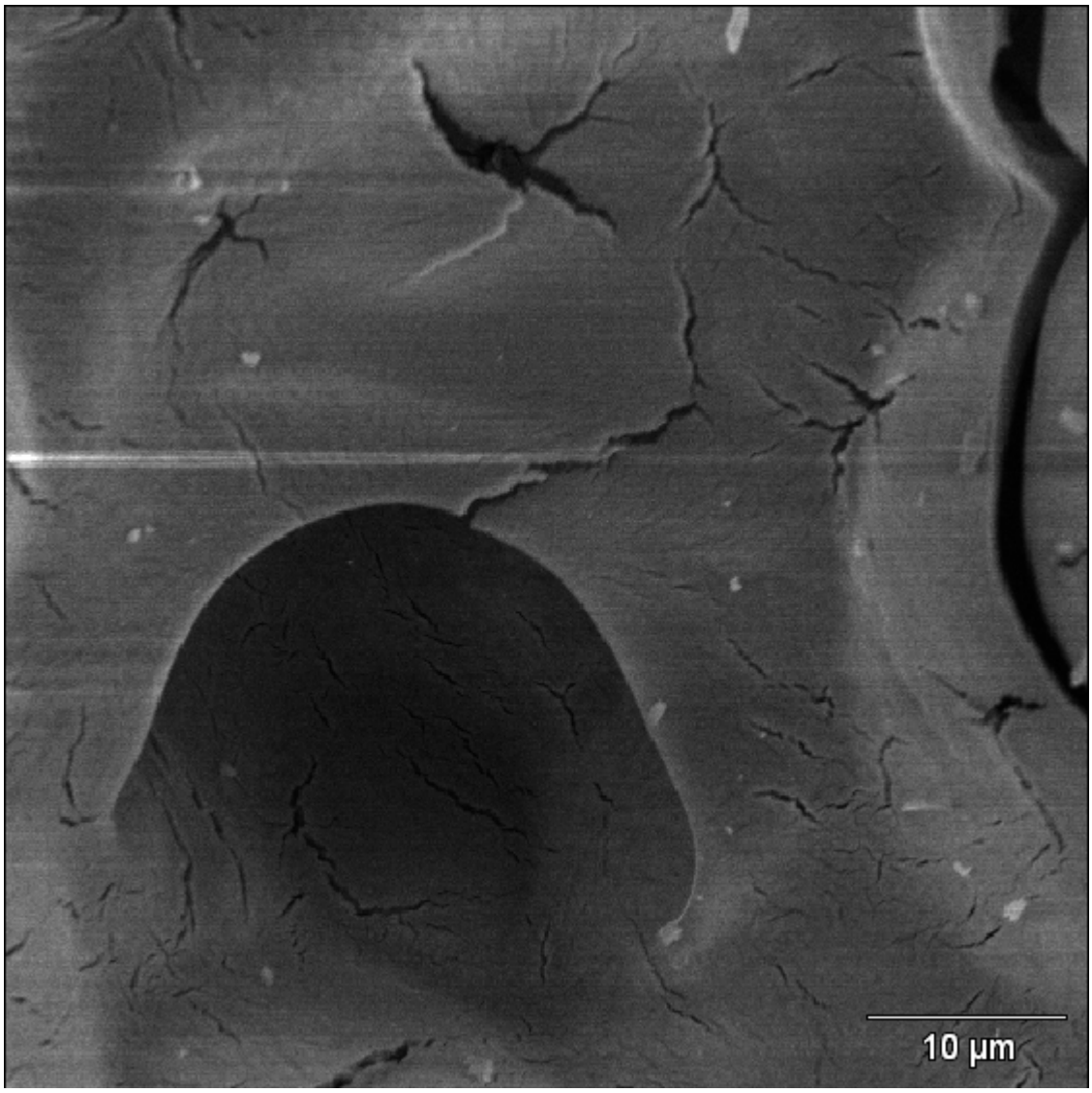

Accelerating Voltage: 10.0 kV Magnification: 2200

Close-up of pore on LRZ.

Surface composition of LRZ catalyst taken by EDS

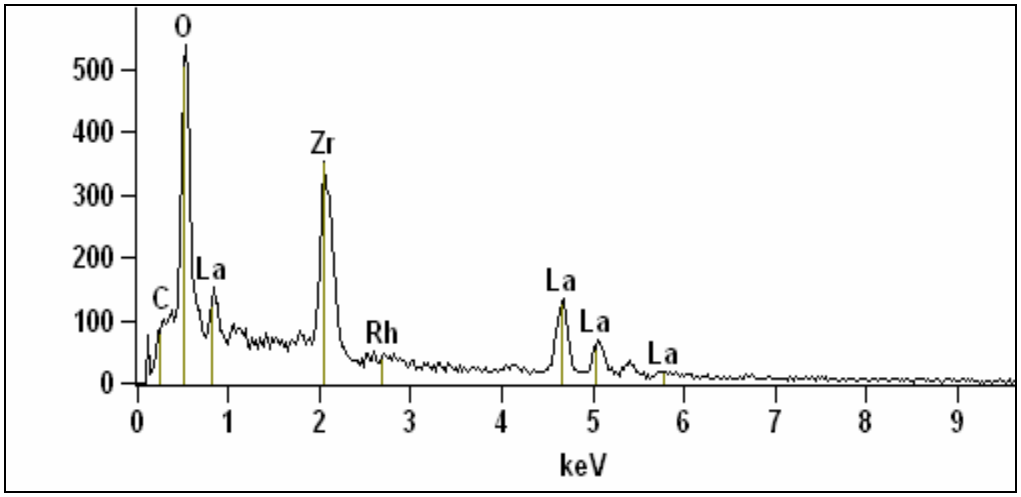

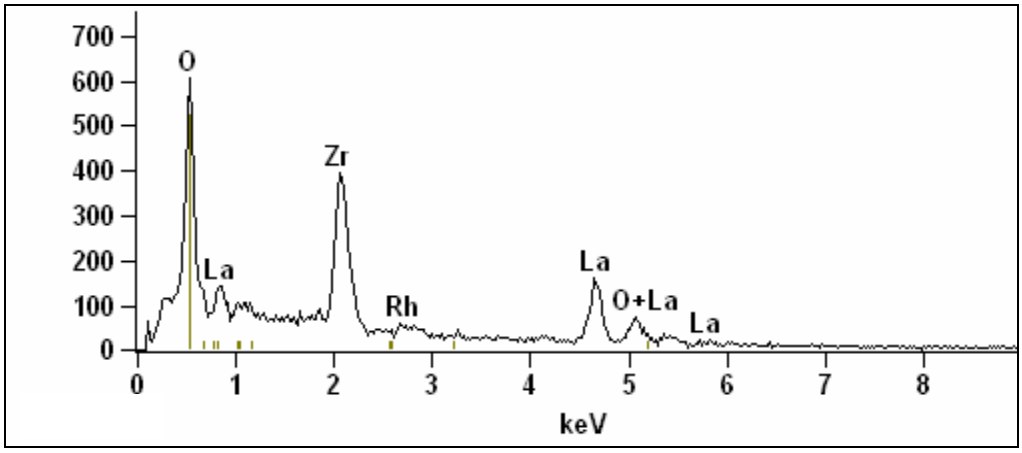

LZ

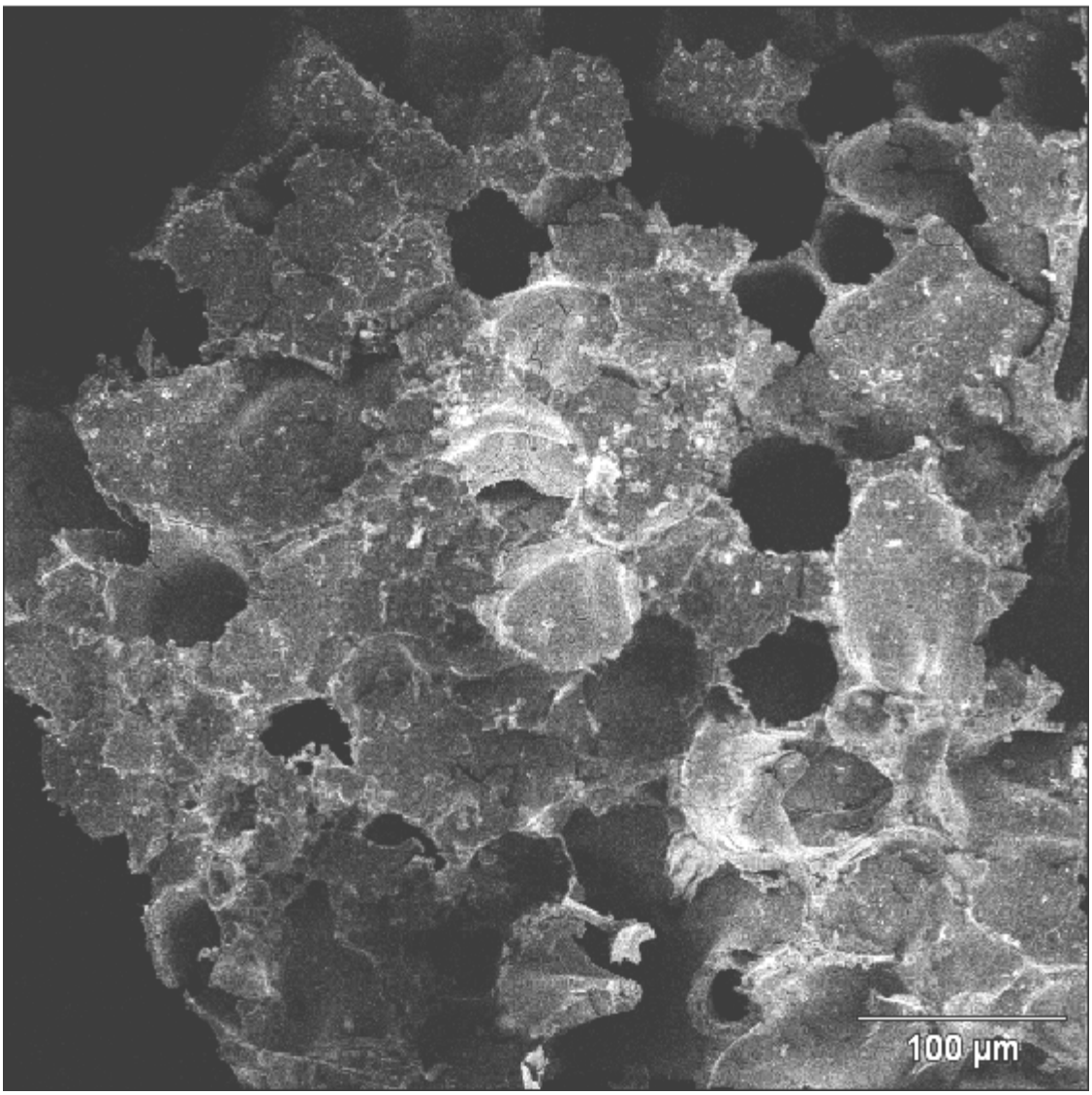

Accelerating Voltage: 10.0 kV Magnification: 230

Low Magnification image of LZ surface.

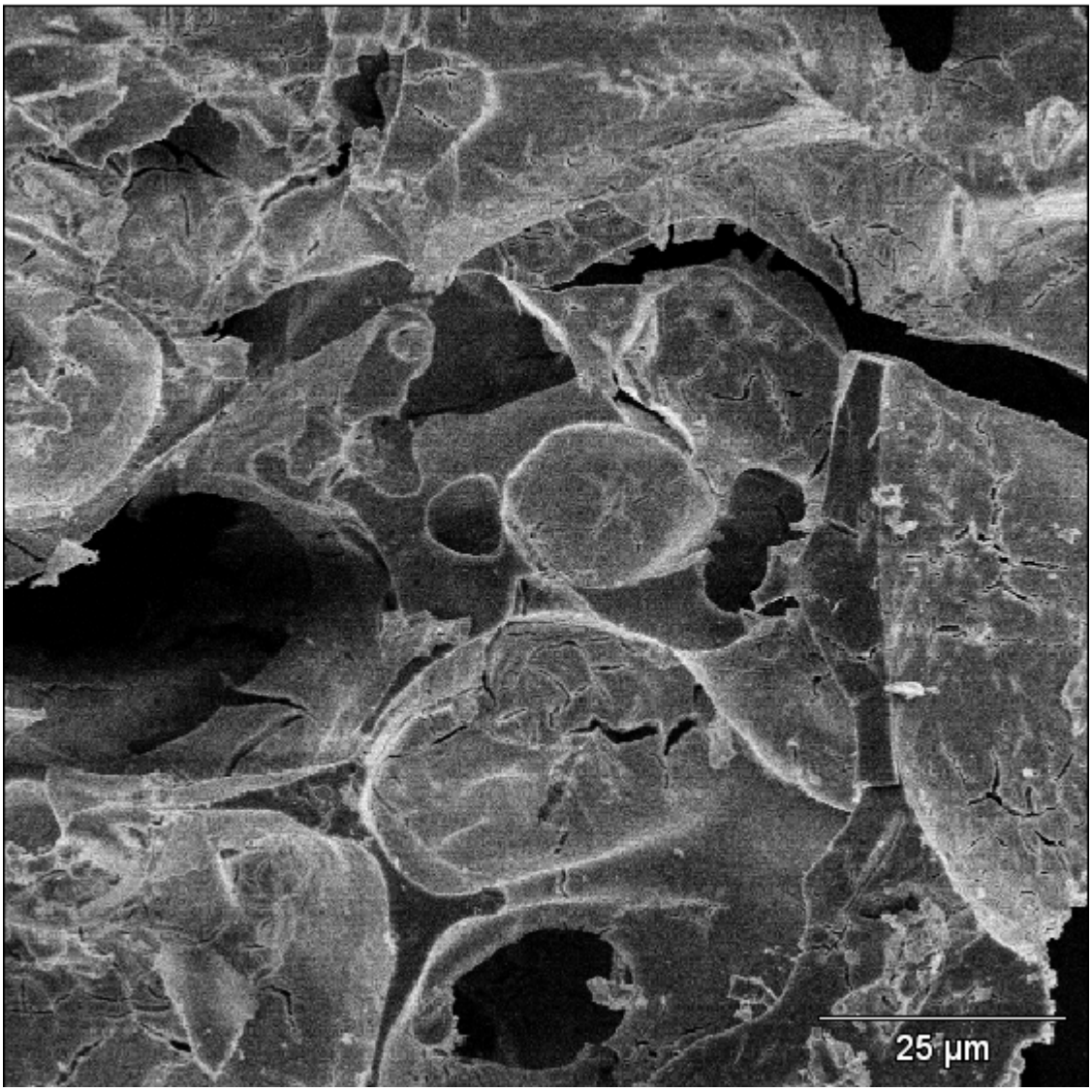

Accelerating Voltage: 10.0 kV Magnification: 1100

Close-up of catalyst pore on LZ surface.

Surface composition of LZ determined by EDS

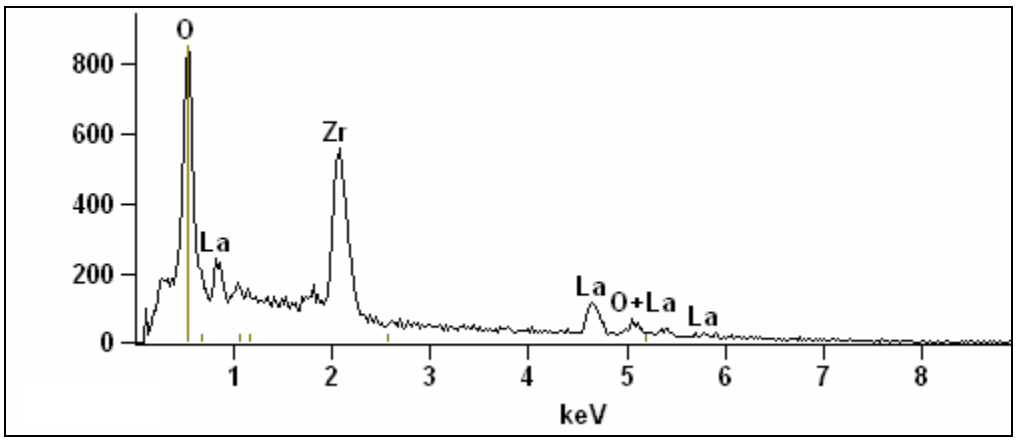

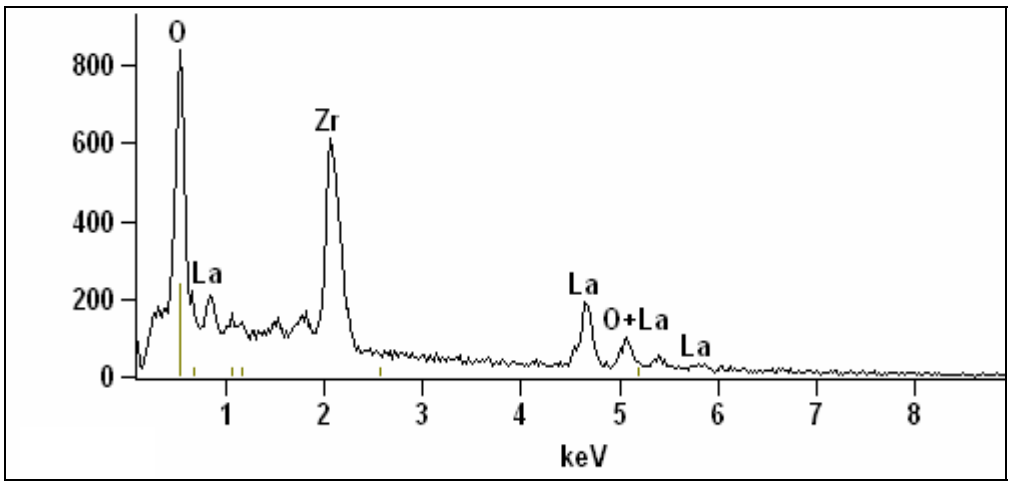

Rh/γ-Al_2O_3

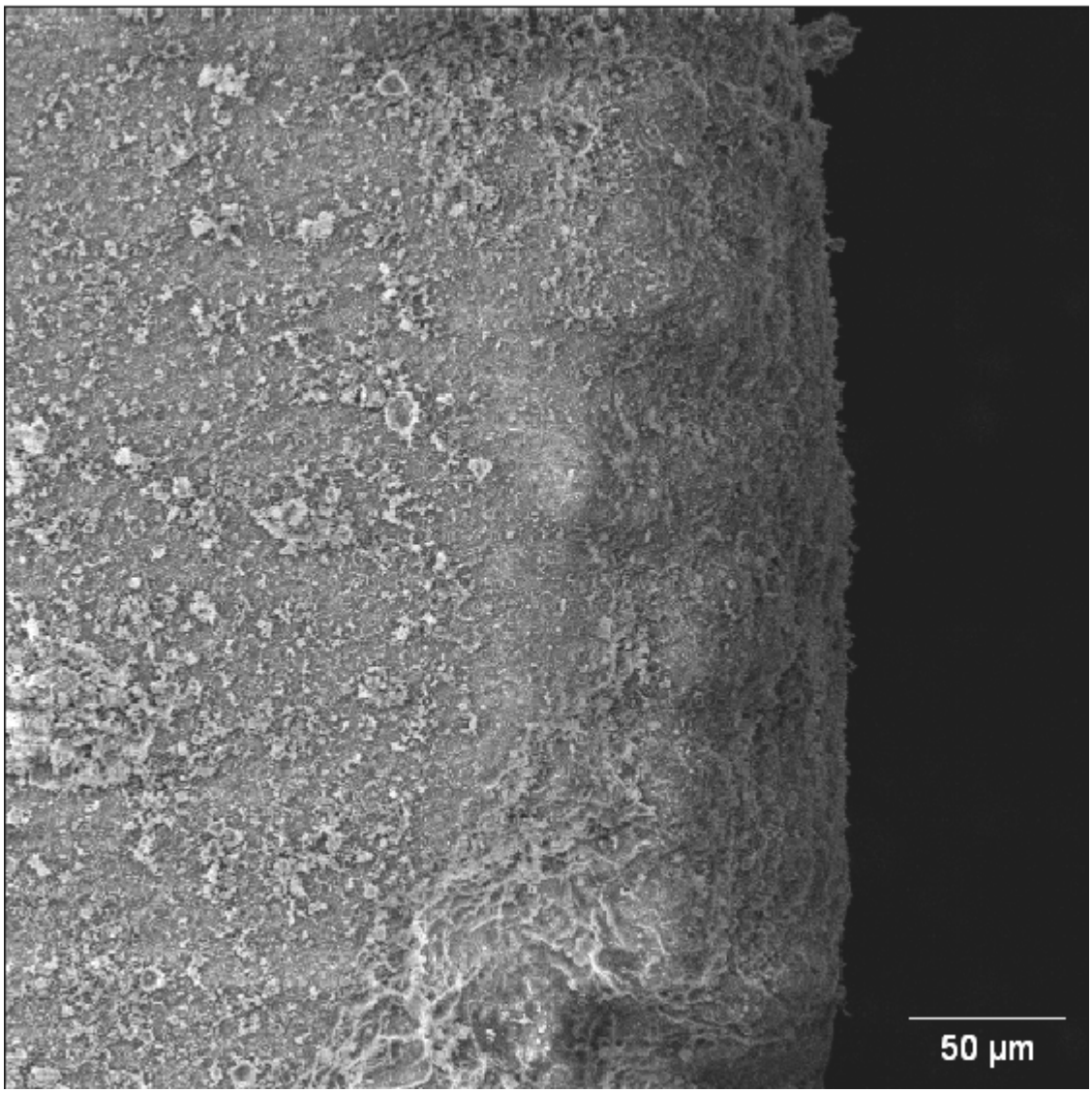

Accelerating Voltage: 10.0 kV Magnification: 350

Low magnification image of Rh/γ-Al_2O_3

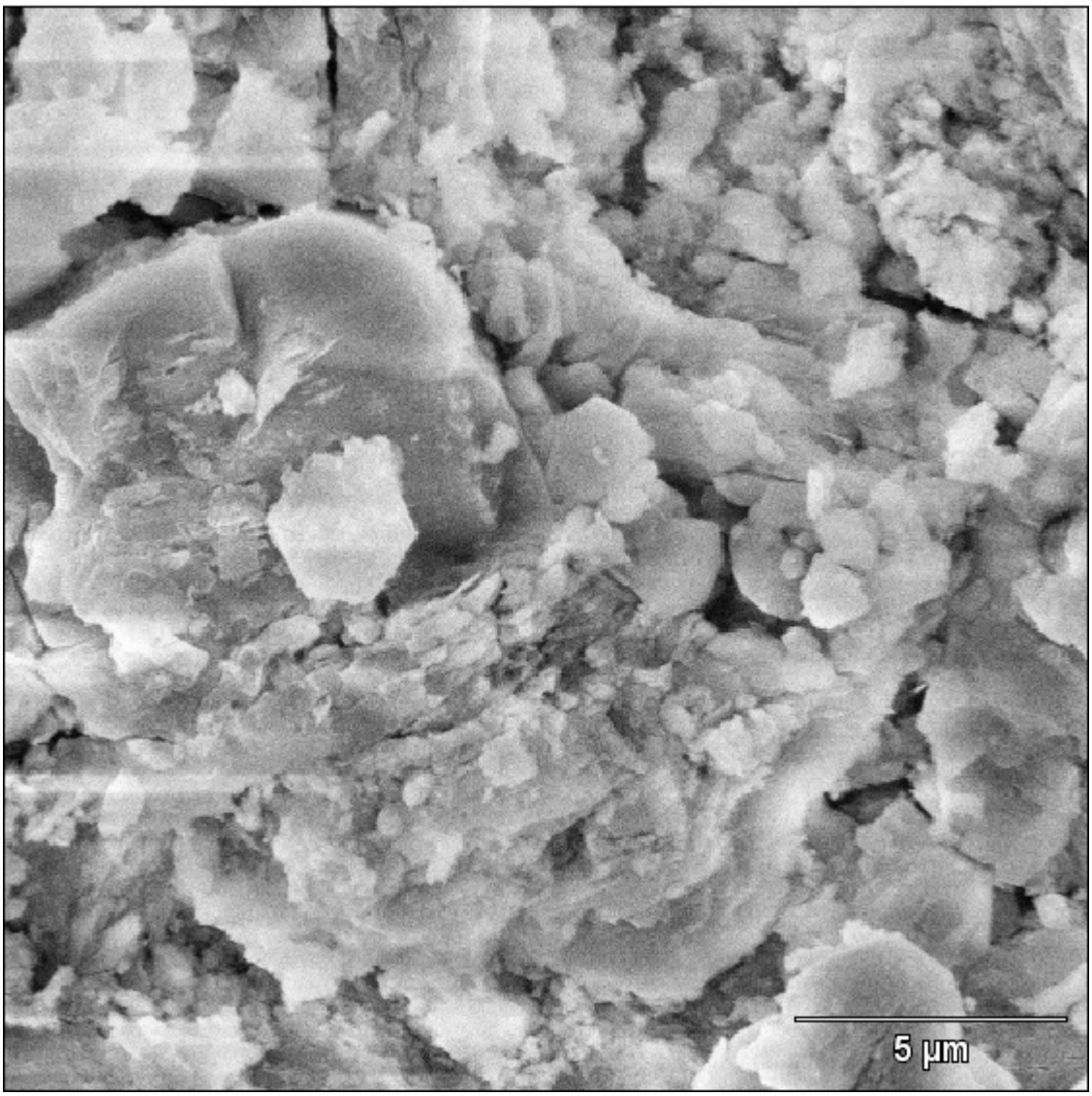

Accelerating Voltage: 10.0 kV Magnification: 6000

Close-up of Rh/γ-Al_2O_3 surface.

Surface composition of Rh/γ-Al_2O_3 determined by EDS

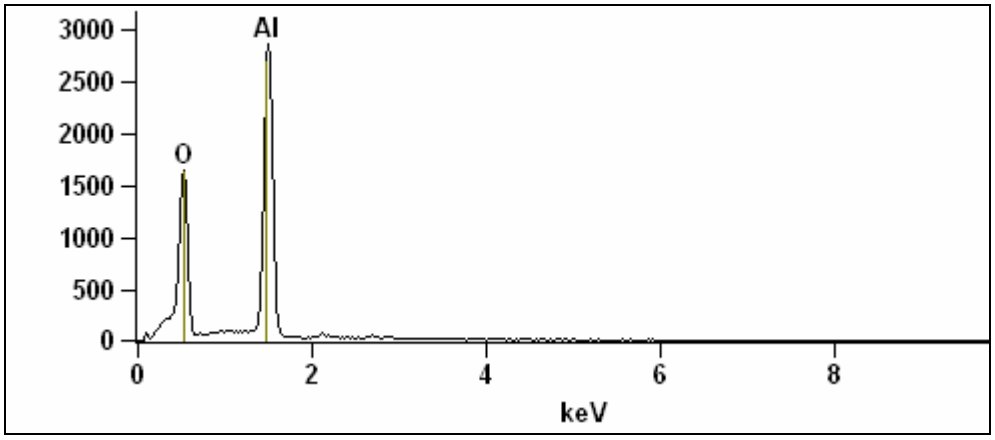

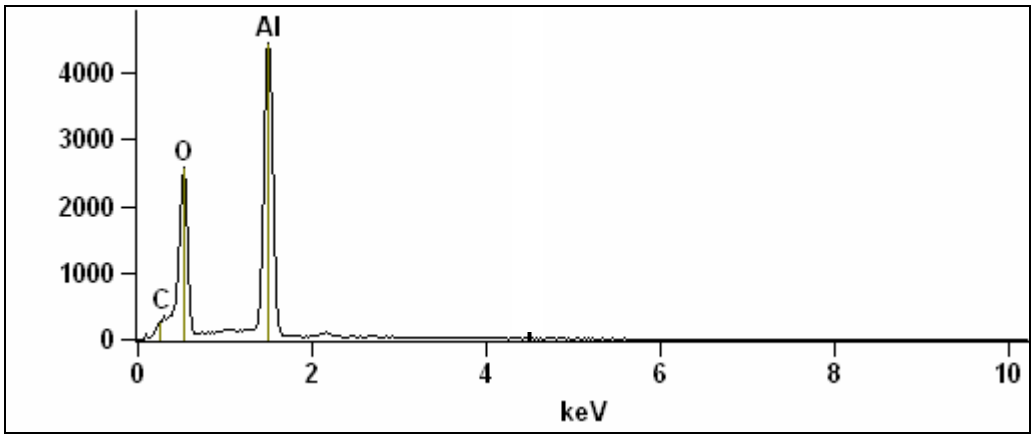

Appendix B. Internal Transport Calculation

$$\phi = R_p \sqrt{\frac{k}{D^e_{TA}}}\ ;\ \eta = \frac{robs}{rmx} = \frac{3}{\phi}\left[\frac{1}{\tanh(\phi)} - \frac{1}{\phi}\right]$$

R_p

Particle radius (R_p) used in experiment 60-100 mesh which corresponds to 0.0085-0.0155 cm range of R_p.

R_p chosen to be 0.0085 cm

D^e_{TA}

$\frac{1}{D^e_{TA}} = \frac{1}{D^e_{AB}} + \frac{1}{D^e_{KA}}$; $D^e_i = \frac{\bar{\varepsilon}}{\bar{\tau}} D_i$; where $\bar{\varepsilon}$ is porosity and $\bar{\tau}$ is tortuosity.

In the absence of experimental data $\bar{\varepsilon} = 0.5$ and $\bar{\tau} = 4$.

Molecular Diffusivity D^e_{AB}

$$D^e_{AB}(cm^2/\sec) = \frac{1.8582x10^{-3} T^{3/2}}{P\sigma^2_{AB}\Omega_{D,AB}}\left[\frac{1}{M_{Air}} + \frac{1}{M_{TD}}\right]^{1/2}$$

P= 2 atm, M_{Air}= 29 g/mol, M_{TD}= 198 g/mol

$$\sigma_{AB} = \frac{1}{2}(\sigma_{Air} + \sigma_{TD})$$

$\sigma_{Air} = 3.711$Å

$\sigma_{TD} = 0.841\,\tilde{V}_c^{1/3}$, $\tilde{V}_{c,TD} = 830$ cm^3/mol; $\sigma_{TD} = 7.90$Å

$$\sigma_{AB} = \frac{(3.711 + 7.90)}{2} = 5.85\text{Å}$$

$\Omega_{D,AB}$ = collision integral, pg 583 property gas and liquid

$$\Omega_{D,AB} = \frac{A}{(T^*)^B} + \frac{C}{\exp(DT^*)} + \frac{E}{\exp(FT^*)} + \frac{G}{\exp(HT^*)}$$

A= 1.06036, B= 0.15610, C=0.1930, D= 0.47635, E= 1.03587, F= 1.52996, G= 1.76474, H=3.89411

$T^* = \frac{KT}{\varepsilon_{AB}}$; T= 1173K (900°C), K= Boltzmann's constant= $1.3806*10^{-23}$ (J/K)

$$\varepsilon_{AB} = (\varepsilon_{Air}\varepsilon_{TD})^{1/2}$$

For binary gas systems at low pressure $\frac{\varepsilon}{K} = 1.15T_b$, T_b= boiling T(K)

T_{bAir}= 787.7K T_{bTD}= 526K

$$\varepsilon_{Air} = (78.7K)(1.15)(1.3806x10^{-23}\frac{J}{K}) = 1.25x10^{-21}J$$

$$\varepsilon_{TD} = (526K)(1.15)(1.3806x10^{-23}\frac{J}{K}) = 8.35x10^{-21}J$$

$$\varepsilon_{AB} = \left[(1.25x10^{-21}J)*(8.35x10^{-21}J)\right]^{1/2} = 3.23x10^{-21}J$$

$$T^* = \frac{(1.3806x10^{-23}\frac{J}{K})(1173K)}{(3.23x10^{-21}J)} = 5.01$$

$$\Omega_D = \frac{1.06036}{(5.01)^{0.15610}} + \frac{0.1930}{\exp(2.386)} + \frac{1.03587}{\exp(7.665)} + \frac{1.76464}{\exp(19.471)} = 0.84$$

$$D_{AB}^e(cm^2/\sec) = \frac{1.8582x10^{-3}(1173)^{3/2}}{2(5.85)^2(0.84)}\left[\frac{1}{28} + \frac{1}{198}\right]^{1/2} = 0.26cm^2/\sec$$

Knudsen Diffusivity

$$D_{KTD}(cm^2/\sec) = (9.7x10^3) \bullet R_{pore} \bullet \left(\frac{T}{M_{TD}}\right)^{1/2}$$

The pore radius for LRZ was used so calculation would result in the highest diffusion coefficient.

$$D_{KTD} = (9.7x10^3) \bullet (1.1x10^{-6}) \bullet \left(\frac{1173K}{198}\right)^{1/2} = 0.025cm^2/\sec$$

$\frac{1}{D^e_{TA}} = \frac{1}{D^e_{AB}} + \frac{1}{D^e_{KA}}$; Assume only Knudsen diffusivity because of small pore size.

Then $D^e_{TTD} = D^e_{KTD} = \frac{\bar{\varepsilon}}{\bar{\tau}} D_{KTD} = \frac{0.5}{4}(0.25cm^2/s)$ =0.0031cm^2/s

Reaction Rate Constant k

Assume rate expression $r_{HC} = k_0(L/mol)^{a+b+c-1} e^{-\frac{E_A}{RT}} C^a_{HC} C^b_{H_2O} C^c_{O_2}$ for ATR is valid for POX if b=0.

* No kinetic parameters are reported for Rh/γ-Al_2O_3, so those for Pd/γ-Al_2O_3 will be used because it has the highest pre-exponential factor and will result in the highest reaction rate.

Parameters for Pd/γ-Al_2O_3

k_0= 44.7 (L/mol)$^{-0.16}$; E_A= 69 (KJ/mol); a= 0.74, c= 0.10

$$C_{TD}^{STP}(mol/L) = 9.5x10^{-4}\ ; C_{TD}^{1173K,\,2\,atm}(mol/L) = (9.5x10^{-4})\left(\frac{1173K}{273K}\right)\left(\frac{1atm}{2atm}\right) = 2.04x10^{-3}(mol/L)$$

$$C_{O_2}^{STP}(mol/L) = 8.0x10^{-3}; C_{TD}^{1173K,\,2\,atm}(mol/L) = (8.0x10^{-3})\left(\frac{1173K}{273K}\right)\left(\frac{1atm}{2atm}\right) = 1.7x10^{-2}(mol/L)$$

Then,

$$r_{HC} = 44.7\left(\frac{L}{mol}\right)^{-0.16} e^{-\frac{69000\frac{J}{mol}}{(8.314\frac{J}{molK})(1173K)}}\left(2.04x10^{-3}\frac{mol}{L}\right)^{0.74}\left(1.7x10^{-2}\frac{mol}{L}\right)^{0.10}$$

$$r_{HC} = 2.6x10^{-4}\frac{mol}{L \bullet \sec}$$

Assume r_{HC} is equal to pseudo 1st order rate expression $r_{HC} = k'C_{TD}$

Solve for k': $k' = \left(\frac{2.6x10^{-4}\ mol}{L \bullet \sec}\right)\left(\frac{L}{2.04x10^{-3}\ mol}\right) = 0.13s^{-1}$

Thiele Modulus

$$\phi = R_p\sqrt{\frac{k'}{D_{TTD}^e}}$$

R_p= 0.0085cm; D_{TTD}^e 0.0031cm^2/s; $k' = 0.13s^{-1}$

$\phi = 0.00745cm\sqrt{\frac{0.13s^{-1}}{0.0031cm^2/s}}$ =0.047 <<<0.95 where transport limitations begin, so with the assumptions made there are no internal transport limitations.

Appendix C. Sample Calculations (for Rh/γ-Al_2O_3)

Compositions

	A	B	C	D	E
	A. Feed specifications				
	Flow rates and compositions				
			POX (basis)*	POX molar	POX sccm
	Species		**mol**	**Comp.**	**Flow Rate**
	O_2/Bal N_2		4.24	0.1786	18
	H_2O		0.00	0.0000	0
	C14		0.51	0.0213	2
	N_2		16.04	0.6751	68
	N2 (only)		2.97	0.1250	13
	N2 (Total)			0.8001	
	Total Σ		23.75		100
	Check		S/C	0.00	
			O2/C	0.60	
			H2O/C	**0**	
			O2/C	**0.6**	
	Pressure	10	psig		
	Bed Height	9.19	mm		
	Reactor ID	8	mm		

	A	B	C	D	E
1	**A. Feed specifications**				
2	**Flow rates and compositions**				
3			POX	POX	POX
4			(basis)*	molar	sccm
5	**Species**		**mol**	**Comp.**	**Flow Rate**
6	**O_2/Bal N_2**		=+D9*14*E17	=+D7/$D$13	=E7*$F$13
7	**H_2O**		=+D9*14*E16	=+D8/$D$13	=E8*$F$13
8	**C14**		=100/198	=+D9/$D$13	=E9*$F$13
9	**N_2**		=3.78*D7	=+D10/$D$13	=E10*$F$13
10	**N2 (only)**		2.97	=+D11/$D$13	=E11*$F$13
	N2 (Total)			=+E10+E11	
	Total Σ		=+SUM(D7:D11)		100
	Check		S/C	=F8/F9/14	
			O2/C	=+(F7)/(14*F9)	
			H2O/C	**0**	
			O2/C	**0.6**	

Pressure	10	psig
Bed Height	=0.375*24.5	mm
Reactor ID	8	mm

Flow Rates

	O	P	Q
3	Temp (°C)	Total Gas FR (sccm)	GHSV
4	900	400.6	52,073

	O	P	Q
3	Temp (°C)	Total Gas FR (sccm)	GHSV
4	900	400.6	=P4*1000*60/(3.14*$C$20*$C$20*$C$19/4)

	R	S	T	U	V	W	X	Y
	sccm	sccm	sccm	sccm	mol/min	mol/min	mol/min	ml/min
3	O2 FR	N2 FR	Air FR	C14	O2 FR	N2 FR	C14	C14
4	72	321	342	9	0.0032	0.0143	0.0004	0.099

	R	S	T	U	V	W
	sccm	sccm	sccm	sccm	mol/min	mol/min
3	O2 FR	N2 FR	Air FR	C14	O2 FR	N2 FR
4	=+E$7*P4	=+E$12*P4	=+S4*4.78	=+$E$9*P4	=+S4/82.05/273	=+T4/82.05/273

	X	Y
	mol/min	ml/min
3	C14	C14
4	=+V4/82.05/273	=+Z4*198/0.763

Molar Flow Rate

	B	G
		(moles/min)
26	H2	0.00154
27	CO	0.00213
28	CO2	0.00163
29	O2	0.00000
30	N2	0.01431
31	Methane	0.00037
32	Ethane	0.00002
33	Ethylene	0.00037

34	Propane	0.00000
35	Propylene	0.00005
36	1-Butene	0.00000
37	1,3 Butadiene	0.00002
38	1-Pentene	0.00000
39	1-Hexene	0.00001
40	Benzene	0.00003
41	Total Flow (moles/min)	0.020481

	B	H (moles/min)
26	H2	=+H$41*Raw!H22/100
27	CO	=+H$41*Raw!H23/100
28	CO2	=+H$41*Raw!H24/100
29	O2	=+H$41*Raw!H25/100
30	N2	=+H$41*Raw!H26/100
31	Methane	=+H$41*Raw!H27/100
32	Ethane	=+H$41*Raw!H28/100
33	Ethylene	=+H$41*Raw!H29/100
34	Propane	=+H$41*Raw!H30/100
35	Propylene	=+H$41*Raw!H31/100
36	1-Butene	=+H$41*Raw!H32/100
37	1,3 Butadiene	=+H$41*Raw!H33/100
38	1-Pentene	=+H$41*Raw!H34/100
39	1-Hexene	=+H$41*Raw!H35/100
40	Benzene	=+H$41*Raw!H36/100
41	Total Flow (moles/min)	=+$Y$4*100/Raw!H26

Raw MS and GC data that is associated with this data point

	B	H
RAW22	H2	11.852
RAW23	CO	13.299
RAW24	CO2	6.545
RAW25	O2	0.000
RAW26	N2	65.514
RAW27	Methane	1.378
RAW28	Ethane	0.084
RAW29	Ethylene	1.060
RAW30	Propane	0.003
RAW31	Propylene	0.114
RAW32	1-Butene	0.000
RAW33	1,3-Butadiene	0.030
RAW34	1-Pentene	0.000

RAW35	1-Hexene	0.051
RAW36	Benzene	0.070

Yield and Mass Balances Calculation

	B	H
47	H2	26.95
48	CO	40.04
48	CO2	30.66
50	Methane	6.88
51	Ethane	0.78
52	Ethylene	13.77
53	Propane	0.06
54	Propylene	2.92
55	1-Butene	0.00
56	1,3 Butadiene	1.48
57	1-Pentene	0.09
58	1-Hexene	1.04
59	Benzene	3.86
60	O2	100.00
61	C Bal	101.57
62	O Bal	0.0004964
63	H Bal	0.0022548
64	H Bal/O Bal	4.54221

	B	H
47	H2	=+H26*100/$Z$4/15
48	CO	=+H27*100/$Z$4/14
48	CO2	=+H28*100/$Z$4/14
50	Methane	=+H31*100/$Z$4/14
51	Ethane	=+H32*2*100/$Z$4/14
52	Ethylene	=+H33*2*100/$Z$4/14
53	Propane	=+H34*3*100/$Z$4/14
54	Propylene	=+H35*3*100/$Z$4/14
55	1-Butene	=+H36*4*100/$Z$4/14
56	1,3 Butadiene	=+H37*4*100/$Z$4/14
57	1-Pentene	=+H38*5*100/$Z$4/14
58	1-Hexene	=+H39*6*100/$Z$4/14
59	Benzene	=+H40*6*100/$Z$4/14
60	O2	=+($X4-H29)*100/$X4
61	C Bal	=SUM(H48:H59)
62	O Bal	=+($X4-H28-H27/2)
63	H Bal	=+(15*$Z4-H26-H31*2-H32*3-H33*2-H34*6-H35*3-H36*4-H37*3-H38*5-H39*6-H40*3)
64	H Bal/O Bal	=H63/H62

Error Analysis

Mass Flow Controller Error

	O	P	Q	R	S
11		Total Flow Mol/min	Error	MFC Range (sccm)	MFC Error
12	Air MFC (N2)	0.012098403	0.000892871	2000	0.01
13	N2 MFC	0.002232178	0.000892871	2000	0.01
14	total N2 in	0.014330581			
15	N2 in (MFC) Error		0.00126271		
16	Total O2	0.0032			
17	O2 in (MFC) Error		0.000892871		

	O	P	Q	R	S
11		Total Flow Mol/min	Error	MFC Range (sccm)	MFC Error
12	Air MFC (N2)	=271/82.05/273	=(R12*S12)/82.05/273	2000	0.01
13	N2 MFC	=50/82.05/273	=(R13*S13)/82.05/273	2000	0.01
14	total N2 in	=SUM(P12:P13)			
15	N2 in (MFC) Error		=((Q12)^2+Q13^2)^0.5		
16	Total O2	=$X$4			
17	O2 in (MFC) Error		=Q12		

Mass Spec, GC and Pump Error

	T	U	V	W
11	Mass Spec Error	Flow rate TD mol/min	Pump Error	Pump Error
12	0.02	0.0004	0.01	3.80251E-06
13				
14		H2 (in)		
15		0.00570377		5.70377E-05

	T	U	V	W
11	Mass Spec Error	Flow rate TD mol/min	Pump Error	Pump Error
12	0.02	=$Z$4	0.01	=0.01*U12
13				
14		H2 (in)		
15		=U12*15		=U15*0.01

Measurement Error

	B	H	T
		(molesmin)	Measurement Error
26	H2 error	0.00486	0.0001422
27	CO	0.00437	0.0001972
28	CO2	0.00105	0.0001510
29	O2	0.00000	0.0000000
30	N2	0.01431	0.0013243
30	Methane	0.00005	0.0000339
32	Ethane	0.00000	0.0000019
33	Ethylene	0.00000	0.0000339
34	Propane	0.00000	0.0000001
35	Propylene	0.00000	0.0000048
36	1-Butene	0.00000	0.0000000
37	1,3 Butadiene	0.00000	0.0000018
38	1-Pentene	0.00000	0.0000001
39	1-Hexene	0.00000	0.0000008
40	Benzene	0.00000	0.0000032
41	Total Flow	0.024642	0.001851

	B	H	T
		(moles/min)	Measurement Error
26	H2 error	=+H$41*Raw!H22/100	=((((0.02)))^2+(T$41/H$41)^2)^0.5*H26
27	CO	=+H$41*Raw!H23/100	=((((0.02)))^2+(T$41/H$41)^2)^0.5*H27
28	CO2	=+H$41*Raw!H24/100	=((((0.02)))^2+(T$41/H$41)^2)^0.5*H28
29	O2	=+H$41*Raw!H25/100	=((((0.02)))^2+(T$41/H$41)^2)^0.5*H29
30	N2	=+H$41*Raw!H26/100	=((((0.02)))^2+(T$41/H$41)^2)^0.5*H30
31	Methane	=+H$41*Raw!H27/100	=((((0.02)))^2+(T$41/H$41)^2)^0.5*H31
32	Ethane	=+H$41*Raw!H28/100	=((((0.02)))^2+(T$41/H$41)^2)^0.5*H32
33	Ethylene	=+H$41*Raw!H29/100	=((((0.02)))^2+(T$41/H$41)^2)^0.5*H33
34	Propane	=+H$41*Raw!H30/100	=((((0.02)))^2+(T$41/H$41)^2)^0.5*H34
35	Propylene	=+H$41*Raw!H31/100	=((((0.02)))^2+(T$41/H$41)^2)^0.5*H35
36	1-Butene	=+H$41*Raw!H32/100	=((((0.02)))^2+(T$41/H$41)^2)^0.5*H36
37	1,3 Butadiene	=+H$41*Raw!H33/100	=((((0.02)))^2+(T$41/H$41)^2)^0.5*H37
38	1-Pentene	=+H$41*Raw!H34/100	=((((0.02)))^2+(T$41/H$41)^2)^0.5*H38
49	1-Hexene	=+H$41*Raw!H35/100	=((((0.02)))^2+(T$41/H$41)^2)^0.5*H39
40	Benzene	=+H$41*Raw!H36/100	=((((0.02)))^2+(T$41/H$41)^2)^0.5*H40
41	Total Flow	=+$Y$4*100/Raw!H26	=((0.02)^2+($Q$15/$P$14)^2)^0.5)*H$41

	B	H	T
			Measurement Error
62	O Bal (mol/min)	0.0004964	0.00091257
63	H Bal (mol/min)	0.0022548	0.0002563
64	H/O	4.54221	1.837

	B	H	T
			Measurement Error
62	O Bal (mol/min)	=+($X4-H28-H27/2)	=($Q$17^2+T28^2+(T27/2)^2)^0.5
63	H Bal (mol/min)	=+(15*$Z4-H26-H31*2-H32*3-H33*2-H34*6-H35*3-H36*4-H37*3-H38*5-H39*6-H40*3)	=($W$15^2+T26^2+(T31*2)^2+(T32*3)^2+(T33*2)^2+(T34*4)^2+(T35*3)^2+(T37*3)^2+(T38*5)^2+(T39*6)^2+(T40*3)^2)^0.5
64	H/O	=H63/H62	=((T63/H63)^2+(T62/H62)^2)^0.5

Appendix D. Instrument Calibrations

Mass Flow Controllers

Calibration Date: October 18, 2005
Operator: S. Clingenpeel
Calibration Gas: N2
Process Gas: AIR
Test Data File: C:\Program Files\COMPASS for molbox\data\FTC-425\2005_291_000.dat
Project: B-25, Room 201 FPL

Device Under Test		Reference	
Manufacturer	BROOKS INSTRUMENT	Manufacturer	DH Instruments Inc.
Model	5850I	Model	Molbox1-AG
Tag/SN	FTC-425/SN: 0103100245067001	SN	398/884
ID	1204794/Inlet Press: 100 psig	ID	0000000119/1202431
Flow Range	0.000 to 2000.000 sccm @ 0.00C	Range	0-5000 sccm
Output Range	0.000 to 5.000 V		
Tolerance	1 %DUTFS		
Inlet Pressure	100 psig (+/- 5 psig)		

Calibration Data (As Found)

Ref Flow (sccm @ 0.00C)	DUT Flow (sccm @ 0.00C)	DUT Output (V)	%Rdg Error	%FS Error	Temp	Press (psi)
0.0000	0.4000	0.0010	N/A	0.020	23.541	14.160
204.16	200.1	0.5000	-2.000	-0.204	23.563	14.790
404.29	400.0	1.000	-1.062	-0.215	23.588	15.390
601.90	600.0	1.500	-0.316	-0.095	23.610	15.970
797.50	800.0	2.000	0.314	0.125	23.626	16.520
992.73	1000.	2.500	0.732	0.363	23.638	17.050
1187.6	1200.	3.000	1.041	0.618	23.660	17.570
1383.3	1400.	3.500	1.211	0.837	23.677	18.070
1578.9	1600.	4.001	1.359	1.073	23.699	18.570
1777.9	1800.	4.499	1.223	1.087	23.719	19.060
1947.8	1967.	4.917	0.974	0.949	23.740	19.470

Mass Spectrometer

Cal Gas Name	Gas	% in mix	Old calibration factor	New calibration factor	% Change	Standard Check	% error
FPL FUEL MIX	CO2	15.2	1.20339	1.19897	0.37	15.1793	-0.14
FPL FUEL MIX	CH4	9.9	0.66037	0.66983	-1.41	9.8982	-0.02
FPL FUEL MIX	H2	9.85	0.51053	0.50840	0.42	9.9060	0.57
FPL FUEL MIX	N2	65.05	0.98360	0.98390	-0.03	64.9506	-0.15
FPL Air	N2	78.08	0.96400	0.97430	-1.06	78.0580	-0.03
FPL Air	O2	20.947	0.85895	0.84872	1.21	20.9215	-0.12
FPL Air	Ar	0.934	1.55022	1.53797	0.80	0.9390	0.53
FPL CO	CO	9.66	1.07966	1.08828	-0.79	9.639069	-0.22
FPL CO	He	90.34	0.14443	0.14270	1.21	90.27664	-0.07

Gas Chromatograph

5/22/2006

Gas	Retention Time	% Difference from Previous Calibration	Concentration PPM	Average Peak Area	Average Calibration Factor	% Difference from Previous Calibration
Methane	4.341	1.095	9991.40	192,844	19.301	2.53
Ethane	4.755	0.913	1003.20	32,530	32.426	2.70
Ethylene	5.130	0.707	9981.00	302,844	30.342	2.37
Propane	5.869	0.479	50.10	2,748	54.848	2.51
Propylene	6.663	0.226	7981.00	408,946	51.240	1.89
1-Butene	8.010	0.062	1995.70	138,374	69.336	2.45
1,3-Butadiene	8.783	0.068	1998.30	138,598	69.358	2.22
1-Pentene	9.609	0.052	200.50	17,954	89.548	2.26
1-Hexene	12.372	0.105	198.40	20,837	105.026	1.89
Benzene	16.578	0.163	2494.60	271,320	108.763	1.57

Previous Calibration

5/19/2006

Gas	Retention Time	% Difference from Previous Calibration	Concentration PPM	Average Peak Area	Average Calibration Factor	% Difference from Previous Calibration
Methane	4.294	0.210	9991.40	188,078	18.824	3.35
Ethane	4.712	0.255	1003.20	31,673	31.572	3.81
Ethylene	5.094	0.374	9981.00	295,837	29.640	3.17
Propane	5.841	0.430	50.10	2,681	53.505	5.29
Propylene	6.648	0.544	7981.00	401,357	50.289	2.91
1-Butene	8.005	0.540	1995.70	135,061	67.676	2.71
1,3-Butadiene	8.777	0.550	1998.30	135,589	67.852	2.89
1-Pentene	9.604	0.587	200.50	17,558	87.572	2.93
1-Hexene	12.359	0.799	198.40	20,451	103.078	3.61
Benzene	16.551	1.056	2494.60	267,137	107.086	3.40

Vita

Daniel Haynes received his bachelor's degree in chemical engineering from The University of Toledo in May 2004. While completing his undergraduate degree he had several co-operative experiences within his field of study. The first was a quality control intern at Perstorp Polyols, a paint and concrete intermediates producer, in Toledo. There he performed various analytical tests to verify the products met quality specifications of the company and the buyer. In January 2002 he obtained an internship with Battelle/PNNL in Richland, Washington. As an intern with PNNL he worked closely with researchers on the catalytic fuel processing of methanol into a hydrogen gas for fuel cells. His responsibilities included setting up and designing experimental test stands to screen the catalysts as well as performing catalyst activity tests. This internship ended in August 2002, but was only one of 3 that he was able to work there. PNNL invited him back during the summers of 2003 and 2004 to continue work in fuel processing. In fall 2004 he started his classes at LSU. He took classes for a year, and then moved to Morgantown, West Virginia to perform the research that is discussed in this work.